Multi-Modal Imaging of Myocardial Ischemia and Reperfusion in a Rat Model

O H-Ici, Darach Michael

Awarding institution:
King's College London

MULTI-MODAL IMAGING OF MYOCARDIAL ISCHEMIA AND REPERFUSION IN A RAT MODEL

Darach O h-Ici

A dissertation submitted for the degree of
Doctor of Philosophy
of the
University of London

Division of Imaging Sciences and Biomedical Engineering
King's College London, School of Medicine

Abstract

Myocardial ischaemia causes progressive cellular injury. Initially there is loss of function, followed by formation of oedema. Ischemia, if prolonged, will eventually lead to cell death. Revascularisation of occluded coronary arteries is an efficient tool to reduce infarct size in acute myocardial infarction. However, reperfusion in itself can be associated with a significant amount of myocardial damage. The structural and metabolic changes occurring in myocardial ischemia and reperfusion can now be studied in-vivo using magnetic resonance imaging (MRI) and are targets to optimise the treatment of patients with acute myocardial ischemia.

The development of new MRI techniques for T_1 mapping allows the study of the evolution of myocardial oedema in both humans and animals. Moreover, hyperpolarised MR spectroscopy (MRS) allows the non-invasive assessment of myocardial metabolism, as injected hyperpolarised molecules can be used to study the function of metabolic pathways and enzymes in the setting of ischaemia and reperfusion.

The aims of this project were to develop an animal model to allow the study of myocardial ischemia in real time, and then use this model to study the acute development of oedema and the metabolic changes in the metabolism of pyruvate.

With the use of a vascular occluder, we successfully developed a closed-chest model of ischemia in the rat. This model allowed the animals to recover from the stress of surgery while also allowing ischemia experiments to be carried while the animals remain in the bore of the scanner. We then proceeded to validate this model and validate a new MR sequence, which produces cine-MR, T_1 mapping and inversion-recovery prepared images. We studied the effects of varying durations of myocardial ischemia on the development of myocardial infarction and used this to validate the Small Animal Look-Locker Inversion Recovery (SALLI) multimodal imaging sequence. We were also able to study the development of myocardial oedema in real time, and demonstrate that preconditioning attenuated the T_1 lengthening effects of myocardial

ischemia. Following this, the acute changes in pyruvate metabolism occurring in the myocardial area at risk following 15 minutes of myocardial ischemia were investigated. We were able to detect abnormal metabolism in the area at risk for the first 60 minutes following ischemia and demonstrated that metabolism returned to normal 1 week after ischemia. The methods used show much promise in the study of the changes occurring in myocardial ischemia-reperfusion, and study of the effects of treatments such as pre- and postconditioning.

Table of Contents

Table of Figures

Table of Tables

Acknowledgements

I would like to thank my family for their unquestioning support, encouragement and guidance.

I would like to thank my supervisors for their wisdom, guidance and near unending patience.

In particular, I would like to thank my colleagues Ulrich Kemnitz, Sarah Jeuthe at the German Heart Centre for their advice and assistance with all the animal experiments. Other colleagues that helped during the experiments included Dr. Thore Dietrich and the other members of his lab group, Heike Meyborg and Katharine Wittstock. A particular thanks must go to my colleagues Patrick Wespi, Julia Busch, Lukas Wissmann, Marcin Krajewski, Kilian Weiss K, and Andres Sigfridsson at ETH Zürich for their assistance with the hyperpolarization experiments. Also at the ETH, Martin Bührer developed the SALLI patch, which allowed the experiments to be carried out; he also provided updates at regular intervals when required.

Abbreviations

Abbreviation	Meaning
AAR	Area at Risk
AD	Acquisition Duration
ATP	Adenosine Tri-Phosphate
AUC	Area-Under-the-Curve
CMR	Cardiac Magnetic Resonance
DNP	Dynamic Nuclear Polarisation
ECG	Electrocardiogram
ECV	Extracellular Volume
EF	Ejection Fraction
EMB	Endomyocardial Biopsy
EPI	Echo-Planar Imaging
EPSI	Echo Planar Spectroscopic Imaging
ESR	Electron Spin Resonance
FELASA	Federation of European Laboratory Animal Science Associations
FID	Free Induction Decay
FLASH	Fast Low Angle Shot Magnetic Resonance Imaging
GRE	Gradient Echo
I/R	Ischemia-Reperfusion
IDEAL	Iterative Decomposition of Water and Fat with Echo Asymmetry and Least-Squares Estimation
IR	Inversion Recovery
LCA	Left Coronary Artery
LGE	Late Gadolinium Enhancement
LV	Left Ventricle
M	Molar
MI	Myocardial Infarction
MOLLI	Modified Look-Locker Inversion-Recovery
MPTP	Mitochondrial Permeability Transition Pore
MRI	Magnetic Resonance Imaging
MRSI	Magnetic Resonance Spectroscopic Imaging
ms	Millisecond
NMR	Nuclear Magnetic Resonance
PCI	Percutaneous Coronary Intervention
PDH	Pyruvate Dehydrogenase
PRESS	Point-Resolved Spectroscopy
RD	Relaxation Duration
RF	Radiofrequency
ROI	Region of Interest
RV	Right Ventricle
SALLI	Small Animal Look-Locker Inversion recovery
SNR	Signal-to-Noise Ratio
SPECT	Single-Photon Emission Computed Tomography
SPSP	Spatial-Spectral
STEAM	Stimulated Echo Acquisition Mode
STEMI	ST-Elevation Myocardial Infarction
STIR	Short-Inversion-Time Inversion-Recovery
TE	Echo Time
TI	Inversion Time
TR	Repetition Time

TTC	Tetrazolium Chloride
VOI	Volume of Interest

Chapter 1 – Thesis Introduction

1.1 Introduction

Despite the striking advances in medical treatment, cardiovascular diseases remain a leading cause of morbidity and mortality. Further understanding of the processes of myocardial ischemia is essential to improve the treatment and prognosis of patients undergoing myocardial infarction. Patients who present with chest pain represent a group with a broad range of possible diagnoses. Cardiac magnetic resonance imaging (CMR) already plays an significant role in many centres, diagnosing acute myocardial infarction and giving important prognostic information about myocardial viability.

Further improvements are required in the area of the study of the myocardial area at risk (AAR); that is the myocardial tissue within the perfusion bed distal to the culprit lesion of the infarct-related coronary artery. For example, while CMR can detect acute myocardial injury in ischemia and myocarditis there is controversy about the role of CMR in the assessment of the size of the AAR (1, 2). As CMR does not involve radiation, it is an ideal method to study the pathological changes occurring following myocardial ischemia. Recent studies have demonstrated how dynamic the changes can be in response to myocardial injury, for example, myocardial water content appears to have a bimodal pattern following myocardial ischaemia/reperfusion (3). The recent development of methods to characterise the myocardium in-vivo now presents the possibility of whole-heart “non-invasive myocardial biopsy” (4).

CMR may be able to provide more information than the static information provided by biopsies, as developments in spectroscopy now offer the possibility of studying myocardial metabolism at baseline and in response to stresses such as myocardial ischemia. Until now, oedema imaging using CMR has played an important role in the diagnosis of acute injury and the detection of the AAR. Nuclear imaging techniques used changes in metabolism to identify the AAR (5). We aim to use hyperpolarised spectroscopic techniques to study in-vivo the rapid metabolic changes in the AAR. These changes have the potential to delineate the AAR, and to further our understanding of the processes of myocardial injury, cell death and myocardial reperfusion and reperfusion injury. For example, as of yet there is no method available to assess the magnitude of reperfusion injury in-vivo in patients.

Myocardial ischaemia occurs when the blood supply is unable to match the metabolic needs of the myocardium. As oxygen supply is limited, the cell shifts from aerobic metabolism to anaerobic metabolism to provide the cell with energy to maintain the functions of contraction, relaxation and homeostasis. When ischaemia is prolonged, contractile function ceases. Cellular homeostasis becomes deranged, with the failure of the cell membrane pumps that maintain intracellular fluid balance, before finally, the development of cellular rupture. This switch from aerobic to anaerobic metabolism could be used as a tool to detect the effects of myocardial ischaemia, and to study in-vivo the pathological processes involved in cell death in myocardial ischaemia.

The goal of treatments for myocardial ischaemia caused by coronary occlusion is the rapid reperfusion of the myocardium by reopening the coronary artery, either by using lytic drugs to dissolve the occluding thrombus or by percutaneous coronary intervention. Although this treatment results in salvage of the myocardium in the AAR, reperfusion itself may be associated with further injury (6). Currently, myocardial revascularization occurs rapidly after patients present to medical services, and further decreases in median time to revascularization (from 83 to 67 minutes) do not appear to be associated with reduced mortality (7). Alternative strategies to minimise myocardial injury are required, with reperfusion injury a prominent target. Strategies to increase myocardial salvage, the amount of myocardium in the AAR that remains viable, include pre- and postconditioning. The process of preconditioning was first described in a seminal paper nearly 30 years ago (8), which described how brief episodes of ischemia preceding prolonged coronary occlusion led to a reduction in the final size of myocardial infarction. This study was followed by others suggesting that both brief episodes of ischemia following reperfusion – postconditioning, and brief episodes of ischemia in a distal organ – remote conditioning, could lead to a reduction in infarction size. The mechanisms of this process are not completely understood but are thought to lead ultimately to a delay in the opening of the mitochondrial permeability transition pore (MPTP). This pore plays a crucial role in necrosis and apoptosis. The opening of this pore results in mitochondrial swelling and the uncoupling of oxidative phosphorylation (9). The mitochondria begin to break down ATP, starving the cell of energy, with disruption of cellular homeostasis. Therapies focused on preventing or delaying MPTP opening have received much attention but have yet to demonstrate a clinical benefit (10).

CMR has developed into the gold standard method of measurement of myocardial systolic function and in-vivo measurement of myocardial infarction using late gadolinium enhancement (LGE) (11). LGE can characterise myocardium in vivo, and is superior in the detection of both subendocardial infarction and defining the extent of transmural myocardial infarction to previously available nuclear imaging methods (12, 13). This technique has allowed clinicians to divide myocardium into viable and infarcted myocardium. However, in reality, the border zones of myocardial infarction may contain a mixture of both viable and infarcted myocardium, a so-called "grey zone" (14). LGE imaging is excellent in detecting infarction (white) and normal (black) myocardium, but assessment of this "grey zone" is challenging, as LGE does not provide a quantitative measurement of the degree of enhancement.

In patients with ischemic cardiomyopathy, myocardium remote from the infarction remodels, becoming hypokinetic and dilated, and develops increasing levels of myocardial fibrosis (15). Increased myocardial fibrosis is also seen in patients with dilated cardiomyopathy (16). In both of these conditions, LGE is unable to quantify this increased fibrosis as this technique requires the presence of a contrast difference between normal and pathological myocardium. These demands led to the development of advanced techniques to characterise the myocardium, including T_1 and T_2 mapping.

CMR uses differences in the relaxation properties of protons, predominantly found in water and fat in the body to generate image contrast. These relaxation properties, T_1 and T_2, can be quantified, but until recently, the motion of the heart presented difficulties in these measurements. Cardiac pulse sequences developments now allow the generation of myocardial maps, where each voxel has a value for the relaxation property of interest. As the relaxation properties are based largely on the water content and binding of water in a tissue, each tissue will have a normal range of T_1 and T_2 values. Changes in native myocardial T_1 and T_2 have been used to detect the AAR (17), probe acute and chronic myocardial infarction (18, 19) and myocarditis (15). This native T_1 value reflects composite water signal from interstitium and myocytes, and therefore reflects myocardial water content. Gadolinium contrast agents are also used to characterise the myocardium. As gadolinium remains extracellular, changes in T_1 following injection of contrast reflect changes in the extracellular space. This value, known as post-contrast T_1, can be compared with the native T_1 value. The development of these imaging

techniques now allows insight into the formation of myocardial oedema and changes in the intracellular and extracellular space, all significant processes in the pathology of myocardial ischemia and infarction.

It is now clear that CMR can assess myocardial function and characterise the myocardium. It has also been possible for many years to use MRI to study myocardial metabolism. However, the spectroscopic techniques used were limited by a low signal to noise ratio, low temporal and spatial resolution and low reproducibility. Recent developments, known as hyperpolarised spectroscopy, have the potential to increase signal to noise ratios by 10,000-100,000, allowing unprecedented study of the myocardial metabolism (20). This technique uses a carbon-containing molecule of low molecular weight, such as pyruvate, to probe metabolic pathways. Simply, the substrate of interest is frozen and hyperpolarised, a process where the near complete polarisation of electrons at low temperatures and high magnetic field strengths is transferred to the molecule of interest. This molecule is then rapidly dissolved and injected into the subject of interest. As pyruvate sits at a central point between glycolysis and the Krebs cycle, hyperpolarised spectroscopy can provide information about the metabolism of carbohydrates in the cell. A particular challenge of this technique is the rapid decay of the hyperpolarised signal. However, this can be seen as an advantage, as it allows sequential studies to be carried out without interference from preceding injections.

1.1 Aim

The aim of this thesis was to study the structural and metabolic changes occurring in acute myocardial ischemia using both T_1 mapping techniques and hyperpolarised ^{13}C spectroscopic imaging. Firstly, a suitable animal model needed to be established, followed by the development and adaptation of methods of T_1 mapping and hyperpolarised imaging to allow the study of the changes occurring in myocardial ischemia in vivo.

1.2 Outline of thesis

Chapter 2 outlines some of the basics of nuclear magnetic resonance and MRI, including an overview of some of the imaging techniques and the technique of ^{13}C dynamic nuclear polarisation (DNP).

Chapter 3 then describes the history and development of T_1 mapping, followed by its cardiac application, including in acute and chronic myocardial infarction, and the native and post-contrast uses (published as Review paper: O h-Ici et al., T_1 mapping in ischaemic heart disease. Eur Heart J Cardiovasc Imaging. 2014 Jun;15(6):597-602).

To study the changes in acute myocardial ischemia, we first needed to develop a suitable model. Although the open chest myocardial infarction model in the rat is well developed, this model was not suitable for our purposes. Any repositioning of the animal to occlude the coronary artery would interfere with the study of the acute phases of ischemia. A model was required that could allow myocardial ischemia to be caused while the animal was in the bore of the scanner. Chapter 4 describes the development of this model (published as Original paper: O h-Ici et al. Closed-chest small animal model to study myocardial infarction in an MRI environment in real time. Int J Cardiovasc Imaging. 2015 Jan;31(1):115-21).

Although a technique for small animal cardiac T_1 mapping had already been developed (21) (22), there remained other aspects of this imaging technique to be validated. In particular, the Small Animal Look-Locker technique is one which produces not only T_1 maps but also generates cine-MR and inversion recovery images. Chapter 5 describes the validation of these aspects of this technique against conventional small animal cine-MR techniques and staining for myocardial infarction (submitted as Original paper: O h-Ici et al. Validation of SALLI, a multimodal T_1 mapping method, for the evaluation of ventricular systolic function and late gadolinium enhancement).

Having developed the small animal model, Chapter 6 describes our studies of the acute changes in myocardial T_1 values following different periods of myocardial ischemia and reperfusion. We were able to examine the development of myocardial oedema following coronary occlusion, and then assess the effects of preconditioning on the development of myocardial oedema (submitted as Original paper: O h-Ici et al. T_1 mapping in acute myocardial ischemia/reperfusion).

We then used the closed-chest model to study the effects of myocardial ischemia on the carbohydrate metabolism in Chapter 7. We were able to detect changes in the aerobic and anaerobic metabolism of pyruvate following myocardial reperfusion, and study the duration of these changes in the first hour after reperfusion, and one week later (O h-Ici et al. Hyperpolarized Metabolic MR Imaging of Acute Myocardial Changes and Recovery Upon Ischemia-Reperfusion in a Small Animal Model. Radiology 2016 Mar;278(3):742-51).

Finally, in Chapter 8, the main achievements of this thesis are summarised, and future areas of investigation are discussed.

1.3 References:

(1) Arai, A.E., Leung, S., and Kellman, P. (2012). Controversies in cardiovascular MR imaging: reasons why imaging myocardial T2 has clinical and pathophysiologic value in acute myocardial infarction. *Radiology* **265**(1), 23-32.

(2) Croisille, P., Kim, H.W., and Kim, R.J. (2012). Controversies in cardiovascular MR imaging: T2-weighted imaging should not be used to delineate the area at risk in ischemic myocardial injury. *Radiology* **265**(1), 12-22.

(3) Fernandez-Jimenez, R., Sanchez-Gonzalez, J., Aguero, J., Garcia-Prieto, J., Lopez-Martin, G.J., Garcia-Ruiz, J.M., Molina-Iracheta, A., Rossello, X., Fernandez-Friera, L., Pizarro, G.*, et al.* (2015). Myocardial edema after ischemia/reperfusion is not stable and follows a bimodal pattern: imaging and histological tissue characterization. *J. Am. Coll. Cardiol.* **65**(4), 315-23.

(4) Kramer, C.M., Chandrashekhar, Y., and Narula, J. (2013). T1 mapping by CMR in cardiomyopathy: a noninvasive myocardial biopsy? *JACC Cardiovasc Imaging* **6**(4), 532-4.

(5) Kawai, Y., Tsukamoto, E., Nozaki, Y., Kishino, K., Kohya, T., and Tamaki, N. (1998). Use of 123I-BMIPP single-photon emission tomography to estimate areas at risk following successful revascularization in patients with acute myocardial infarction. *Eur. J. Nucl. Med.* **25**(10), 1390-5.

(6) Garcia-Dorado, D., Ruiz-Meana, M., and Piper, H.M. (2009). Lethal reperfusion injury in acute myocardial infarction: facts and unresolved issues. *Cardiovasc. Res.* **83**(2), 165-8.

(7) Menees, D.S., Peterson, E.D., Wang, Y., Curtis, J.P., Messenger, J.C., Rumsfeld, J.S., and Gurm, H.S. (2013). Door-to-balloon time and mortality among patients undergoing primary PCI. *N. Engl. J. Med.* **369**(10), 901-9.

(8) Murry, C.E., Jennings, R.B., and Reimer, K.A. (1986). Preconditioning with ischemia: a delay of lethal cell injury in ischemic myocardium. *Circulation* **74**(5), 1124-36.

(9) Crompton, M. (1999). The mitochondrial permeability transition pore and its role in cell death. *Biochem. J.* **341 (Pt 2)**, 233-49.

(10) Cung, T.-T., Morel, O., Cayla, G., Rioufol, G., Garcia-Dorado, D., Angoulvant, D., Bonnefoy-Cudraz, E., Guérin, P., Elbaz, M., Delarche, N.*, et al.* (2015). Cyclosporine before PCI in Patients with Acute Myocardial Infarction. *N. Engl. J. Med.* **373**(11), 1021-1031.

(11) Pennell, D.J., Sechtem, U.P., Higgins, C.B., Manning, W.J., Pohost, G.M., Rademakers, F.E., van Rossum, A.C., Shaw, L.J., Yucel, E.K., Society for Cardiovascular Magnetic, R.*, et al.* (2004). Clinical indications for cardiovascular magnetic resonance (CMR): Consensus Panel report. *Eur. Heart J.* **25**(21), 1940-65.

(12) Wagner, A., Mahrholdt, H., Holly, T.A., Elliott, M.D., Regenfus, M., Parker, M., Klocke, F.J., Bonow, R.O., Kim, R.J., and Judd, R.M. (2003). Contrast-enhanced MRI and routine single photon emission computed tomography (SPECT) perfusion imaging for detection of subendocardial myocardial infarcts: an imaging study. *Lancet* **361**(9355), 374-9.

(13) Wu, E., Judd, R.M., Vargas, J.D., Klocke, F.J., Bonow, R.O., and Kim, R.J. (2001). Visualisation of presence, location, and transmural extent of healed Q-wave and non-Q-wave myocardial infarction. *Lancet* **357**(9249), 21-8.

(14) Perazzolo Marra, M., Lima, J.A., and Iliceto, S. (2011). MRI in acute myocardial infarction. *Eur. Heart J.* **32**(3), 284-93.

(15) Sutton, M.G., and Sharpe, N. (2000). Left ventricular remodeling after myocardial infarction: pathophysiology and therapy. *Circulation* **101**(25), 2981-8.

(16) Masci, P.G., Schuurman, R., Andrea, B., Ripoli, A., Coceani, M., Chiappino, S., Todiere, G., Srebot, V., Passino, C., Aquaro, G.D.*, et al.* (2013). Myocardial fibrosis as a key determinant of left ventricular remodeling in idiopathic dilated cardiomyopathy: a contrast-enhanced cardiovascular magnetic study. *Circ Cardiovasc Imaging* **6**(5), 790-9.

(17) Bohnen, S., Radunski, U.K., Lund, G.K., Kandolf, R., Stehning, C., Schnackenburg, B., Adam, G., Blankenberg, S., and Muellerleile, K. (2015). Performance of t1 and t2 mapping cardiovascular magnetic resonance to detect active myocarditis in patients with recent-onset heart failure. *Circ Cardiovasc Imaging* **8**(6).

(18) O h-Ici, D., Jeuthe, S., Al-Wakeel, N., Berger, F., Kuehne, T., Kozerke, S., and Messroghli, D.R. (2014). T1 mapping in ischaemic heart disease. *Eur Heart J Cardiovasc Imaging* **15**(6), 597-602.

(19) Messroghli, D.R., Niendorf, T., Schulz-Menger, J., Dietz, R., and Friedrich, M.G. (2003). T1 mapping in patients with acute myocardial infarction. *J. Cardiovasc. Magn. Reson.* **5**(2), 353-9.

(20) Ardenkjaer-Larsen, J.H., Fridlund, B., Gram, A., Hansson, G., Hansson, L., Lerche, M.H., Servin, R., Thaning, M., and Golman, K. (2003). Increase in signal-to-noise ratio of > 10,000 times in liquid-state NMR. *Proc. Natl. Acad. Sci. U. S. A.* **100**(18), 10158-63.

(21) Messroghli, D.R., Nordmeyer, S., Buehrer, M., Kozerke, S., Dietrich, T., Kaschina, E., Becher, P.M., Hucko, T., Berger, F., Klein, C.*, et al.* (2011). Small animal Look-Locker inversion recovery (SALLI) for simultaneous generation of cardiac T1 maps and cine and inversion recovery-prepared images at high heart rates: initial experience. *Radiology* **261**(1), 258-65.

(22) Messroghli, D.R., Nordmeyer, S., Dietrich, T., Dirsch, O., Kaschina, E., Savvatis, K., O h-Ici, D., Klein, C., Berger, F., and Kuehne, T. (2011). Assessment of diffuse myocardial fibrosis in rats using small-animal Look-Locker inversion recovery T1 mapping. *Circ Cardiovasc Imaging* **4**(6), 636-40.

Chapter 2 - Overview and History of MR spectroscopy and imaging

"You know, what these people do is really very clever. They put little spies into the molecules and send radio signals to them, and they have to radio back what they are seeing."

Felix Bloch recalling Niels Bohr's description of Nuclear Magnetic Resonance.

2.1 History of Magnetic Resonance

Magnetic resonance imaging (MRI) can trace its development ultimately to spectroscopy, the study of the interaction of electromagnetic radiation with matter. Two particular developments in spectroscopy were of importance in the development of nuclear magnetic resonance (NMR). The first introduced magnetic fields into spectroscopy. It was observed by Zeeman in 1896 when he noted that a magnetic field could split the spectrum of the light emitted along the magnetic field (1). The second was the suggestion by Pauli in 1924 that atomic nuclei possess an intrinsic angular momentum (spin) and, parallel to this, a magnetic moment (2).

Following on this knowledge, in the 1940s Felix Bloch and Edward Purcell developed a series of experiments to measure this magnetic moment (3, 4). Bloch initially gave his method the name of "nuclear induction," as it allowed the signal generated by the transition of nuclei from one energy level to another to be detected as a voltage difference. This method subsequently became known as nuclear magnetic resonance.

It was first thought that a nucleus would have a specific resonance frequency, irrespective of its local chemical environment. However, in 1949 and 1950, it was found that the electron cloud surrounding the nucleus played a role in determining the resonance frequency (5). This difference became known as the chemical shift (6). It was also found that nuclei could interact with each other, or undergo spin-spin coupling, resulting in the splitting of the NMR spectra obtained (7). These discoveries moved NMR from the realm of physics into the world of

chemistry, allowing molecular structure to be studied (5, 8, 9). NMR was then adapted for the study of biological materials (10), followed by cells (11) and intact tissues (12). Some of these experiments may have been foreseen by Bloch when he placed his finger into the coil of his NMR probe and obtained a signal (13).

While protons are abundant in biological compounds, early biological NMR studies focused on phosphorus-31 (^{31}P) and carbon-13 (^{13}C) (14). The large water signal in proton NMR interfered with the study of the much smaller signals from the other proton containing metabolites. Methods were developed to suppress the signal from water, allowing the development of proton NMR. It was found that the relaxation times of red blood cells varied with the surrounding water content (15), and subsequently that the relaxation times of tissues could change over the reproductive hormonal cycle (16). It was therefore suggested that the water content in cells affected relaxation times. A search for a method to distinguish healthy from cancerous tissue led to the claim that NMR properties of healthy tissue were significantly different from those of cancerous tissue (17). In the mid-1970s, Lauterbur (18), and Mansfield (19) discovered magnetic field gradients could be used for spatial localisation of the NMR signals. This discovery allowed the development of magnetic resonance imaging (MRI). These findings were aided by the development of two-dimensional (2D) Fourier transformed NMR (20), resulting in more efficient imaging.

In its short history, NMR and MRI have evolved into essential tools in the study of chemistry, biology and medicine: from the analysis of single compounds to the current possibilities of in-vivo analysis of changes in the metabolism and water content of living tissues.

2.2 Basic Principles of MR

2.2.1 Nuclear Spin

Atoms consist of a positively charged nucleus surrounded by a negatively charged cloud of electrons. Certain nuclei, those with an odd number of protons and/or neutrons, spin on their nuclear axis. This nuclear spin **I** (21) of a positively charged object will generate a magnetic dipole, resembling a bar magnet. The magnetic dipole moment, μ and the angular momentum of a spinning nucleus, *I* are related by a fundamental nuclear constant known as the gyromagnetic ratio, γ

$$\mu = \gamma I \quad (2.1)$$

Nuclear spin ranges from 0 to 8 across the periodic table. The spin of nuclei can be predicted from their mass number. Nuclei with an odd number of protons and/or neutrons possess in their ground state a nuclear spin > 0 (22). For example, ^{1}H and ^{13}C have a spin number of ½, whereas ^{12}C has a spin of 0.

Spin is a type of angular momentum, which can be quantized into magnitude L, and a direction, m. The magnitude L is given by $\hbar\sqrt{I(I+1)}$, where $\hbar = h/2\pi$ and h is Plank's constant. The magnetic quantum number m equals $-I, -I+1, \ldots, I-1, +I$, resulting in a total number of eigenstates (spin states) of $2I+1$. These eigenstates refer to the orientation of I along the direction of an external magnetic field B_0.

2.2.2 Nuclei in a Magnetic Field

A nucleus with a magnetic moment in a magnetic field is classically compared to a spinning top, with a rotation about both its own axis and that of the external magnetic field. When a nucleus is placed in an external magnetic field, B_0, its angular momentum prevents it from aligning itself parallel to B_0. The spins will experience a torque, causing the nucleus to rotate or precess about B_0 (Figure 2-1). This can be described as:

$$\frac{d\vec{\mu}}{dt} = \gamma\vec{\mu}\times\overrightarrow{B_0} \quad (2.2)$$

The precessional frequency can be derived as:

$$\omega_0 = \gamma B_0 \quad (2.3)$$

where ω_0 is the Larmor frequency, or the frequency of the precession of the nucleus and is proportional to the magnetic field strength.

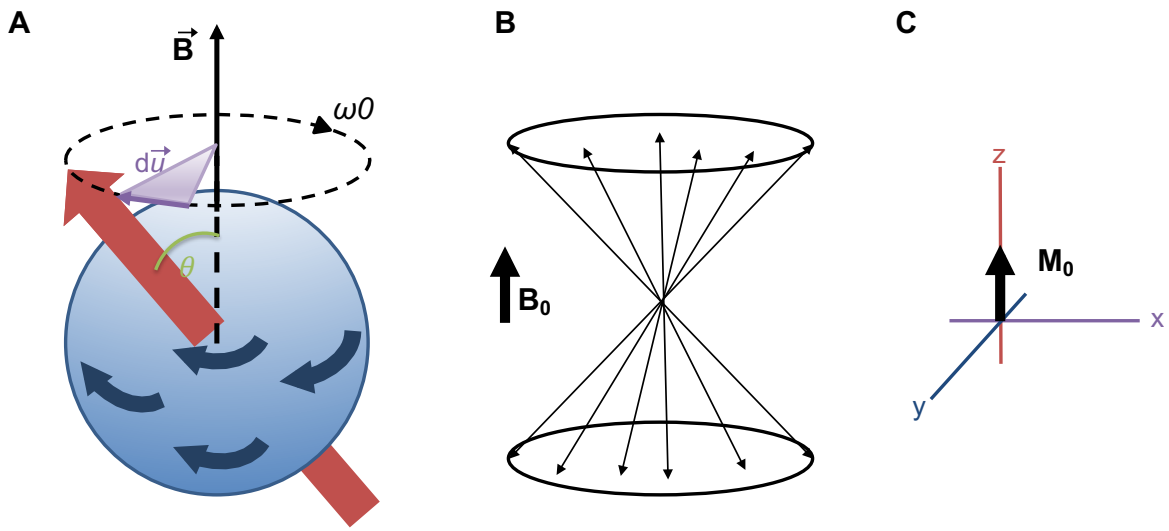

Figure 2-1. The precession of a ½ spin magnetic moment μ around a magnetic field B_0 (A). Each NMR sample will contain a large number of precessing nuclei (B). The sum of all of these spins will result in a net magnetisation vector M_0 (C).

In the absence of a magnetic field, the nuclear spins will be randomly aligned, and have no net magnetic vector. When placed into a magnetic field, the spins will tend to align parallel or anti-parallel with B_0. These spin states are known as nuclear Zeeman levels (Figure 2-2). For I = 1/2 spins, there are two equidistant energy levels in a magnetic field B_0:

$$E = \pm\mu B_0 = \pm\tfrac{1}{2}\gamma\hbar B_0 \qquad (2.4)$$

The spin states can be referred to as “up” or “down”, the low energy (α) and high energy (β) states respectively. From equation 2.4 it can be seen that the energy difference between the spin states is

$$\Delta E = \gamma\hbar B_0 \qquad (2.5)$$

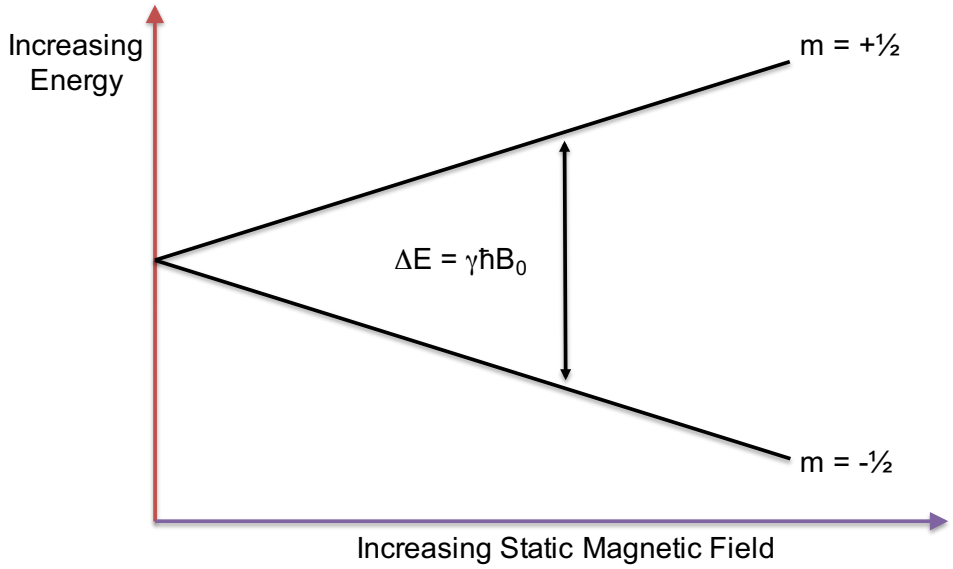

Figure 2-2. Nuclear Zeeman levels for a nucleus with spin ½. $\Delta E = \gamma \hbar B_0$

Therefore, if B_0 or γ increase, ΔE will increase. The low sensitivity of proton NMR results from the small energy difference between the two energy states of the proton. In comparison, the γ of an electron is approximately 660 times larger. This property is exploited in the field of dynamic nuclear polarisation addressed later in this chapter (22, 23). γ is different for each nucleus. Nuclei with larger γ can absorb/emit more energy and are therefore more sensitive for the purposes of NMR. This sensitivity is proportional to γ^3. The gyromagnetic ratios of nuclei of most interest in biological NMR are given in **Table 2-1** (21).

Isotope	**Spin Quantum Number I**	**Gyromagnetic Ratio γ/107 (rad T^{-1} s^{-1})**	**Resonance frequency at B_0= 1T (MHz)**	**Natural Abundance (%)**	**Relative MR Sensitivity in Comparison with ^{1}H (%)**
^{1}H	½	26.752	42.577	99.985	100.0
^{2}H	1	4.1066	6.536	0.015	0.96
^{12}C	0	–	–	98.89	–
^{13}C	½	6.7283	10.708	1.11	1.59
^{16}O	0	–	–	99.76	–
^{19}F	½	25.181	40.077	100.0	83.34
^{31}P	½	10.841	17.254	100.0	6.63

Table 2-1. NMR properties of selected nuclei used in biological NMR and MRI (24)

It can be seen from Table 2-1 that spectroscopy of ^{13}C is limited in comparison to hydrogen by its low natural abundance and its lower gyromagnetic ratio. The ^{12}C isotope of carbon and the ^{16}O isotope of oxygen have a spin of 0 and cannot be observed by NMR spectroscopy.

The energy difference between the two population states is what enables NMR. If energy is supplied in the form of electromagnetic radiation of the correct frequency, this can cause the nuclei to flip from the lower energy state to the higher state. This phenomenon is known as nuclear magnetic resonance.

2.2.3 Polarisation

To generate a signal from NMR, the population of spins in the lower energy state must be greater than that of the higher energy state. The lower energy spins can then be excited, leading to an NMR signal. The difference in the spin states (spin excess), parallel (α) or anti-parallel (β) to the external magnetic field is known as polarisation. The larger the polarisation, the larger the potential NMR signal. Polarisation varies with thermal equilibrium and is given by the Boltzmann distribution:

$$\frac{n\alpha}{n\beta} = \exp\left(\frac{\Delta E}{kT}\right) \tag{2.6}$$

where $n\alpha$ and $n\beta$ denote the population in each energy state, ΔE is the energy difference, k is the Boltzmann constant, and T is absolute temperature. From the equation, it can be seen that polarisation increases as absolute temperature decreases, or as field strength increases.

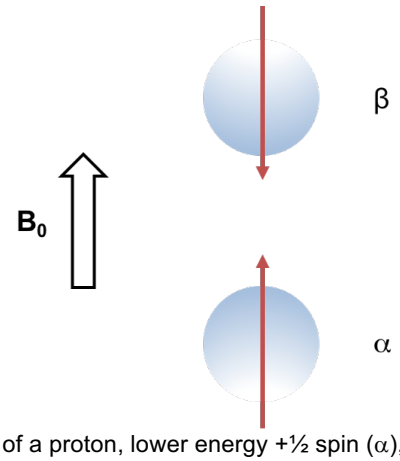

Figure 2-3. The two energy states of a proton, lower energy +½ spin (α), and higher energy -½ (β) spin.

At thermal equilibrium, this spin excess is very small and can be calculated. As $\gamma\hbar B_0 \ll kT$ at room temperature and typical magnetic field strengths, equation 2.6 can be rewritten as

$$\frac{n\alpha}{n\beta} = 1 + \frac{\gamma\hbar B_0}{kT}$$

With this rewritten equation, polarisation can then be calculated. At room temperature and 1.0T, the number of excess protons in the low energy state is 3 per million, 3 x 10^{-6}. Although the relative difference between spin states is very small, the absolute difference of spins in a sample will be very large. In-vivo MRI is possible as humans are made up predominantly of water (the heart is made of 73% water (25)). Each water molecule has 2 protons, with large numbers of protons (10^{21}) in a typical MRI voxel. This results in 3 x 10^{-6} x 10^{21} or approximately 3^{15} protons in the low energy state, a sufficient amount to generate a signal. ^{13}C spectroscopy is limited by the low γ (Table 2-1) and much lower natural concentrations of the ^{13}C nucleus (1.1%). At room temperature and a magnetic field strength of 3 T, the ^{13}C spin polarisation is 2.47 ppm (26).

2.2.4 Net Magnetisation

For a sample containing many spins, there will be more spins aligned with B_0, (parallel – low energy, α) than in the higher energy state (antiparallel – high energy, β) (Figure 2-3). The sum of all the spins will form a single net macroscopic magnetisation along the longitudinal plane (Figure 2-1) (26). This 'longitudinal equilibrium magnetisation' M_0 for the vector of the magnetic moment along the external field direction can be calculated. For n spins, M_0 is determined by the magnetic moment component of each spin multiplied by the net population difference:

$$M_0 = \frac{n\gamma^2\hbar^2}{4kT}B_0 \qquad (2\text{-}7)$$

For in vivo studies, neither body temperature nor spin density can be changed, meaning that under normal conditions, M_0 can only be increased by increasing B_0.

2.2.5 Magnetisation

An NMR sample will contain a large number of spins. These spins will form two cones, parallel and anti-parallel (Figure 2-1). For simplicity, we align the z-axis with the external magnetic field. As there are more spins in the low-energy parallel state, we can reduce this to one cone precessing parallel to B_0. As each spin will be randomly assigned along the surface of the cone, the transverse vector of the spins will cancel itself out. This results in a single vector M, along the z-axis. The magnetisation vector M can be described as the sum of motion for the individual spins:

$$\frac{d\vec{M}}{dt} = \gamma\vec{M}\times\vec{B} \quad (2.8)$$

This expression forms the basis of the Bloch Equations (3, 27) and illustrates the interaction of spins with external magnetic fields.

2.2.6 Excitation

Before the magnetisation can be detected and measured, it must first be tilted into the transverse (xy) plane to allow for induction using a current loop placed perpendicular to the main magnetic field axis. This tilting is achieved by applying an RF pulse at the Larmor frequency of the nucleus of interest. This pulse creates a secondary magnetic field B_1 in the xy plane. This B_1 is a circularly polarised radio frequency (RF) field (Figure 2-4) that can be described as:

$$\vec{B}(t) = B_1 cos\omega t\vec{x} + B_1 sin\omega t\vec{y} \quad (2.9)$$

M_0 will spiral away from the z-axis towards the xy-axis, precessing around the B_0 axis with a frequency ω_0 and around the B_0 axis with $\omega_1 = \gamma B_1$ (Figure 2-4). The Bloch equation describes the behaviour of the macroscopic magnetisation vector as a result of the magnetic interactions with B_1 and B_0 (3, 27, 28):

$$\frac{d\vec{M}}{dt} = \gamma\vec{M}\times(\vec{B}_0 + \vec{B}_1) \quad (2.10)$$

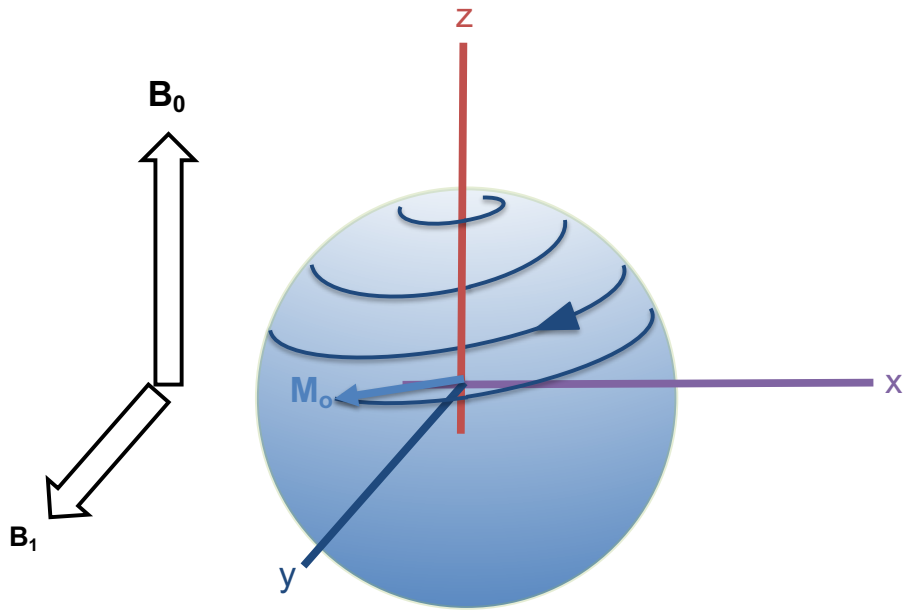

Figure 2-4. The circularly polarised field of B_1 is applied perpendicularly to B_0. Seen from a rotating frame of reference (Figure 2-5), the magnetisation vector experiences B_1 as a static field when B_1 oscillates "on resonance", with ω_0.

The angle to which M_0 is tilted, known as the flip angle, α is determined by the duration t and the strength of B_0

$$\alpha = \gamma B_1 t \tag{2.11}$$

A rotating system of reference is used to simplify the understanding of nuclear excitation. This coordinate system rotates around B_0, or z, at the Larmor frequency of the nucleus of interest. In this rotating frame, the axes have the notation x', y', z'. Now, rather than a complex circular rotation, B_1 apears as a simpler stationary force along x'.

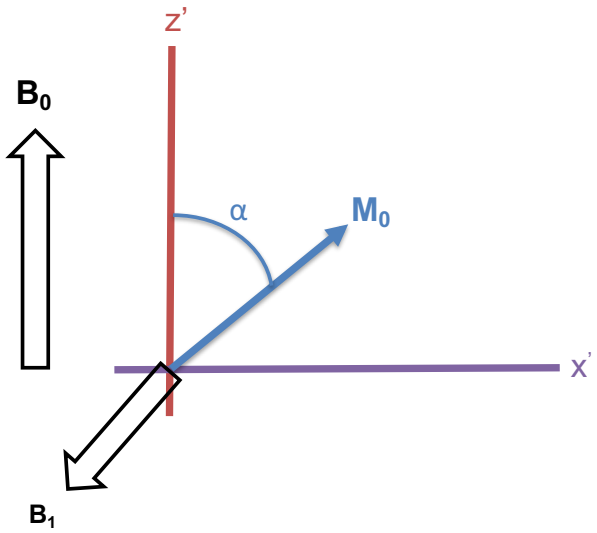

Figure 2-5. In the rotating frame of reference, the z-axis is parallel to magnet field B_0 while the x' and y' axes rotate about the z-axis at the Larmor frequency.

2.2.7 Relaxation

Following the application of the radiofrequency (RF) pulse, the magnetisation will return to thermal equilibrium in a process known as relaxation. This consists of two separate processes occurring simultaneously, but at different rates; the recovery of longitudinal magnetisation M_z, and loss of transverse magnetisation M_{xy}. Each of these has its own time constant, which can be described by:

$$\frac{dM_z(t)}{dt} = \frac{M_0 - M_z(t)}{T_1} \tag{2.12}$$

$$\frac{dM_{xy}(t)}{dt} = \frac{-M_{xy}(t)}{T_2} \tag{2.13}$$

where T_1 is the time constant required to recover 63% of longitudinal relaxation following a 90° pulse. T_2 the time taken to loose 63% of the transverse magnetisation following a 90° pulse.

Following excitation, excited spins gradually return to their thermal equilibrium or Boltzman distribution. This process involves the release of energy, as the excess is lost in interactions between the spin and the molecular environment or lattice. The rate of this recovery can be given by:

$$M_z(t) = M_z(0)e^{-t/T_1} + M_z(1 - e^{-t/T_1}) \qquad (2.14)$$

Immediately following an excitation pulse, the spins in the xy plane are in phase. Spins will interact with one another, with local magnetic field variations, resulting in slight changes to the speed of precession. As a consequence, spins become gradually out of phase. This interaction will occur many times for each spin. This loss of phase results in loss of transverse magnetisation (Figure 2-6)

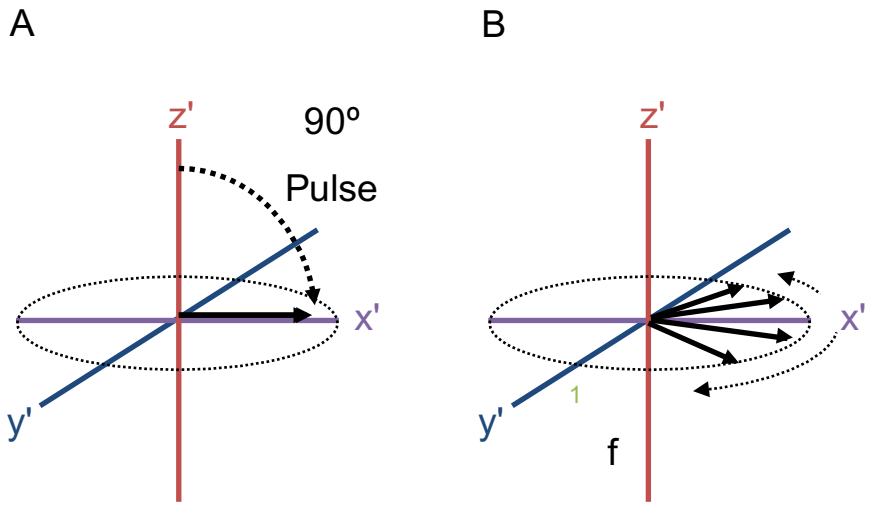

Figure 2-6. Dephasing of spins in the xy plane following a 90° pulse.

The dephasing that occurs solely due to spin-spin interactions is known as T_2. It, unlike spin-lattice relaxation, does not involve loss of energy (there is no change of energy states of spins, merely dephasing). The decay of transverse magnetisation due to T_2 can be described as follows:

$$M_{xy}(t) = M_{xy}(0)e^{-t/T_2} \qquad (2.15)$$

However, the magnetic field fluctuations experienced by spins do not only include dipolar field variation resulting from spin-spin interactions. The external magnetic field B_0 itself will not be completely homogenous. The lack of homogeneity will result in local magnetic field variations, as spins experience different local field strengths. This external inhomogeneity is added to the internal inhomogeneity, resulting in increased dephasing and shorter relaxation times. This observed M_{xy} relaxation is known as T_2^* and can be described using:

$$\frac{1}{T_2^*} = \frac{1}{T_2} + \gamma \Delta B_0 \tag{2.16}$$

where $\gamma \Delta B_0$ indicates the effect of tissue susceptibility and static field inhomogeneities. The magnetisation lost to T_2^* can be recovered using a technique known as spin-echo is described below (Section 2.3.2).

2.2.8 Relaxation Times in Biological Tissues

Relaxation times in fluids and solids vary significantly. These variations are due to the fact that each nucleus has a changing magnetic environment, with interactions between the magnetic moments of nearby electrons, nuclei and molecules. A local field results that can be described using the spectral density function *J* (ω):

$$J(\omega) = \frac{\tau_c}{1+\omega^2 {\tau_c}^2} \tag{2.17}$$

Where τ_c is the correlation time, a value that represents the average time it takes one molecule to rotate by one radian. Anything that can allow faster rotation, such as molecule size, viscosity or temperature will result in shorter τ_c. The relationship between τ_c and relaxation rates for two protons is given by the Solomon-Bloembergen equations for proton-proton interaction:

$$R_1 = \frac{1}{T_1} = \frac{6\hbar\gamma^4}{20r^6}\{J(\omega) + 4J(2\omega)\} \tag{2.18}$$

$$R_2 = \frac{1}{T_2} = \frac{3\hbar\gamma^4}{20r^6}\{3J(0) + 5J(\omega) + 2J(\omega)\} \tag{2.19}$$

where (*r*) is the distance between the spins.

T_1 times, therefore, will differ if the sample studied is in solid or liquid form. T_1 is longer in solids than pure liquids. Also, if the correlation time is close to the Larmor frequency, this will allow

energy transitions to occur, resulting in shorter T_1 times. This factor also means that T_1 will vary with field strength.

From equation 2.19, it can be seen that $T_2 \leq T_1$ as T_2 relaxation contains the contribution from an additional low-frequency component relative to T_1 relaxation. Considering spectral density, a rapidly tumbling molecule will experience a local magnetic field that averages out quickly. A molecule that tumbles more slowly will experience the field homogeneities for longer, and become more rapidly out of phase. In contrast to T_1, T_2 does not vary widely with field strength.

The relaxation constants of different biological tissues will, therefore, depend on the state of mobility of the protons and molecules that contribute to the proton signal. In general, the protons in water play the most important role, as the body is made up predominantly of water. Pure liquids like CSF will have long T_1 values and tissues with higher water contents will, in general, have longer T_1 values. For example, the medulla of the kidney, with a higher water content, has a longer than the cortex (29). The protons in fat tumble close to the Larmor frequency, resulting in a short T_1 for fatty tissue, and shorter T_1 for tissues containing large amounts of fat such as bone marrow (29).

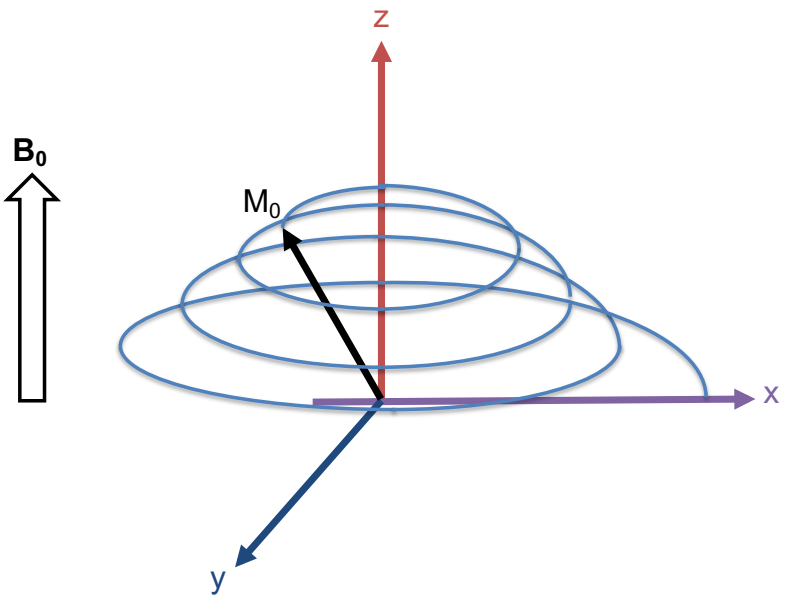

Figure 2-7. The precession and relaxation of the magnetisation after a 90◦ excitation as it relaxes in the longitudinal and transverse planes.

2.2.9 Detection of the MR signal - Fourier Transform NMR

Following an RF pulse, magnetisation is tilted into the transverse plane. The resulting magnetisation can be detected with tuned RF coils using Faraday's principle. The oscillating signal will decay over time due to the transverse relaxation processes described above (Figure 2-7). This signal is known as the free induction decay (FID) and can be described by

$$FID = [\sin \omega_o t]\, e^{-t/T2^*} \quad (2.20)$$

The coils used to detect the signal are in the x and y planes, allowing the complex signal along both components to be simultaneously detected:

$$S = Sx + i\, Sy \quad (2,21)$$

where S represents the signal detected and i represents the square root of -1. As described before, the signal will decay with T_2^*. The two signals acquired are cosine and sine functions of the offset frequency $\Omega = \omega_0 - \omega$. Following a short RF pulse creating flip angle θ, the magnetisation components for each plane after the pulse can be derived using the Bloch equation (Eq. 2.10) and are given by:

$$M_x(0) = 0$$

$$M_y(0) = M_0 sin\theta$$

$$M_z(0) = M_0 cos\theta \quad (2.22)$$

The spin then precesses around B_0 and undergoes relaxation. Therefore, the magnetisation components after an excitation are:

$$M(t) = M_0 cos\theta e^{-\frac{t}{T1}} + M_0(1 - e^{-\frac{t}{T1}}) \quad (2.23)$$

2.3 Measurement of Relaxation Time Constants

Knowledge of the time constants T_1 and T_2 or T_2^* is essential, as they will affect the signal obtained by magnetic resonance and the pulse sequence parameters used to study the sample. As such, there has been interest in measuring these since the earliest days of NMR (15, 30). For

hyperpolarised ^{13}C experiments, the T_1 value describes the rate of loss of measureable hyperpolarised signal. A longer T_1 allows the signal of a hyperpolarised tracer to be studied in in-vivo experiments.

2.3.1 T_1 Measurements

The conventional methods to measure T_1 include the inversion recovery experiment with an initial 180° inversion and the saturation recovery experiment with a 90° excitation pulse (Figure 2-8). The inversion recovery sequence is the gold standard for the determination of T_1 relaxation times (31). This time can be calculated using:

$$M_z(t) = M_0(1 - \alpha e^{-\frac{t}{T_1}}) \qquad (2.24)$$

Where t is the inversion time (TI) for an inversion recovery experiment (180° pulse), or TR for a repetition time for a saturation recovery measurement (90° pulse). α = 2 for an inversion recovery measurement or α = 1 for a saturation recovery measurement. If the experiment is repeated with different TI/TR, different FIDs will be acquired. These can then be fitted using equation 2.24, allowing the calculation of T_1. In general, the delay time between two consecutive excitations should be $t \geq 5T_1$ to allow for at least 99% of signal recovery. The inversion recovery results in longer scan times as more time is needed for M_z to recover fully before another excitation can be performed. Using a saturation pulse rather than an inversion pulse (Figure 2-8) results in shorter repetition times (TR) as the recovery only occurs from 90º. The shorter TR significantly reduces the scan duration.

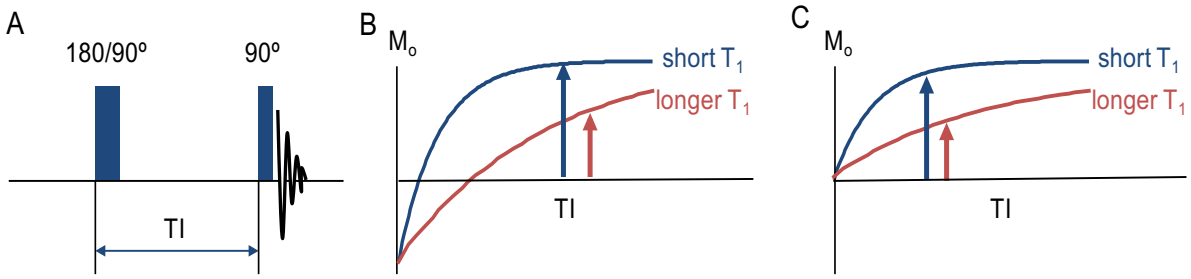

Figure 2-8. T_1 relaxation can be measured using the inversion recovery (180º/90º) or saturation recovery (90º/90º) method (A). Magnetisation relaxes to thermal equilibrium value M_0 over time constant T_1 Different tissues will relax at different rates. Using a variety of inversion times (TI), the recovery of M_0 can be sampled and fitted to the expression for M_0 recovery (B). A similar experiment performed using saturation recovery (C).

2.3.2 T_2 Measurements

After RF excitation field inhomogeneities and spin-spin interactions will cause spins to precess at slightly different Larmor frequencies. These different precession frequencies result in a loss of phase coherence as described in equation 2.25. The spin echo method allows the separation of the effects of T_2 and magnetic field inhomogeneity (32). In a spin echo sequence (Figure 2-9, Figure 2-10) the magnetisation is tipped to the transverse plane by a 90° pulse. The magnetisation begins to lose coherence in the transverse plane because of the processes described above. After a delay of $T_E/2$ a 180° pulse is applied. Dephasing is reversed, causing the spins to come together following another a delay of $T_E/2$ generating a spin echo. The echo time T_E refers to the time taken from the 90° pulse to the echo generation. By measuring the signal from different T_E experiments, T_2 can be calculated by fitting the signal intensities as a function of T_E to the following equation:

$$M_{xy}(t) = M_{xy}(0)e^{-T_E/T_2} \qquad (2.25)$$

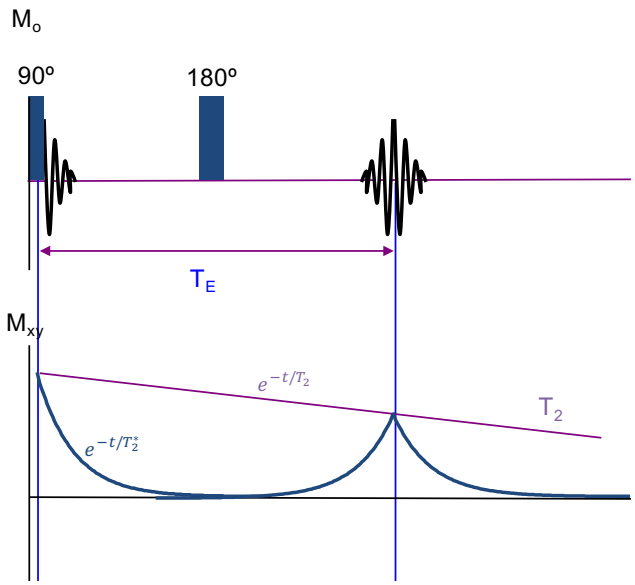

Figure 2-9. Above: A typical spin-echo experiment with a 90º and 180º pulse. Below: The decay of the transverse magnetisation with T_2^* can be seen, followed by the regeneration of the signal following the 180º pulse. This technique allows the measurement of T_2.

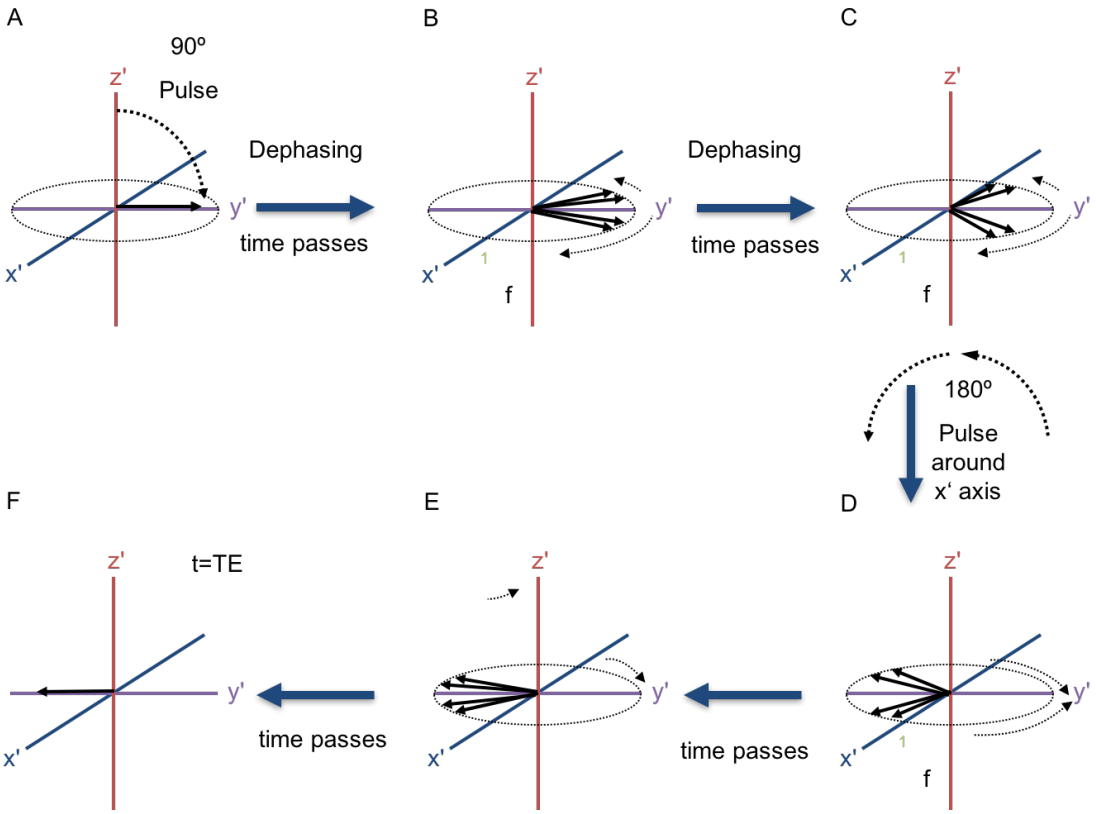

Figure 2-10. Spin-echo Diagram. (A) A 90° pulse tilts the spins into the transverse plane. (B), (C) The spins progressively dephase in the first half of the echo time $T_E/2$. This dephasing in the transverse plane has a time constant T_2^* A 180º pulse refocuses the magnetisation vectors. (D), (E) The spins rephase again over $T_E/2$. (F) Following T_E, the spins have rephased and an echo is formed.

2.3.3 Look-Locker Method

The multiple-readout method was developed by Look and Locker to overcome the necessity for a long relaxation period between inversion pulses (Figure 2-11) (33). Following an inversion pulse (to maximise the dynamic range from +1 to -1), a train of low-flip-angle readout pulses is used to sample the magnetisation as it relaxes exponentially toward equilibrium**.** A continuous acquisition of image data is necessary for this method. However, cardiac motion means that this method is unsuitable for cardiac studies. To address this issue, the modified Look-Locker inversion recovery (MOLLI) was developed.

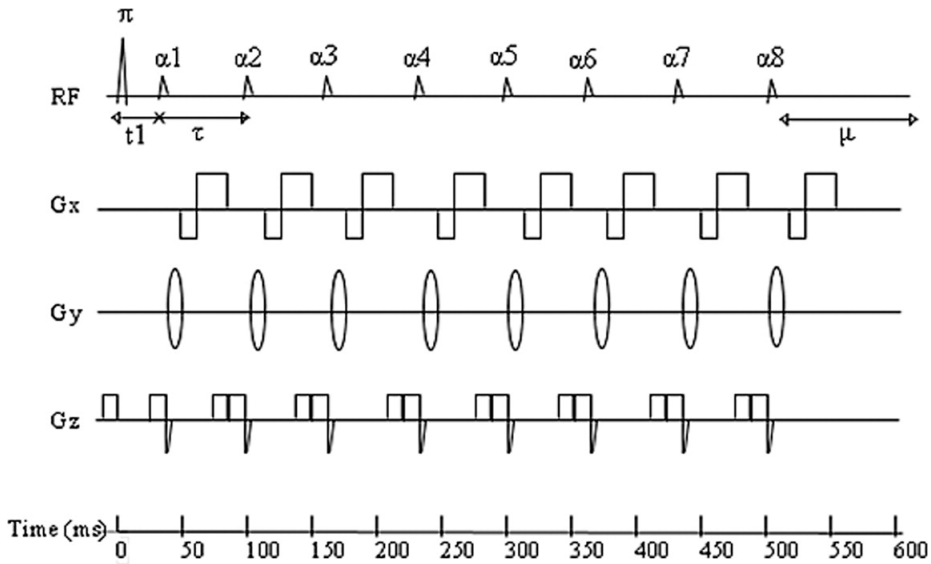

Figure 2-11. Look-Locker inversion recovery pulse sequence diagram. A nonselective 180° inversion pulse (π) is used, which is followed by multiple small flip angle pulses (α). These are separated by time (τ) and sample the longitudinal signal magnetisation as it recovers to steady state. μ = undisturbed recovery period. From (34), used with permission.

2.3.4 Modified Look-Locker Inversion Recovery

The MOLLI pulse sequence merges data from three consecutive inversion recovery (IR) experiments into one data set generating single-slice T_1 maps of the myocardium (Figure 2-12) (35). The image acquisition is gated to the electrocardiogram (ECG). It generates high spatial resolution single-slice T_1 maps (2.0 x 2.0 mm^2 in-plane). The potential clinical use of MOLLI has been shown in patients with both acute and chronic myocardial infarction (36, 37). MOLLI uses non-segmented acquisitions of 150–200 msec for each raw image. This technique can generate good quality end-diastolic images for heart rates up to 100 beats per minute (38). This technique is not suitable for the high heart rates of small animals (200–600 beats per minute). The SALLI (Small Animal Look-Locker Inversion recovery) technique was developed to overcome this problem (39).

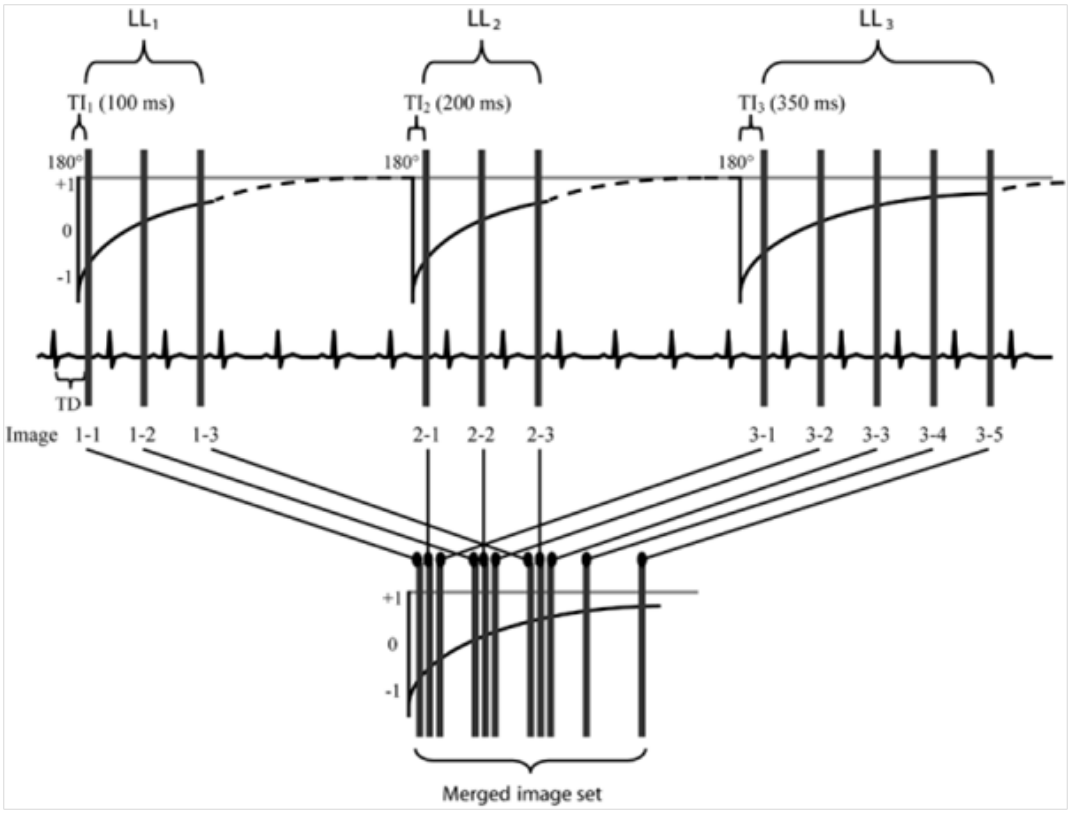

Figure 2-12. MOLLI pulse sequence. LL1 - signal is sampled at end diastole for three consecutive cardiac phases following an inversion pulse where magnetisation recovers with a time constant T_1^* solid line) following an inversion pulse. Next comes a period of relaxation, (dashed line) where magnetisation recovers with T_1 (dashed line). Following this relaxation period, the signal is again sampled for three (LL2) heartbeats with another relaxation period, before the final acquisition of data for four heartbeats (LL3). Imaging occurs within a single breath hold, and the data is regrouped into a merged imaged set according to the T_1. From (35), used with permission of the publisher.

2.3.5 SALLI

SALLI uses a segmented, ECG-gated, inversion recovery prepared Look-Locker–type pulse sequence to generate a data set. This data set can be used to reconstruct T_1 maps, cine images, and inversion recovery images. A segmented approach allows the acquisition of T_1 maps at end-diastole at high heart rates. Acquisition times are increased to allow this, with the additional time is used to generate cine and inversion recovery images. Temporal undersampling and radial non-balanced steady-state free precession are used to enable an acceleration of data acquisition and reduction of motion artefacts respectively. The technique is further explained in Figure 2-13 and Figure 2-14.

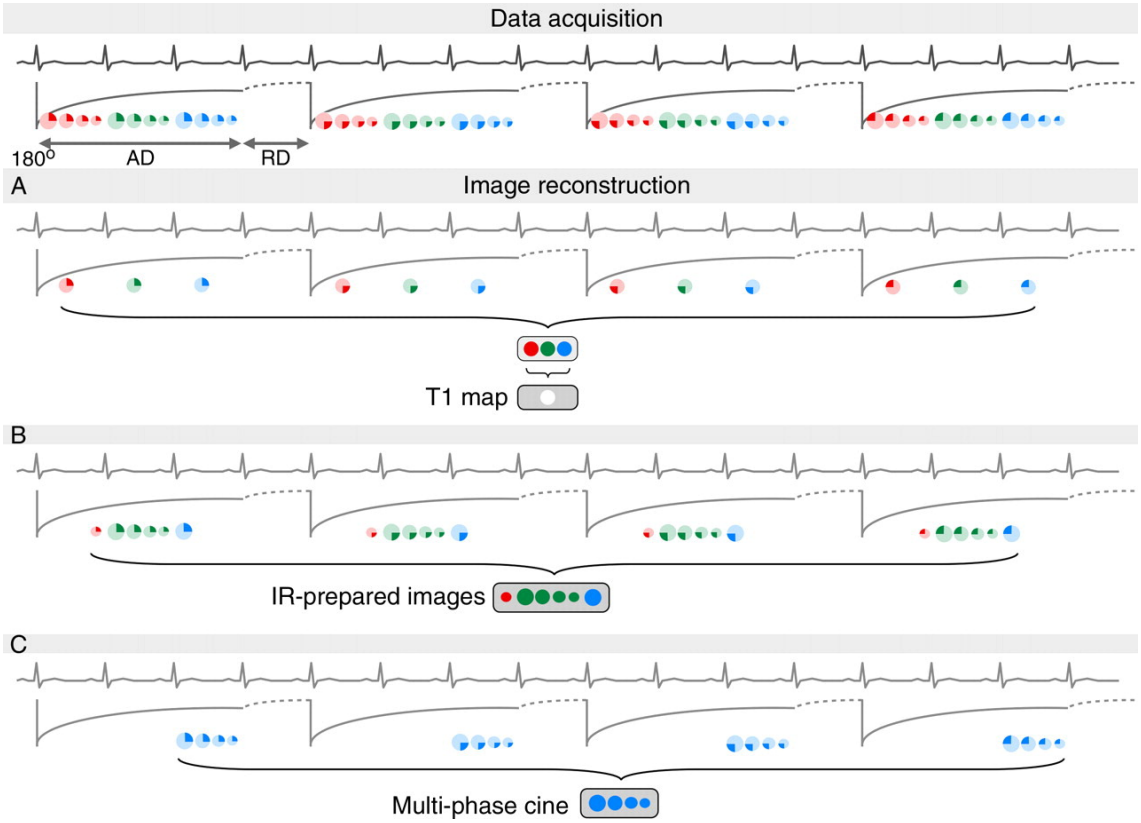

Figure 2-13. SALLI pulse sequence of fully sampled data sets and reconstruction schemes. From (39), used with publisher's permission.
Top: SALLI pulse sequence. Following an inversion pulse, signal is sampled for consecutive cardiac phases and while magnetisation recovers with a time constant T_1^* (solid line) following an inversion pulse (acquisition duration - AD). Next comes a defined period of relaxation, (relaxation duration - RD) where magnetisation now recovers with T_1 (dashed line). This process is repeated for each radial segmental acquisition. T_1^* refers to the readout induced deviation of the magnetisation recovery curve caused by the sampling of the magnetisation.
A: T_1 maps reconstruction. The raw data is reconstructed using pixel-wise nonlinear curve fitting with a correction for T_1^*.
B: IR-prepared image reconstruction. Images with predefined inversion times are reconstructed from the image data.
C: Cine images reconstruction. Images are reconstructed from the data available after the time point where T_1 has recovered by at least 90%. The number of cardiac phases can be specified beforehand.

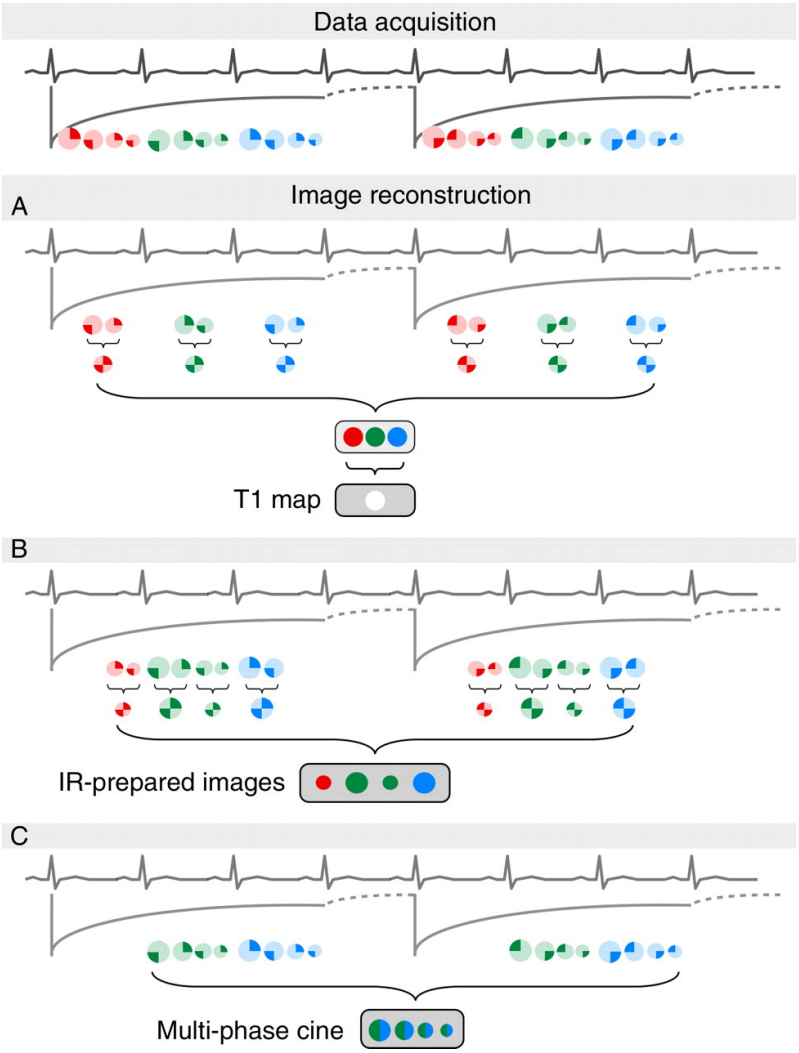

Figure 2-14. SALLI pulse sequence scheme with temporally undersampled data acquisition (top) and image reconstruction (A – C). From (39), used with publisher's permission.
Top: Data for each radial segment are acquired every second phase of one heart cycle (for a temporal undersampling factor of two). Image acquisition is reversed in the following heart cycle.
A. T_1 maps are generated by combining data from neighbouring phases.
B. IR-prepared images are generated in the same fashion
C. Data from neighbouring heart cycles are combined, providing full data sets that can offer the same temporal resolution as fully sampled data sets.

2.4 Chemical Shift

Nuclei within the same molecule can have individual chemical environments (8) which will affect the resonance frequency ω of the nucleus. The distribution of electrons around the same type of nucleus (e.g. ^{1}H, ^{13}C) will vary because of local factors, such as binding partners, bond lengths, and the angles between bonds. These electrons will interact with the local magnetic field. Electrons, having an opposite charge to the proton, will precess about B_0 in the opposite direction. They will, therefore, induce an additional local magnetic moment at the nucleus shielding the external field B_0 (Figure 2-15).

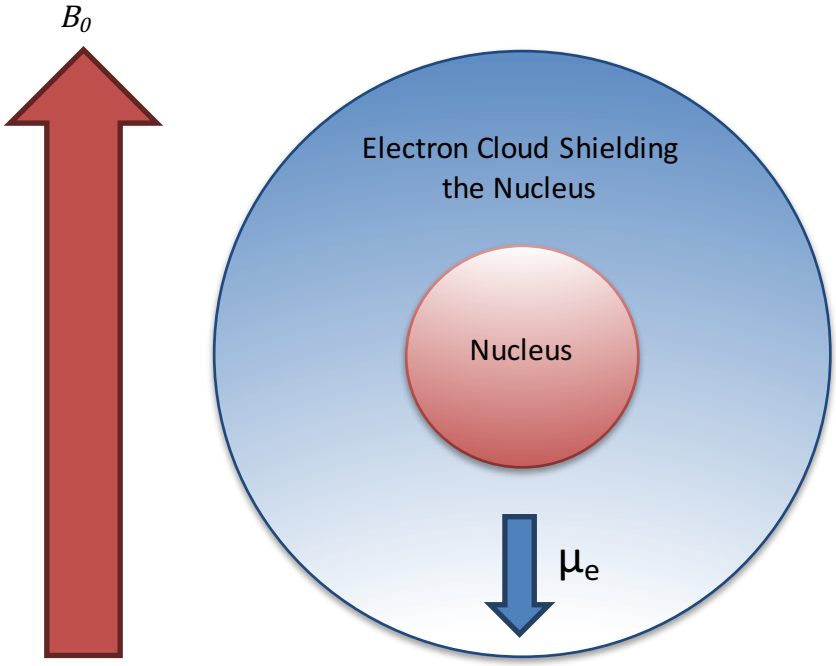

Figure 2-15. The secondary magnetic field generated by the electrons "shields" the nucleus from the effects of the external magnetic field.

The actual magnetic field experienced by the nucleus can be described by the shielding constant σ:

$$\vec{B} = \vec{B}_0(1 - \sigma) \qquad (2.26)$$

σ is a dimensionless constant that represents the difference between local and external magnetic fields. σ will differ depending on the arrangement of electrons around the nucleus in question. The actual Larmor frequency, therefore, reflects the real magnetic field experienced by the nucleus, and not the external magnetic field. The resonance condition for nuclei is:

$$\omega_0 = \gamma B_0(1 - \sigma) \quad (2.27)$$

In practice, the absolute value of the change in frequency cannot be easily measured. The resonance frequency ω is then compared to that of a standard compound ω_{ref}.

$$\delta = \frac{\omega - \omega_{ref}}{\omega_{ref}} \times 10^6 \quad (2.28)$$

This chemical shift δ provides information how atoms are bound within a molecule and is expressed in parts per million (ppm). The shifts in ppm are hence independent of magnetic field strength.

2.5 Spectroscopy

2.5.1 Spatial Localisation

The simplest way to localise a slice is to use an additional magnetic field with a spatial gradient (Figure 2-16). The gradient is generated by varying the strength of the magnetic field along an axis of interest. When RF excitation with a given bandwidth is performed, only the spins fulfilling the resonance condition will be excited. The spin frequency ω of a particular nucleus with a position x in a sample is:

$$\omega(x) = \gamma(B_0 + G_x x) \quad (2.29)$$

where γB_0 is the Larmor frequency ω_0. The gradient G allows the selection of a slice perpendicular to that gradient. At the centre of the gradient x will equal 0, and the spins will resonate at the Larmor frequency. The slice position is determined by the centre frequency of the RF pulse (Figure 2-16). For a bandwidth of frequencies $\Delta\omega$, the spatial displacement Δx of the acquired signal is given by:

$$\Delta x = \Delta\omega/(\gamma G_x) \quad (2.30)$$

where G_x is a gradient along x.

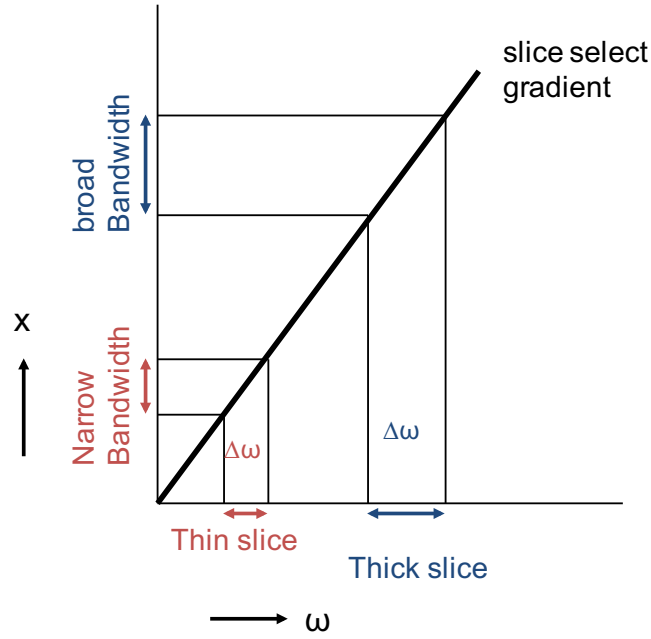

Figure 2-16. Slice selection using magnetic field gradients. The variation in magnetic field strength across the field of view results in a corresponding change in the resonance frequencies. Therefore, a slice along an axis can be selectively excited. The position and thickness of this slice can be varied using the strength of the gradient and the radio-frequency offset.

2.5.2 Single Voxel Spectroscopy

There are a number of different techniques for signal localisation in MR spectroscopy, including the stimulated echo acquisition mode (STEAM) (40) and point-resolved spectroscopy (PRESS) (41) (Figure 2-17) Chemical-shift-selective (CHESS) pulses are applied to suppress the unwanted water signal. Both STEAM and PRESS involve the use of 3 slice selective RF pulses to select a voxel. The size, shape and location of the voxel can be adjusted (Figure 2-17).

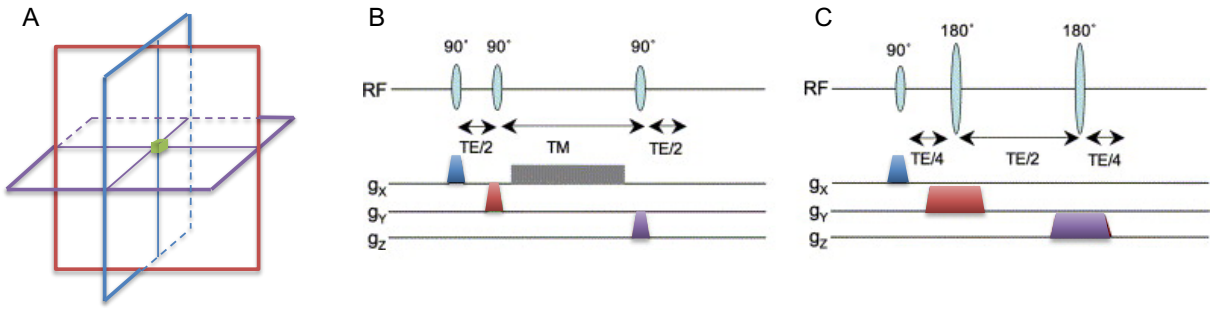

Figure 2-17. Single-voxel localization techniques. (A) Slice-selective RF pulses in the x, y and z-directions will result in a central voxel of interest. (B) The STEAM sequence consists of three orthogonal 90° slice selective pulses (C). The PRESS sequence is a double spin echo sequence, with orthogonal slice pulses of 90°, 180°, 180°.

In the case of STEAM, three orthogonal 90° slice selective pulses are used. The stimulated echo is recorded from a voxel intersected by the three slices. The initial 90° pulse is followed by a

spoiler gradient to dephase the magnetisation in the xy plane. The second 90° pulse rotates the magnetisation at the intersection of the two slices with the z-axis, thereby allowing the magnetisation to be "stored". A spoiler pulse is used to eliminate the transverse component, leaving only magnetisation along the z-axis. The third 90° pulse tips this magnetisation back into the transverse plane where it refocuses to generate the simulated echo. The stimulated echo loses half the available equilibrium magnetisation due to the isotropic distribution of the spin following the 1st pulse. The T_E of this stimulated echo is twice the time interval between the 1st and 2nd 90° pulses.

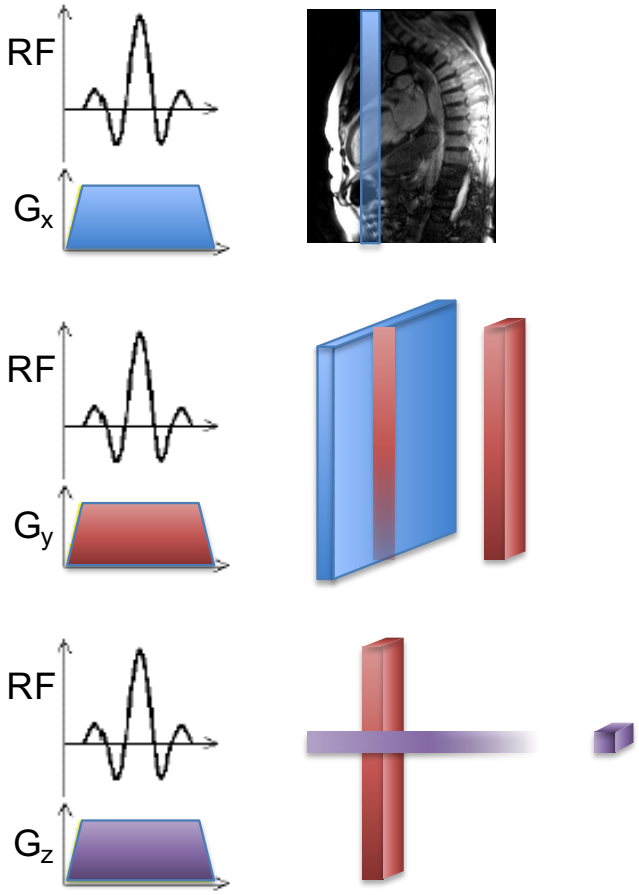

Figure 2-18. Anatomic ^{1}H images are used for localizing the volume of interest (VOI). Localization is achieved by sequential selection of three orthogonal slices. The size and location of VOI can be easily controlled.

PRESS is based on the spin-echo technique. Three pulses are used, a 90° pulse to generate transverse magnetisation, a 180° pulse to refocus this magnetisation, and a second refocusing 180° pulse. The voxel of interest is the volume that experiences all three pulses. This technique generates a signal twice the amplitude of the stimulated echo, and, therefore, has a higher signal to noise ratio. Paired spoiler gradients are used to eliminate inadvertent transverse

magnetisation. PRESS can be used for both long and short T_E applications. The choice of T_E plays a significant role in the spectrum detected. A longer T_E will select the metabolites with longer T_2, whereas a shorter T_E will generate more peaks, with a resultant more complex spectrum for interpretation.

2.5.3 Magnetic Resonance Spectroscopic Imaging

Similar to MRI, magnetic resonance spectroscopic imaging (MRSI) uses frequency and phase encoding to localize the signal (42). The use of slice selection and spatial encoding techniques in MRSI was first demonstrated by Brown et al. in 1982 (43). A volume of interest (VOI) is selected with the use of magnetic field gradients (Figure 2-18). The VOI selection is followed by a phase gradient in 1, 2 or 3 dimensions. These gradients are then turned off, and the signal is acquired as a FID or spin echo. The process is repeated to generate a full data set of phase encoded signals, which are then Fourier transformed to generate spatial and frequency data.

The MRSI technique using phase-encoding is time-inefficient as for an n-dimensional image, with m pixels in each direction, the acquisition will require n x m phase-encode experiments. To avoid T_1 weighting, a T_R of greater than five times the T_1 will be needed. Therefore, the practical resolution of this technique is limited.

2.5.4 Echo Planar Spectroscopic Imaging

An important step towards rapid MR imaging was the introduction of echo-planar imaging (EPI), first proposed by Mansfield in 1977 (44). This development led to the first human images published by the same group in 1983 (45). EPI is essentially the combination of two 1D localization methods, with frequency encoding in one direction and phase encoding in the other direction (Figure 2-19). The advantage of EPI is that it allows multiple lines of k-space to be filled following each RF pulse. If k-space is completely filled following a single excitation, the technique is called “single-shot” EPI. In this case, the time required to fill k-space will equal 1 TR. As the k-space is being sampled, the echoes will decay with T_2^*. If the acquisition time is much greater than T_2^* the signal will have decreased considerably from the start of the acquisition to the finish, leading to different weighting across k-space. To ensure homogenous k-space weighting, the entire acquisition must occur very rapidly, placing significant demands on the gradients of the MR system. An alternative to this is to divide the acquisition, a technique known as multi-shot EPI.

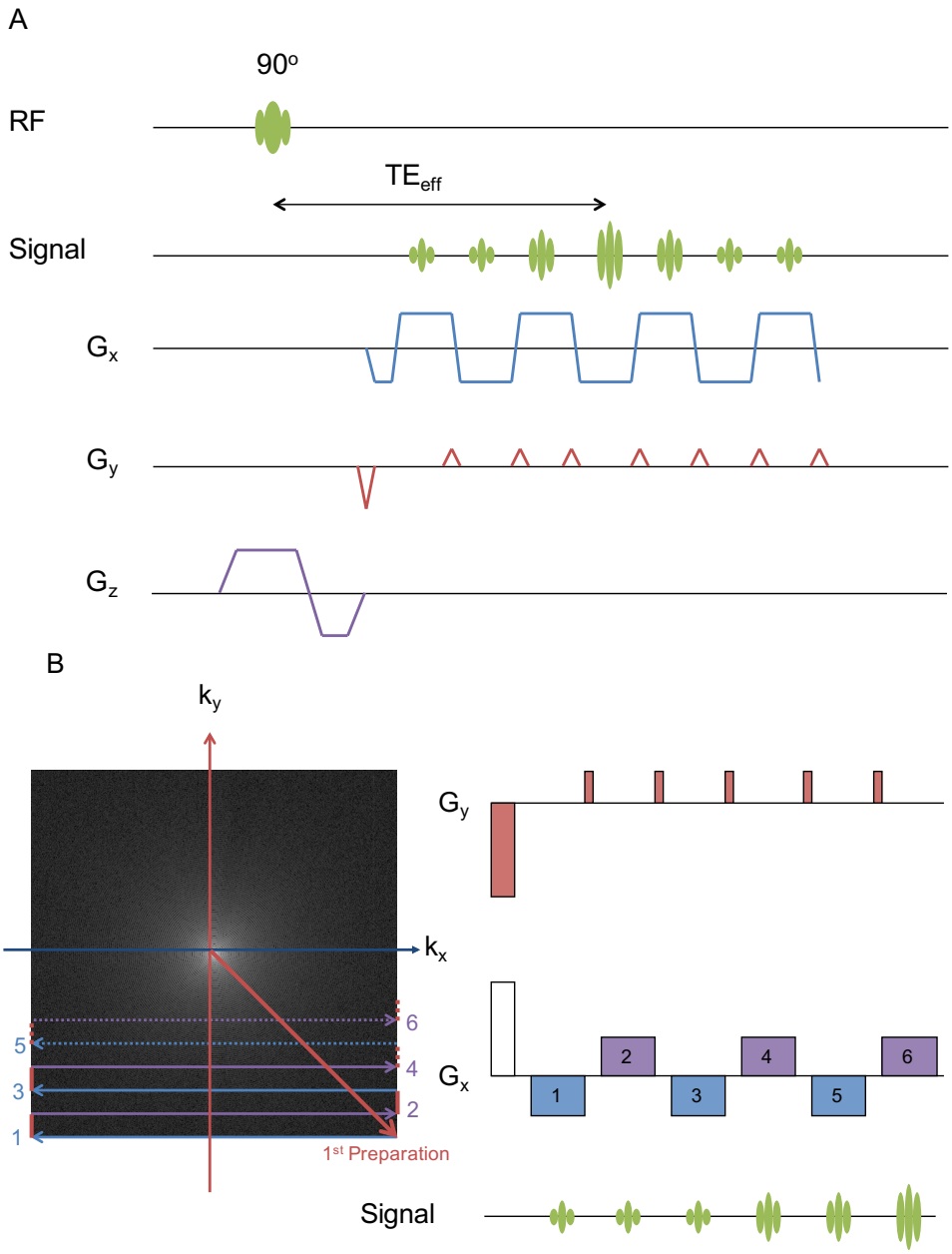

Figure 2-19. (A) Gradient-echo EPI sequence. Sampling is started at the edge of k-space with the aid of gradients in the x and y-direction. The blue and lines represent the frequency encoding gradients where signal is acquired while the red lines represent the phase encoding blips. The frequency-encoding gradient is then reversed, leading to the generation and acquisition of the first gradient-echo (1). A phase encoding gradient alters the k-space position and then the frequency-encoding gradient is again reversed, leading to another gradient-echo (2). This back and forth continues until all of k-space is filled.

Spectroscopic imaging requires not only spatial but also spectral information to be encoded. In 1984, Mansfield proposed a solution for rapid spectroscopic imaging, echo-planar spectroscopic imaging (EPSI) (46). Hardware limitations, however, meant that this method was first demonstrated in 1997, where changes in brain metabolites with hyperventilation were measured (47).

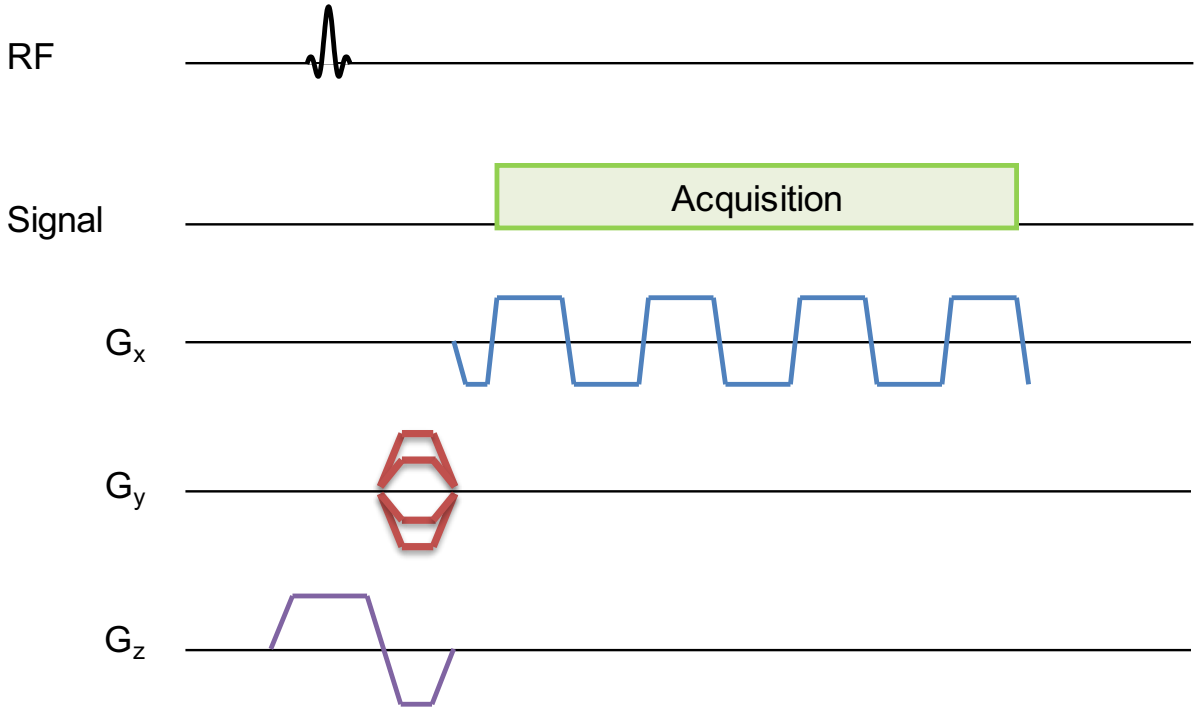

Figure 2-20. In echo-planar spectroscopic imaging (EPSI), the signal is acquired during an oscillating gradient waveform

The periodic inversion of the gradient lobe during the readout enables the encoding of spectroscopic signals as a single k-space line is repeatedly acquired as shown in Figure 2-20. This “zig-zag” provides spatial and spectral encoding. EPSI methods have been developed to allow regional assessment of cardiac metabolites and triglycerides in vivo (48).

2.6 Hyperpolarisation

Hyperpolarisation refers to the nuclear spin polarisation of a material far beyond thermal equilibrium conditions. Figure 2-21 is a simplified illustration of the results of hyperpolarisation on the magnetic moments of a sample. A number of techniques to increase the polarisation of a material exist. These include "brute force" methods (49), optical pumping of noble gases (50), para-hydrogen induced polarisation (51) and dynamic nuclear polarisation (DNP) (52). The enormous increases in signal provided by DNP offer great promise in the study of biological processes.

DNP can provide an increase in sensitivity of up to 10,000-100,000-fold. Potential advantages of hyperpolarisation include; decreased time required to observe a metabolite concentration change and increased signals from the target molecule against much lower background signal.

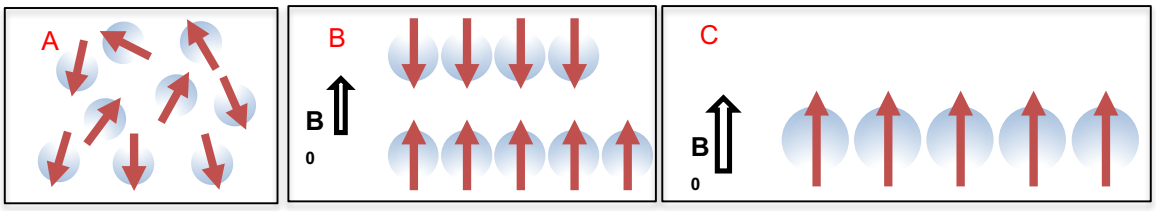

Figure 2-21. (A) illustrates the random nature of nuclear magnetic moments μ. (B) shows the alignment of the z-component of magnetic moments spin either with or against the external magnetic field (B_0) at thermal equilibrium. (C) illustrates the effect of hyperpolarisation, where the majority of magnetic moments to align with B_0.

2.7 Dynamic Nuclear Polarisation

DNP transfers the spin polarisation from electrons to nuclei (55-59). This transfer is carried out by first adding a small amount of a radical with unpaired electrons to a sample containing the molecule of interest. The sample is frozen to liquid helium temperatures (1 ± 0.3 K) and placed in a high magnetic field. At these temperatures, the electron spin polarisation approaches 100%. The sample is then irradiated with a continuous microwave frequency ω, a frequency that is close to the Larmor frequency of the electron spins ω_e. This radiation saturates the electron spin resonance (ESR) line of the unpaired electrons of stable radicals. Accordingly, the polarisation of the electrons can be transferred to the nuclei. Once an electron has transferred its polarisation, it returns to thermal equilibrium with a time T_{1e}, and can then polarise another nucleus. This process is known as the solid effect and requires high microwave power. Electron relaxation must occur faster than the T_{1N} of the nucleus for hyperpolarisation to proceed.

Other methods of hyperpolarisation include thermal mixing, which can take place with, or instead of the solid effect. Thermal mixing is a two-step effect, requiring less microwave energy than the solid effect. It involves two electrons and one nucleus. Firstly, the spin of one electron is flipped; this is followed by the flipping of two electrons of opposite sign, which then induces a flip in the nuclear spin. Thermal mixing requires a higher concentration of free electrons to allow coupling to occur between them and the nucleus of interest. Freezing the sample into a glassy state, using a solvent where required, allows enough contact between electrons and nuclei for coupling to occur.

2.8 Dissolution DNP

A dissolution DNP experiment is a three-step process; polarisation via DNP by microwave irradiation at low temperature, dissolution in a hot solvent and, finally, sample injection and data acquisition (53).

The molecule of interest (most commonly ^{13}C labelled pyruvate) is mixed with a source of free electrons provided by radicals. The mixture is cooled, placed in a magnetic field and pumped to low pressure to bring the temperature to approximately 1K (53). The magnetic field is used to polarise the electrons. With microwave radiation applied at a particular frequency, this high polarisation is transferred to the nuclei of interest. The process can take between 30 and 60 minutes depending on the T_1 of the sample in the solid state.

The sample must be rapidly warmed to allow its use in vivo. The hyperpolarised molecule sample is melted with a heated solution and shuttled out of the system using high-pressure helium gas. The solution can then injected into the subject of interest, and its downstream metabolites can be differentiated from each other on the basis of their chemical shifts.

Typical polarisation levels produced with [1-^{13}C] pyruvate range from 20-40%. This polarisation decays with the T_1 of the molecule. The T_1 value varies with the molecule studied but is typically 1-2 minutes for molecules of small weight. The short T_1 value means that the solution must be used quickly after being generated.

Hyperpolarised ^{13}C MR studies have mainly used the molecules [1-^{13}C] pyruvate, [2-^{13}C] pyruvate, and ^{13}C-bicarbonate as they polarise efficiently, retain hyperpolarisation for a relatively long time, and are rapidly metabolised via critical enzymes in the heart. It has been found that ^{13}C labelled carbonyl positions are of particular interest as the T_1 is about 30-50 seconds. T_1 times of molecules of interest in biomedical imaging are shown in **Table 2-2**.

Pyruvate is a key substrate for many metabolic pathways. Its role as an intermediary can be clearly seen in the simplified Figure 2-22. In the myocardial cells, pyruvate can be metabolised to lactate, alanine, and CO_2. Following combination with water to form carbonic acid, the CO_2 rapidly forms HCO_3^- with the aid of carbonic anhydrase.

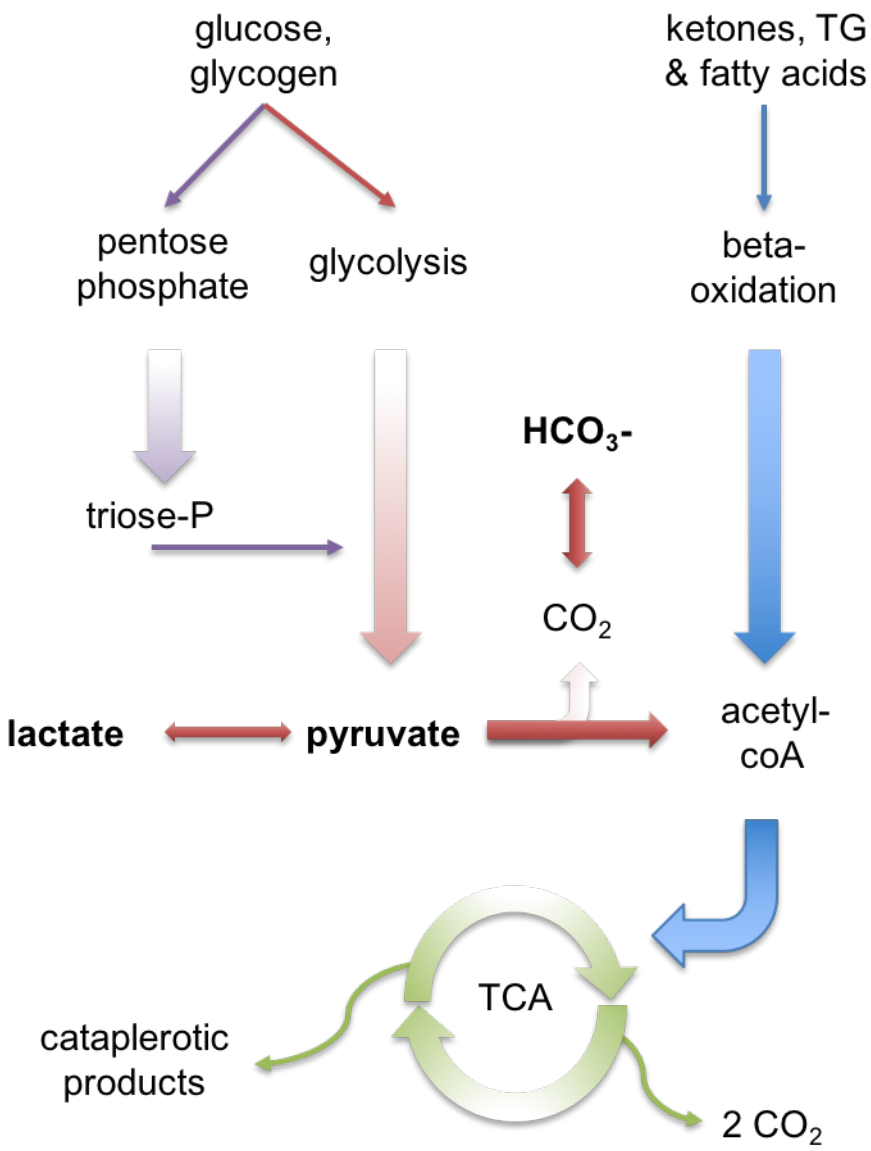

Figure 2-22. Simplified diagram indicating the role of pyruvate as the end product of glycolysis, showing its key position between glycolysis and the tricyclic acid (TCA) cycle. Some of the products measured by hyperpolarised ^{13}C DNP imaging, including lactate and bicarbonate (HCO_3^-) can also be seen.

DNP allows the detection of metabolites present at very low concentrations, undetectable by conventional NMR. Additionally it enables the observation of fast metabolic processes in real-time and in-vivo after infusion of hyperpolarised ^{13}C labelled biomolecules (54).

Unlike in conventional MR, where relaxation increases the longitudinal magnetisation, T_1 relaxation in hyperpolarised experiments involves decay of magnetisation to normal Boltzmann polarisation levels. This fact means that conventional spin echo sequences are of little use, as hyperpolarisation does not relax back to its initial magnetisation following a single 90° RF pulse, rather it remains at zero. For this reason, multiple low flip angle acquisitions are typically performed during an experiment following the DNP sample dissolution and subsequent infusion.

Metabolite	T_1[s]
[1-^{13}C]sodium acetate	49 (11.7T); 50 (3T); 34 (3T)
[1-^{13}C]alanine	42 (3T); 29 (9.4T)
[1-^{13}C]bicarbonate	49 (11.7T); 34 (3T)
[1-^{13}C]pyruvic acid	67 (3T); 48 (11.7T); 44 (14.1T)
[1,5-^{13}C]citric acid	25
[1-^{13}C]lactate	45, 50.6 (3T); 32, 33.4 (14.1T)
[1,1'-$^{13}C_2$]butyric anhydride	39,40 (14.1 T)
[1,4-^{13}C]fumaric acid	24 (9.4T); 29 (11.7T)
^{13}C -urea	44 (11.7T); 35 (14.1T)

Table 2-2. Longitudinal relaxation times T_1 of ^{13}C labelled metabolites of interest for in vivo DNP studies. Adapted, with permission, from (26).

2.9 Dynamic ^{13}C NMR Spectroscopy

Rapid acquisitions are needed to measure the metabolic information before the hyperpolarisation has decayed. A variety of methods has been used to date. Some of the earliest images generated used MRSI to image the metabolic changes following myocardial ischemia in a pig model (55). However, the limitations of this method include poor resolution, a lack of dynamic acquisition, and the length of acquisition time. Alternatives to overcome some of these issues include EPSI (56) (1.5.3.1) and fast spiral MRSI (57).

Besides MRSI and EPSI, the process of spectral encoding can also be addressed using spatial-spectral (SPSP) excitation in conjunction with EPI readouts (58). The sparse spectra (i.e., pyruvate, lactate, alanine, and bicarbonate) following the injection of hyperpolarised ^{13}C-pyruvate are well suited to the SPSP technique (59, 60). SPSP pulses are applied in the frequency and slice-selective direction simultaneously. Changing the excitation frequency will result in different metabolites being encoded in an interleaved scheme. Each metabolite of interest can be excited with a particular flip angle. Selective excitation is of particular importance in hyperpolarised imaging. For example, following hyperpolarised pyruvate injection, the initial concentration of pyruvate will be much higher than that of its downstream metabolites – such as lactate or bicarbonate. A lower flip angle can be used for pyruvate, avoiding saturation while conserving polarisation. A higher flip angle is used for its downstream metabolites that are found in lower concentrations (60). Disadvantages of this approach include the long SPSP pulse required, and the inability for correction after the use of an incorrect excitation frequency. Minimum slice

thickness is limited by the minimum time between SPSP subpulses. However, modifications of this technique have been able to provide slice thickness of 8 mm (61) and 5 mm (Chapter 6).

2.10 References:

(1) Zeeman, P. (1897). XXXII. On the influence of magnetism on the nature of the light emitted by a substance. *Philosophical Magazine Series 5* **43**(262), 226-239.

(2) Pauli, W., Jr. (1924). Zur Frage der theoretischen Deutung der Satelliten einiger Spektrallinien und ihrer Beeinflussung durch magnetische Felder. *Naturwissenschaften* **12**(37), 741-743.

(3) Bloch, F., Hansen, W.W., and Packard, M. (1946). Nuclear Induction. *Phys. Rev.* **69**(3-4), 127-127.

(4) Purcell, E.M., Pound, R.V., and Bloembergen, N. (1946). Nuclear Magnetic Resonance Absorption in Hydrogen Gas. *Phys. Rev.* **70**(11-12), 986-987.

(5) Knight, W.D. (1949). Nuclear Magnetic Resonance Shift in Metals. *Phys. Rev.* **76**(8), 1259-1260.

(6) Meyer, L.H., Saika, A., and Gutowsky, H.S. (1953). Electron Distribution in Molecules. III. The Proton Magnetic Spectra of Simple Organic Groups1. *J. Am. Chem. Soc.* **75**(18), 4567-4573.

(7) Proctor, W.G., and Yu, F.C. (1951). On the Nuclear Magnetic Moments of Several Stable Isotopes. *Phys. Rev.* **81**(1), 20-30.

(8) Proctor, W.G., and Yu, F.C. (1950). The Dependence of a Nuclear Magnetic Resonance Frequency upon Chemical Compound. *Phys. Rev.* **77**(5), 717-717.

(9) Dickinson, W.C. (1950). Dependence of the F19 Nuclear Resonance Position on Chemical Compound. *Phys. Rev.* **77**(5), 736-737.

(10) Shaw, T.M., and Elsken, R.H. (1950). Nuclear Magnetic Resonance Absorption in Hygroscopic Materials. *J. of Chem. Phys.***18**(8), 1113-1114.

(11) Moon, R.B., and Richards, J.H. (1973). Determination of intracellular pH by 31P magnetic resonance. *J. Biol. Chem.* **248**(20), 7276-8.

(12) Hoult, D.I., Busby, S.J., Gadian, D.G., Radda, G.K., Richards, R.E., and Seeley, P.J. (1974). Observation of tissue metabolites using 31P nuclear magnetic resonance. *Nature* **252**(5481), 285-7.

(13) Digby, A. (2001). Wellcome witnesses to twentieth century medicine, vol. 2. Making the human body transparent: the impact of nuclear magnetic resonance and magnetic

resonance imaging. Research in general practice. Drugs in psychiatric practice. The MRC Common Cold Unit. *Med. Hist.* **45**(1), 137-138.

(14) Matwiyoff, N.A., and Needham, T.E. (1972). Carbon-13 NMR spectroscopy of red blood cell suspensions. *Biochem. Biophys. Res. Commun.* **49**(5), 1158-64.

(15) Odeblad, E., and Lindstrom, G. (1955). Some preliminary observations on the proton magnetic resonance in biologic samples. *Acta Radiol Suppl (Stockholm)* **43**, 469-76.

(16) Odeblad, E. (1968). An NMR-Method for Determination of Ovulation. *Acta Obstet. Gynecol. Scand.* **47**(S8), 39-47.

(17) Damadian, R., Zaner, K., Hor, D., and DiMaio, T. (1974). Human tumors detected by nuclear magnetic resonance. *Proc. Natl. Acad. Sci. U. S. A.* **71**(4), 1471-3.

(18) Lauterbur, P.C. (1973). Image Formation by Induced Local Interactions: Examples Employing Nuclear Magnetic Resonance. *Nature* **242**(5394), 190-191.

(19) Mansfield, P., and Grannell, P.K. (1973). NMR 'diffraction' in solids? *J. Phys. C: Solid State* **6**(22), L422.

(20) Kumar, A., Welti, D., and Ernst, R.R. (1975). NMR Fourier zeugmatography. *J. Magn Reson. (1969)* **18**(1), 69-83.

(21) Reiser, M. (2008). *Magnetic resonance tomography* (Heidelberg: Springer).

(22) Balc, M. (2005). *Basic p1 sH- and p13 sC-NMR spectroscopy* (Amsterdam: Elsevier).

(23) Graaf, R.A.d. (2007). *In vivo NMR spectroscopy principles and techniques*, 2nd edn (Chichester: Wiley).

(24) Harris, R. (1986). *Nuclear magnetic resonance spectroscopy* [Online]. Harlow: Longman Scientific Technical.

(25) Mitchell, H.H., Hamilton, T.S., Steggerda, F.R., and Bean, H.W. (1945). The Chemical Composition of the Adult Human Body and its bearing on the Biochemistry of Growth. *J. Biol. Chem.* **158**(3), 625-637.

(26) Keshari, K.R., and Wilson, D.M. (2014). Chemistry and biochemistry of 13C hyperpolarized magnetic resonance using dynamic nuclear polarization. *Chem. Soc. Rev.* **43**(5), 1627-59.

(27) Bloch, F., Hansen, W.W., and Packard, M. (1946). The Nuclear Induction Experiment. *Phys. Rev.* **70**(7-8), 474-485.

(28) Bloch, F. (1946). Nuclear Induction. *Phys. Rev.* **70**(7-8), 460-474.

(29) Bazelaire, C.M.J.d., Duhamel, G.D., Rofsky, N.M., and Alsop, D.C. (2004). MR Imaging Relaxation Times of Abdominal and Pelvic Tissues Measured in Vivo at 3.0 T: Preliminary Results. *Radiology* **230**(3), 652-659.

(30) Huggert, A., and Odeblad, E. (1959). Proton magnetic resonance studies of some tissues and fluids of the eye. *Acta Radiol.* **51**(5), 385-92.

(31) Moon, J.C., Messroghli, D.R., Kellman, P., Piechnik, S.K., Robson, M.D., Ugander, M., Gatehouse, P.D., Arai, A.E., Friedrich, M.G., Neubauer, S.*, et al.* (2013). Myocardial T1 mapping and extracellular volume quantification: a Society for Cardiovascular Magnetic Resonance (SCMR) and CMR Working Group of the European Society of Cardiology consensus statement. *J. Cardiovasc. Magn. Reson.* **15**, 92.

(32) Hahn, E.L. (1950). Spin Echoes. *Phys. Rev.* **80**(4), 580-594.

(33) Look, D.C., and Locker, D.R. (1970). Time Saving in Measurement of NMR and EPR Relaxation Times. *Rev. Sci. Instrum.* **41**(2), 250-251.

(34) Henderson, E., McKinnon, G., Lee, T.Y., and Rutt, B.K. (1999). A fast 3D look-locker method for volumetric T1 mapping. *Magn. Reson. Imaging* **17**(8), 1163-71.

(35) Messroghli, D.R., Radjenovic, A., Kozerke, S., Higgins, D.M., Sivananthan, M.U., and Ridgway, J.P. (2004). Modified Look-Locker inversion recovery (MOLLI) for high-resolution T1 mapping of the heart. *Magn. Reson. Med.* **52**(1), 141-6.

(36) Messroghli, D.R., Walters, K., Plein, S., Sparrow, P., Friedrich, M.G., Ridgway, J.P., and Sivananthan, M.U. (2007). Myocardial T1 mapping: application to patients with acute and chronic myocardial infarction. *Magn. Reson. Med.* **58**(1), 34-40.

(37) Messroghli, D.R., Niendorf, T., Schulz-Menger, J., Dietz, R., and Friedrich, M.G. (2003). T1 mapping in patients with acute myocardial infarction. *J. Cardiovasc. Magn. Reson.* **5**(2), 353-9.

(38) Messroghli, D.R., Plein, S., Higgins, D.M., Walters, K., Jones, T.R., Ridgway, J.P., and Sivananthan, M.U. (2006). Human myocardium: single-breath-hold MR T1 mapping with high spatial resolution--reproducibility study. *Radiology* **238**(3), 1004-12.

(39) Messroghli, D.R., Nordmeyer, S., Buehrer, M., Kozerke, S., Dietrich, T., Kaschina, E., Becher, P.M., Hucko, T., Berger, F., Klein, C.*, et al.* (2011). Small animal Look-Locker inversion recovery (SALLI) for simultaneous generation of cardiac T1 maps and cine and

inversion recovery-prepared images at high heart rates: initial experience. *Radiology* **261**(1), 258-65.

(40) Frahm, J., Merboldt, K.-D., and Hänicke, W. (1987). Localized proton spectroscopy using stimulated echoes. *Journal of Magnetic Resonance (1969)* **72**(3), 502-508.

(41) Bottomley, P.A. (1987). Spatial localization in NMR spectroscopy in vivo. *Ann. N. Y. Acad. Sci.* **508**, 333-48.

(42) Keevil, S.F. (2006). Spatial localization in nuclear magnetic resonance spectroscopy. *Phys. Med. Biol.* **51**(16), R579-636.

(43) Brown, T.R., Kincaid, B.M., and Ugurbil, K. (1982). NMR chemical shift imaging in three dimensions. *Proc. Natl. Acad. Sci. U. S. A.* **79**(11), 3523-6.

(44) Mansfield, P. (1977). Multi-planar image formation using NMR spin echoes. *J. Phys. C: Solid State* **10**(3), L55.

(45) Rzedzian, R., Chapman, B., Mansfield, P., Coupland, R.E., Doyle, M., Chrispin, A., Guilfoyle, D., and Small, P. (1983). Real-time nuclear magnetic resonance clinical imaging in paediatrics. *Lancet* **2**(8362), 1281-2.

(46) Mansfield, P. (1984). Spatial mapping of the chemical shift in NMR. *Magn. Reson. Med.* **1**(3), 370-86.

(47) Posse, S., Dager, S.R., Richards, T.L., Yuan, C., Ogg, R., Artru, A.A., Muller-Gartner, H.W., and Hayes, C. (1997). In vivo measurement of regional brain metabolic response to hyperventilation using magnetic resonance: proton echo planar spectroscopic imaging (PEPSI). *Magn. Reson. Med.* **37**(6), 858-65.

(48) Weiss, K., Martini, N., Boesiger, P., and Kozerke, S. (2012). Metabolic MR imaging of regional triglyceride and creatine content in the human heart. *Magn. Reson. Med.* **68**(6), 1696-704.

(49) Johnson, R., Paulson, D., Giffard, R., and Wheatley, J. (1973). Bulk nuclear polarization of solid3He. *J. Low Temp. Phys.* **10**(1-2), 35-58.

(50) Happer, W. (1972). Optical Pumping. *Rev. Mod. Phys.* **44**(2), 169-249.

(51) Bowers, C.R., and Weitekamp, D.P. (1987). Parahydrogen and synthesis allow dramatically enhanced nuclear alignment. *J. Am. Chem. Soc.* **109**(18), 5541-5542.

(52) Abragam, A., and Goldman, M. (1978). Principles of dynamic nuclear polarisation. *Rep. Prog. Phys* **41**(3), 395.

(53) Ardenkjaer-Larsen, J.H., Fridlund, B., Gram, A., Hansson, G., Hansson, L., Lerche, M.H., Servin, R., Thaning, M., and Golman, K. (2003). Increase in signal-to-noise ratio of > 10,000 times in liquid-state NMR. *Proc. Natl. Acad. Sci. U. S. A.* **100**(18), 10158-63.

(54) Golman, K., in 't Zandt, R., and Thaning, M. (2006). Real-time metabolic imaging. *Proc. Natl. Acad. Sci. U. S. A.* **103**(30), 11270-5.

(55) Golman, K., Petersson, J.S., Magnusson, P., Johansson, E., Akeson, P., Chai, C.M., Hansson, G., and Mansson, S. (2008). Cardiac metabolism measured noninvasively by hyperpolarized 13C MRI. *Magn. Reson. Med.* **59**(5), 1005-13.

(56) Yen, Y.F., Kohler, S.J., Chen, A.P., Tropp, J., Bok, R., Wolber, J., Albers, M.J., Gram, K.A., Zierhut, M.L., Park, I.*, et al.* (2009). Imaging considerations for in vivo 13C metabolic mapping using hyperpolarized 13C-pyruvate. *Magn. Reson. Med.* **62**(1), 1-10.

(57) Mayer, D., Levin, Y.S., Hurd, R.E., Glover, G.H., and Spielman, D.M. (2006). Fast metabolic imaging of systems with sparse spectra: application for hyperpolarized 13C imaging. *Magn. Reson. Med.* **56**(4), 932-7.

(58) Meyer, C.H., Pauly, J.M., Macovski, A., and Nishimura, D.G. (1990). Simultaneous spatial and spectral selective excitation. *Magn. Reson. Med.* **15**(2), 287-304.

(59) Cunningham, C.H., Chen, A.P., Lustig, M., Hargreaves, B.A., Lupo, J., Xu, D., Kurhanewicz, J., Hurd, R.E., Pauly, J.M., Nelson, S.J.*, et al.* (2008). Pulse sequence for dynamic volumetric imaging of hyperpolarized metabolic products. *J. Magn. Reson.* **193**(1), 139-46.

(60) Lau, A.Z., Chen, A.P., Hurd, R.E., and Cunningham, C.H. (2011). Spectral-spatial excitation for rapid imaging of DNP compounds. *NMR Biomed.* **24**(8), 988-96.

(61) Weiss, K., Sigfridsson, A., Wissmann, L., Busch, J., Batel, M., Krajewski, M., Ernst, M., and Kozerke, S. (2013). Accelerating hyperpolarized metabolic imaging of the heart by exploiting spatiotemporal correlations. *NMR Biomed.* **26**(11), 1380-6.

Chapter 3 - T_1 Mapping in Ischemic Heart Disease

3.1 Abstract

Disease processes can change the quantity and form of water in tissues. Research into T_1 mapping has primarily been focused on the study of cardiomyopathies, but T_1 mapping also shows potential in the study of ischaemic heart disease. In fact, the first cardiac T_1 maps were used to characterise myocardial infarction in the 1980s. Robust high-resolution myocardial T_1 mapping is now available for use as a clinical tool. This quantitative technique is simple to perform and analyse, minimally subjective, and highly reproducible. This chapter aims to summarise the present state of research on the topic and to show the clinical potential of this method to aid the diagnosis and treatment of patients with ischaemic heart disease (1).

3.2 Introduction

Magnetic resonance imaging (MRI) is the gold standard imaging technique for cardiac anatomy and function. A unique feature of MRI is its ability to characterise tissue using proton relaxation times, T_1, T_2, and T_2^*. These values are mostly dependent on the physical and chemical environments of water protons in tissue. Using conventional MRI techniques, higher signal intensity with either T_1 weighted sequences using gadolinium contrast agents or T_2 weighted techniques can detect myocardial infarction (MI) or focal oedema respectively. Unlike other imaging modalities, such as CT, signal intensity in CMR images is displayed on an arbitrary scale. This property means that signals cannot be quantified or compared between subjects or follow-up examinations in the same individual. Visualization of pathology depends on a contrast existing between “normal” and “abnormal” myocardium. T_1 weighted sequences provide the basis for late gadolinium enhancement (LGE) imaging that is now universally used in the detection of MI, the focal lesions of myocarditis and myocardial fibrosis in cardiomyopathies.

T_1 values are a reflection of the composition of individual tissues, with each tissue type having a normal range. T_1 values can alter in the presence of disease, and this difference can be used to study and diagnose tissue pathology (2). In fact, some of the earliest work on MRI was driven by a belief that cancerous tissues could be distinguished from healthy tissues on the basis of their relaxations times (3). T_1 reflects the mobility of nuclei (predominantly protons) and how they are bound within macromolecules. Therefore, it can be used to study macromolecular content, water binding and water content. For example, muscle has an intermediate value but with inflammation, water content increases and is matched by an increase in T_1.

When T_1 is measured on a pixel-by-pixel basis, the resulting T_1 values can be visualized as a T_1 map. In this map, the signal intensity of each pixel reflects the absolute T_1 value of the underlying voxel. The interest in absolute quantification of T_1 values in a clinical setting has risen recently. Over the last few years, a number of sequences have been developed which allow robust high-resolution cardiac T_1 mapping (4, 5).

3.3 Historical Background

T_1 quantification has been the basis for diagnostic methods since the beginning of magnetic resonance imaging in the early 1970s. The initial studies looking at changes in T_1 in the heart were performed in vitro using samples from dog hearts (6). These showed that T_1 increased with ischemia and that the magnitude of increase was related to the duration and severity of ischemia. In-vivo studies then demonstrated increases in T_1 and T_2 with infarction. The first studies to quantify myocardial T_1 in humans with recent myocardial infarction (MI) also detected increased T_1. These were also the first to present their findings as a map of the T_1 values of the heart (7). T_1 was found to increase within the first hour of ischemia (8), reach its peak in patients with ST-elevation myocardial infarction (STEMI) between days 8-14, before gradually returning to baseline (9).

Following these early studies, specific techniques were developed to exploit these changes in tissue oedema. The short-inversion-time inversion recovery (STIR) magnetic resonance imaging pulse sequence, which generates high contrast from both T_1 and T_2 prolongation in the presence of water, is widely used for the detection of myocardial oedema in myocarditis (10), rejection in cardiac transplant (11), and acute MI (12).

Ex-vivo measurements of T_1 are usually based on inversion recovery sequences, requiring an interval of at least five times the T_1 to allow for adequate recovery. This technique could be used for the first investigations into myocardial relaxation at very low field strengths (0.08T). At these very low field strengths, T_1 is short (305 ms), and acquisition schemes can easily be fitted into the cardiac cycle (7, 9). As field strength increased to 1.5T, myocardial T_1 increased to approximately 1000 ms, which exceeds cardiac cycle length in most patients. As a consequence, conventional acquisition schemes could not be confined to single cardiac cycles and required long acquisition times. The long acquisition times prevented their use as breath-hold techniques in clinical routine. Cardiac motion meant that alternative methods, such as the Look-Locker described above, were unsuitable for imaging the heart.

T_1 quantification in ischemic heart disease can be divided into native and post-contrast applications. Native T_1 values in this setting are a reflection of the composite water signal from interstitium and myocytes, and, therefore, reflect changes in water content. As standard

gadolinium contrast agents are extravascular and extracellular, changes in T_1 following contrast administration reflect gadolinium concentration in the extravascular compartment. These changes can then be used to estimate extracellular volume (ECV).

3.4 Native Myocardial applications

3.4.1 Myocardial Oedema

To understand the changes occurring in myocardial relaxation values, we need to understand the response of the heart to injury. Myocardial injury is characterised by cellular oedema (13). In healthy myocardium, water balance is tightly regulated by cell membrane function, Starling filtration and lymphatic drainage. Intracellular water accounts for 79% of total water or about 380ml/100g of dry tissue and varies little between individuals or species (14). As myocardial water balance is an energy requiring process, myocardial ischemia will result in failure of the active processes of cell volume regulation. The earliest studies looking at T_1 values in myocardial ischemia came from the knowledge that ischemia results in oedema (15). In fact, the increasing amounts of water present after reflow have been shown to correlate with increased myocardial injury in an animal model (16).

Myocardial oedema occurs within 15 minutes of coronary occlusion (17). Myocardial water reaches its peak in the first 1-2 hours after onset of ischemia (18) and is caused by dysfunction of the complex processes that regulate both intra- and intercellular myocardial water balance. Initially, there is a local intracellular increase in the products of anaerobic metabolism, such as lactate and inorganic phosphates (19). The increased osmotic load draws water into the intracellular space (17).This initial increase in water is limited by the reduction in blood supply and the limited amount of extracellular water.

The alterations in cell membrane function can be simplified into three stages (20). Initially there is inhibition of the Na^+/K^+ pump, resulting in an influx of water as it follows the increased intracellular Na^+. The second stage involves the sarcolemmal transport systems, again leading to an increase in intracellular water. Finally, physical disruption of the cell membrane occurs, and breakdown of the water and ion equilibrium between the interior and exterior of the cell.

Reperfusion can worsen myocardial oedema, but the degree of oedema is predominantly determined by the duration and severity of the preceding ischemic episode (21). The increased oedema is caused by a reactive hyperaemia and osmotic changes. Following the opening of an occluded coronary artery, blood flow to ischemic myocardium significantly increases. There is a localised increase in cellular osmolality as high energy phosphates, and macromolecules are broken down (22). These products diffuse into extracellular spaces but, intracellular osmolality remains increased (22). On reperfusion, the hyperosmolar myocardial cells absorb extra fluid across this osmotic gradient to return the osmolarity of the intracellular environment to normal.

The time before cell death will vary on the degree of ischemia, whether there is absolute cessation or merely reduced blood flow, the presence of collateral blood supply, and the duration of ischemia. From the processes described above, it can be seen that prolonged ischemia will result in a breakdown of the active processes maintaining cellular homeostasis, with the final stage being the breakdown of myocardial cell walls. Brief episodes of ischemia are tolerated by the myocardial cells. In general, coronary occlusions of up to 15 minutes is thought to be associated with reversible injury, with occlusion of longer duration resulting in myocardial infarction.

3.4.2 T_1 Changes in Myocardial Infarction

Changes in T_1 can be used to detect acute MI with high sensitivity and specificity (23-25). As of yet there is no cut-off T_1 value to distinguish infarcted myocardium from the surrounding oedematous myocardium; however previous studies have demonstrated high accuracy using three (23) and two (24) standard deviations above mean values. Whereas most studies have focused on patients with ST-elevation myocardial infarction (STEMI), T_1 mapping can also identify infarction in patients with non-STEMI (24). There is a progression in T_1 from healthy myocardium to that of maximal injury, a finding similar to the peri-infarct zone described in studies studying MI with contrast agents (26), or the wavefront phenomenon In acute MI (27). T_1 increases are more pronounced in the myocardium that will become infarcted than in myocardium that will be salvaged by reperfusion (28). Following reperfusion, T_1 increases further in infarcted tissue but remains unchanged in salvaged myocardium.

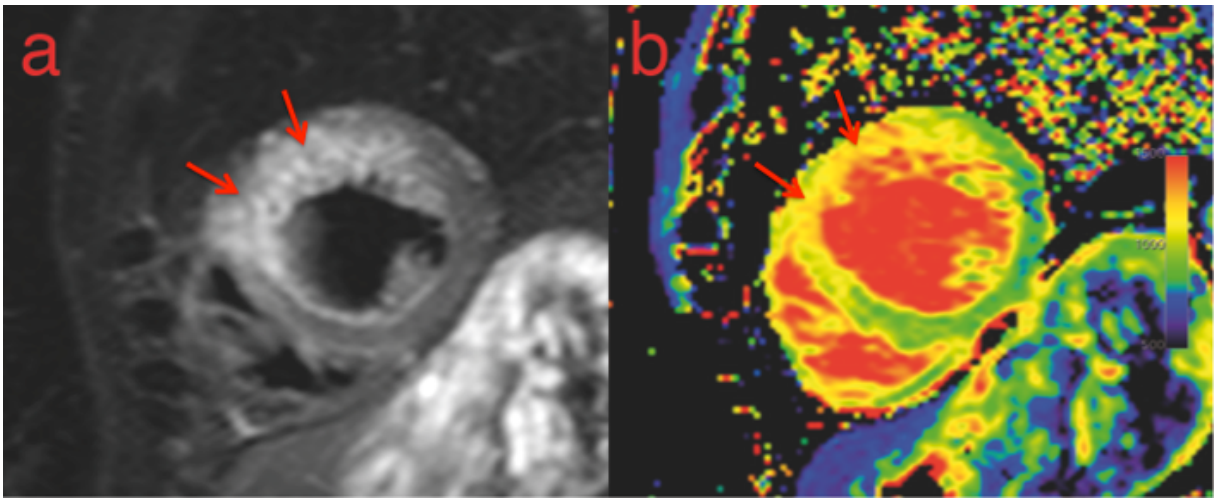

Figure 3-1. (a) Short axis STIR image in 52-year-old male six days post anterior STEMI with localised hyperintensity indicating acute oedema (arrows). (b) Corresponding T_1 map demonstrates a similar area of injury; however there is a zone with a range of increased T_1 (arrows) reflecting the increasing severity of injury from epicardium to endocardium.

In chronic MI, T_1 values are higher than normal myocardium, but do not reach the levels of acute MI (23). There is replacement of myocardial cells by scarring or fibrosis with an increase in extracellular collagen. Importantly, there is no oedema, as this has resolved in the initial weeks after MI. These subtle differences in T_1 in chronic infarction do not allow reliable discrimination of acute from chronic myocardial without the use of gadolinium contrast (23). In some areas of chronic MI areas of lipomatous metaplasia can be seen, particularly when T_1 weighted sequences are used (29). As fat has a T_1 value much lower than myocardium (230-350 ms), intramyocardial fat can be easily identified byT_1 mapping (30).

Elevated myocardial water content also results in increased T_2. T_2 weighted imaging has been used for oedema imaging since the first papers demonstrating T_2 prolongation in MI in dogs (31) and humans (32). T_2 based imaging techniques have been used in acute MI, (12) myocarditis, (10) sarcoidosis, (33) and in cardiac transplant rejection (34). A difficulty with this technique is the need for a homogenous magnetic field, as the increase in T_2 associated with oedema in acute MI is relatively small - in the order of 15-20 ms (8). The STIR sequence, a technique that uses changes in both T_1 and T_2 to obtain contrast, is commonly used to identify areas of hyperintense signal (35). However, a number of technical issues may affect the signal intensity, including choice of coil used, artefacts from slow flowing blood, slice thickness, signal loss from myocardial contraction, relaxation during acquisition and TR (36). As absolute values are not quantified, contrast depends on the presence of “normal” myocardium. Therefore, diseases that involve diffuse or widespread inflammation of the myocardium cannot be identified. By providing an

absolute value for myocardium, T_2 mapping may overcome some of these limitations (37). Indeed, more recently T_2 mapping has been used to study the development of myocardial oedema in a pig model of myocardial ischemia, where not only were the T_2 values in the ischemic myocardium higher than that of the remote myocardial, but the T_2 values were found to parallel the measured myocardial water content (38). However, in chronic myocardial infarction, where there is no oedema, T_2-weighted imaging is less able to differentiate healthy from infarcted myocardium (12).

Pre-contrast T_1 measurement may have some other novel uses. For example, methemoglobin, formed from thrombus, has a T_1 shortening effect (39). This property can be used to detect intramyocardial haemorrhage in MI, (40) a marker of adverse cardiac outcomes. Shorter myocardial T_1 following acute myocardial infarction, probably reflecting haemorrhage, can also detect the severity of myocardial injury and predict long-term recovery of contractile function (24).

3.4.3 Duration of T_1 Changes

After the restoration of normal myocardial blood flow following a brief period of ischemia, the ECG can normalize within seconds, and functional changes normalize within 5 minutes. However increased intracellular water is present for a much greater period. Pathological studies demonstrate a gradual resolution of intracellular oedema, typically over one month (41). These findings were matched in an early study that showed that water content was elevated with a corresponding prolongation of T_1 in dogs three weeks following MI (8). A T_1 mapping study demonstrated increased T_1 for up to 2 months after MI (25). Persistent small areas of hyperintensity have been detected with the STIR technique at up to 6 months after infarction (42). Potential reasons for persistent oedema could include increased wall stress, residual/recurring ischemia, alterations in drainage of the infarcted segments or continuing tissue repair.

3.5 Post-contrast Applications

3.5.1 T_1 Mapping in Acute Myocardial Infarction

The increased volume of distribution for gadolinium agents in infarction shortens the T_1 of infarcted areas to a greater extent than that of normal myocardium. The larger the volume of distribution, the larger the concentration of gadolinium. The difference in T_1 can be used to

distinguish between normal and infarcted tissue. This property, used in a non-quantitative manner in LGE imaging, is the in-vivo gold standard method of detecting MI. In acute infarction, the timing of the LGE sequence is critical. The injured tissue surrounding the acutely infarcted myocardium is swollen, and, therefore, there is increased extracellular space where gadolinium can accumulate. If LGE is performed early following contrast injection the hyperenhanced area will include both the infarcted tissue and at least some of the surrounding injured myocardium. Infarcted myocardium will only be brighter than the surrounding injured tissue late after contrast injection when the gadolinium is cleared from the viable myocardium. The best available data suggests an interval of at least 10 minutes is required to allow accurate infarct assessment (43) however, some groups wait up to 20 minutes (44). As the volume of distribution in infarcted tissue is much higher in infarcted than in injured myocardium, the combination of both pre- and post-contrast T_1 mapping may better differentiate between reversible and irreversible injury. In addition, in acutely injured myocardium, the higher initial concentration of free water and therefore elevated native T_1 will reduce the net change in T_1 and thus reduce the effective T_1-shortening and apparent contrast enhancement (45).

3.5.2 Chronic Myocardial Infarction

As T_1 values of chronically infarcted myocardium are lower than acutely infarcted myocardium, the difference in post-contrast T_1 between normal and infarcted myocardium is greater in chronic MI. A problem with LGE imaging, irrelevant to the timing of infarct, is that it is dependent on the manual setting of the inversion time to null normal myocardium. infarct size may be underestimated of should the incorrect inversion time be chosen.

3.5.3 Microvascular Obstruction

Precontrast T_1 values of areas of microvascular obstruction (MVO) have been found to be higher than that of remote myocardium, but lower than the surrounding hyperenhanced area (24). This may be due to reduced blood supply in this area, which limits oedema. Whereas MI detection using LGE reflects decreased wash-out of contrast, areas of MVO can be detected by decreased wash-in. The timing of the LGE imaging plays a significant role in the detection of MVO. Gadolinium contrast agents will diffuse passively over time, leading to eventual hyperenhancement. Gadolinium will, therefore, have less T_1 shortening action in areas of MVO if T_1 times are measured early after contrast administration.

3.6 Area at Risk

The area at risk (AAR) refers to the hypoperfused myocardium during coronary occlusion (46). In revascularized myocardium, the relation between the AAR and the infarct allows the quantification of the volume of myocardium that reperfusion successfully salvaged from ischemic death. The AAR can therefore not only be used as a measure of the severity of ischemic insult, but it could also be used to measure the efficacy of a treatment.

The AAR must be clearly identified to allow the study of the effects of treatments on infarct size. Previously, radionuclide imaging was used. This method has many limitations including use of nuclear tracers in an emergency department, high cost, low image resolution, and radiation. The unique tissue characterisation abilities of MRI make it a suitable method for identifying the area at risk. AAR using T_2 weighted imaging has been validated against pathology (47) and AAR as delineated using single-photon emission computed tomography **(**SPECT) imaging (48).

The basis of the identification of the AAR is similar for both T_1 mapping and T_2 weighted imaging, i.e. protons from increased water in oedematous myocardium caused by ischemia are detectable by increases in T_1 and T_2. It has been known for many years that ex-vivo T_1 weighted imaging was able to delineate the AAR (49). These findings were recently confirmed in-vivo in a study demonstrating increased T_1 in the AAR. In addition, this area closely matched the AAR as defined by microspheres (50). In keeping with the concept of oedema being a marker of severity of injury, T_1 changes can predict myocardial salvage and myocardial recovery (24). It has been found that T_1 is higher in myocardium that ultimately goes on to undergo infarction than in salvaged myocardium (28). Mapping techniques, using either T_1 or T_2, have the potential to improve the objectivity of the AAR imaging. However, a recent study examining the changes in myocardial water content and T_2 values found that the myocardial response to injury followed a bimodal pattern, with an early wave dissipating in the first 24 hours, to be followed by a second wave peaking at day 7 (38). This study has brought into question some of the studies using T_2 weighted imaging as a marker of myocardial salvage, as the myocardial salvage index would vary simply with the index time since the ischemic episode.

3.7 Extracellular Volume

The myocardium is made up of both myocardial cells and their surrounding interstitium. The extracellular volume (ECV) can increase in myocardial disease, especially through processes that lead to an accumulation of collagen. The increase can be diffuse or focal as in the case of infarction. The gold standard test, myocardial biopsy, has both significant morbidity and sampling error. T_1 mapping provides a non-invasive alternative method of quantifying fibrosis. ECV not only provides a physiologically intuitive unit of measurement, increased ECV is strongly associated with adverse outcomes (51).

Post-contrast T_1 values alone could be used to estimate the ECV, however, there are multiple factors that influence post-contrast myocardial T_1. By normalizing myocardial T_1 in relation to blood T_1, these factors can be ignored. The ECV is calculated using the change in T_1 values in myocardium and blood with contrast, and the haematocrit. Increased ECV has been found not only in diffuse myocardial diseases such as aortic stenosis (52), hypertrophic cardiomyopathy (52), and non-ischemic cardiomyopathy (45), but also in ischemic heart disease(53). In acutely infarcted myocardium, ECV is increased as a result of cellular breakdown. In chronic infarction, ECV remains elevated due to the development of replacement fibrosis. ECV increases in line with increasing levels of myocardial damage. It has been shown that the ECV of infarcted myocardium is higher than the ECV in other diseases causing myocardial fibrosis (54).

The ECV can be abnormal even in normal appearing myocardium in patients with ischemic cardiomyopathy (45). ECV increases with worsening left ventricular function. This finding correlates with pathological findings from explanted hearts of patients with ischemic cardiomyopathy (55), in which interstitial fibrosis in areas remote from infarction was increased over 2-fold in comparison to controls. Raised ECV has now been found to be a marker of short-term adverse outcomes in a broad range of patients (51), and, in fact, is a stronger marker of risk than left ventricular ejection fraction.

It can be shown that the ECV of salvaged myocardium is higher than that of the remote myocardium as a result of extracellular oedema. ECV can delineate the AAR from infarcted and normal myocardium (56). The post-contrast T_1 in the AAR has a value less than 2SD from the remote myocardium (50 ms approximately), and is, therefore, difficult to detect using LGE alone.

The combination of pre- and post-contrast images demonstrates that the ECV in the AAR is significantly elevated from that of remote myocardium.

3.8 Technical Aspects

T_1 mapping uses multiple scans with varying degrees of signal recovery to calculate T_1 values on a pixel-by-pixel basis, from which a parametric image can be reconstructed. Pixel intensities in these images correspond to T_1 values. These can then be presented as a grey-scale or colour map of the myocardium.

To produce raw data with varying degree of signal recovery, most T_1 mapping pulse sequences acquire images at different delay time following a 180° or 90° prepulse (inversion recovery or saturation recovery, respectively). Inversion pulses can only be used when the signal has recovered from all preceding experiments. In order to omit long waiting times, clinical inversion recovery-based techniques (e.g. modified Look-Locker inversion recovery, MOLLI (4)) are based on the method that was introduced by Look and Locker (57) and acquire data at multiple time points following a single inversion pulse. Inversion pulses provide higher dynamic range than saturation pulses, but the necessity to use multiple-readout schemes introduces a certain degree of heart rate dependence. This becomes relevant at high flip angles (>35° in balanced steady-state free precession) and high heart rates (>100 beats per minute) (23). Saturation pulses provide a lower dynamic range to start with but, when carried out separately for each raw image, allow for using high flip angles (e.g. 70°) without heart rate dependence (58). As a result, both approaches exhibit different levels of accuracy and precision.

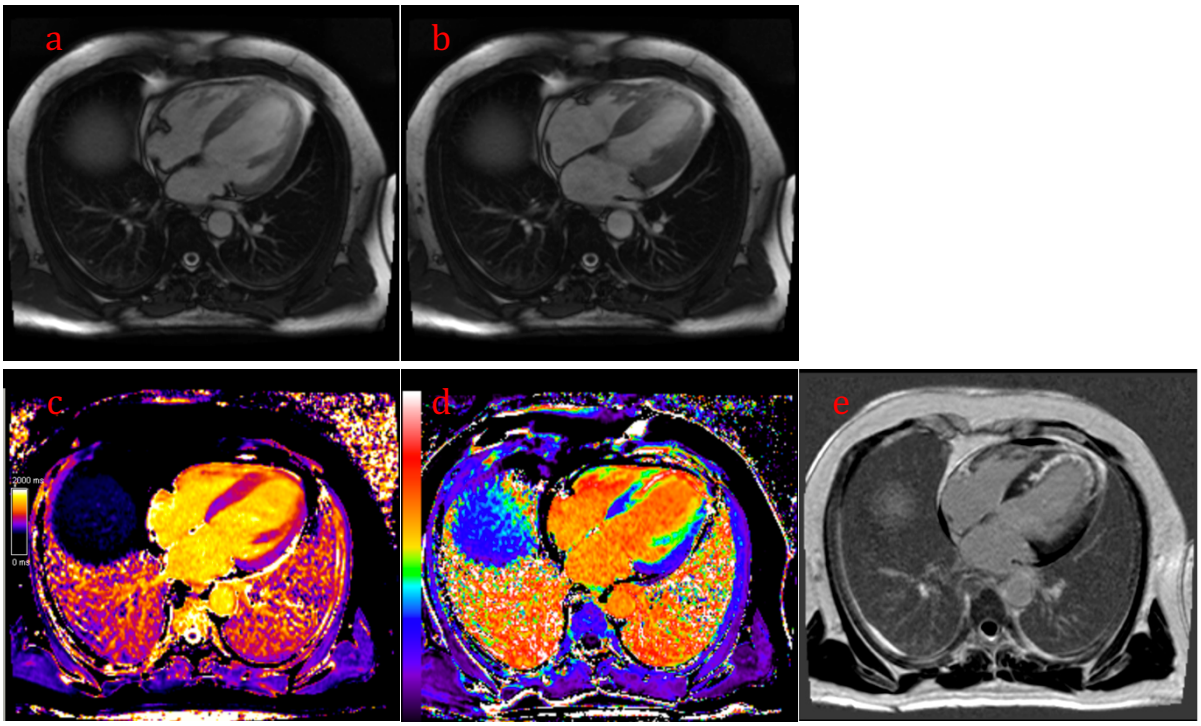

Figure 3-2. 4 chamber MR Imaging in a patient with recent antero-septal myocardial infarction. Upper Row - Cine MR imaging in diastole (a) and systole (b) demonstrating apical hypokinesia. Lower Row – (c) T_1 Mapping showing increased T_1 in the apico-septal region. (d) ECV mapping demonstrating varying degrees of transmural myocardial injury. (e) LGE imaging demonstrating apico-septal myocardial infarction.

3.8.1 Additional Factors Affecting T_1

Factors that influence T_1 itself include cardiac phase and field strength. The measured T_1 value will reflect the T_1 of blood flowing through the myocardium in addition to that of the myocardium. As myocardial blood flow occurs primarily during diastole, the phase in which the T_1 is measured, systole or diastole, affects T_1 measurement. Precontrast, arterial blood T_1 is higher than that of myocardium, resulting in higher T_1 in diastole than systole (59, 60).

Minor differences (2% approximately) have been noted in the measurement of T_1 both pre- and post-contrast between the septal and non-septal regions (59), this may be a result of a combination of factors, including magnetic susceptibility artefacts, receiver coil sensitivity, and signal gradient between septal and non-septal myocardium due to greater distance from the receiver coil elements. No difference, however, has been found between basal, mid and apical regions (61).

Gender and age appear to play a role in the range of normal T_1 values (62). Women have a higher ECV and native T_1 when compared with men. In men, there is a gradual increase in native T_1 value and ECV with age, whereas women appear to have fewer changes in ECV and T_1 with

age. Some of the differences in T_1 values between the genders may be related to haematocrit – the haematocrit will influence the value of the blood, with a lesser impact on the myocardial T_1 value. Women tend to have a lower haematocrit than men, leading to a higher T_1 values in blood, with a contribution to higher myocardial T_1 values. Normalisation for haematocrit has been found to eliminate differences between the genders (60). The changes in myocardial T_1 values with age would appear to be explained by the increased fibrosis found as part of normal aging.

Thinner walled myocardium is more challenging to assess accurately. A region of interest in thinner structures, may include a higher amount of voxels which include a contribution from the surrounding blood pool. As the T_1 in blood and myocardium are significantly different, this partial volume effect could result in artificially high native T_1, and artificially low post-contrast T_1 values. Therefore, thin walled myocardial infarctions and the relatively thin walls of the right ventricle are technically challenging to assess. However, with improvements in spatial resolution, T_1 mapping can be expected to overcome some of these challenges.

3.9 Potential of T_1 Mapping in Ischemic Heart Disease

Native and post contrast T_1 mapping provides previously unavailable insights into myocardial diseases, and, in particular, myocardial oedema and fibrosis. The recent consensus statement acts as a guide towards the standardisation of imaging techniques and reporting which will help increase the clinical use of these measurements (63).

T_1 mapping provides a quantitative method to complement both oedema imaging (STIR) and infarct imaging (LGE). An advantage of T_1 mapping is that by using a quantitative technique, both intra- and interobserver agreement are very high (59, 61). The data provided by pre and post contrast T_1 mapping could help in the diagnosis of patients with acute chest pain, distinguishing acute coronary syndromes from myocarditis and Takotsubo cardiomyopathy (64), and acute from chronic infarction.

In chronic ischemic heart disease, standardised T_1 thresholds or ECV values could detect and automatically quantify MI. In addition, the complexities of the area at risk could be analysed, looking for MVO and myocardial haemorrhage and assessing the peri-infarct zone. This could be of clinical importance, as some studies have found that MVO is a predictor of adverse outcomes.

The peri-infarct zone is a potentially important pathophysiological substrate for arrhythmias. Presumptively normal myocardium has been used in prior studies to differentiate the infarct core (eg, more than three standard deviations) from the heterogeneous peri-infarct zone, containing viable myocardium (eg, between two and three standard deviations). T_1 mapping could identify this border zone that may provide a substrate for ventricular tachycardia and sudden cardiac death (26).

T_1 mapping can help distinguish ischemic LGE from non-ischemic LGE (45). In addition, it can assess the “normal” appearing myocardium for fibrosis, as increases in ECV are closely linked to increased chances of adverse cardiac events (51).

T_1 mapping could be used to predict myocardial recovery of function after revascularization, where it offers a potential alternative to the conventional method that uses the percentage of transmurality. In the field of research, it offers a quantitative alternative to T_2 weighted methods to measure the area at risk from MI in NSTEMI and STEMI. Coronary microembolization is a frequent complication during percutaneous coronary intervention (PCI). As LGE using semiautomated thresholding underestimates myocardial damage (65), T_1 mapping techniques could identify areas of reversible and irreversible injury with the aim of improving revascularization techniques.

Diffuse myocardial fibrosis is a common histological feature of the failing heart. Endomyocardial biopsy (EMB) is the standard of reference for quantifying fibrosis but is an invasive procedure and prone to sampling error. It is known that the development of diffuse fibrosis is influenced by neurohormonal factors including angiotensin-converting enzyme, angiotensin II, catecholamines, and aldosterone. Pharmacological therapy with beta-blockers and angiotensin-converting enzyme inhibitors can reduce diffuse myocardial fibrosis (45). ECV has a low variability across scans, and could be a viable tool for evaluating clinical trial outcomes (66). This property may make it possible to non-invasively, serially, and quantitatively assess fibrosis in the non-infarcted myocardium as a potential endpoint for pharmacological intervention in heart failure, using small groups of patients, significantly reducing trial costs. Looking to the future, the use of CMR tissue characterization techniques in clinical trials as surrogate, mechanistic, and secondary end points may increase.

3.10 Conclusion

T_1 quantification has a long history in the study of ischemic heart disease. Recent imaging sequence developments allow T_1 values to be quickly and reproducibly quantified on a pixelwise basis and presented as T_1 maps using clinical MR systems. Oedema from acute myocardial ischemia and replacement fibrosis in chronic MI can be accurately detected and quantified. The combination of pre- and post-contrast images can not only identify and differentiate acute and chronic injury but also demonstrate a range of myocardial injury by measuring ECV.

The precise role of T_1 mapping in the evaluation of ischemic heart disease remains to be defined, however, its broad potential, and the fact it is a quantitative measurement show much promise for the future.

3.11 References:

(1) O h-Ici, D., Jeuthe, S., Al-Wakeel, N., Berger, F., Kuehne, T., Kozerke, S., and Messroghli, D.R. (2014). T1 mapping in ischaemic heart disease. *Eur. Heart J. Cardiovasc. Imaging* **15**(6), 597-602.

(2) Akber, S.F. (2008). Water proton relaxation times of pathological tissues. *Physiol. Chem. Phys. Med. NMR* **40**, 1-42.

(3) Damadian, R. (1971). Tumor detection by nuclear magnetic resonance. *Science* **171**(3976), 1151-3.

(4) Messroghli, D.R., Radjenovic, A., Kozerke, S., Higgins, D.M., Sivananthan, M.U., and Ridgway, J.P. (2004). Modified Look-Locker inversion recovery (MOLLI) for high-resolution T1 mapping of the heart. *Magn. Reson. Med.* **52**(1), 141-6.

(5) Piechnik, S.K., Ferreira, V.M., Dall'Armellina, E., Cochlin, L.E., Greiser, A., Neubauer, S., and Robson, M.D. (2010). Shortened Modified Look-Locker Inversion recovery (ShMOLLI) for clinical myocardial T1-mapping at 1.5 and 3 T within a 9 heartbeat breathhold. *J. Cardiovasc. Magn. Reson.* **12**, 69.

(6) Williams, E.S., Kaplan, J.I., Thatcher, F., Zimmerman, G., and Knoebel, S.B. (1980). Prolongation of proton spin lattice relaxation times in regionally ischemic tissue from dog hearts. *J. Nucl. Med.* **21**(5), 449-53.

(7) Been, M., Smith, M.A., Ridgeway, J.P., Brydon, J.W., Douglas, R.H., Kean, D.M., Best, J.J., and Muir, A.L. (1985). Characterisation of acute myocardial infarction by gated magnetic resonance imaging. *Lancet* **2**(8451), 348-50.

(8) Wisenberg, G., Prato, F.S., Carroll, S.E., Turner, K.L., and Marshall, T. (1988). Serial nuclear magnetic resonance imaging of acute myocardial infarction with and without reperfusion. *Am. Heart J.* **115**(3), 510-8.

(9) Been, M., Smith, M.A., Ridgway, J.P., Douglas, R.H., de Bono, D.P., Best, J.J., and Muir, A.L. (1988). Serial changes in the T1 magnetic relaxation parameter after myocardial infarction in man. *Br. Heart J.* **59**(1), 1-8.

(10) Abdel-Aty, H., Boye, P., Zagrosek, A., Wassmuth, R., Kumar, A., Messroghli, D., Bock, P., Dietz, R., Friedrich, M.G., and Schulz-Menger, J. (2005). Diagnostic performance of cardiovascular magnetic resonance in patients with suspected acute myocarditis: comparison of different approaches. *J. Am. Coll. Cardiol.* **45**(11), 1815-22.

(11) Marie, P.Y., Angioi, M., Carteaux, J.P., Escanye, J.M., Mattei, S., Tzvetanov, K., Claudon, O., Hassan, N., Danchin, N., Karcher, G.*, et al.* (2001). Detection and prediction of acute heart transplant rejection with the myocardial T2 determination provided by a black-blood magnetic resonance imaging sequence. *J. Am. Coll. Cardiol.* **37**(3), 825-31.

(12) Abdel-Aty, H., Zagrosek, A., Schulz-Menger, J., Taylor, A.J., Messroghli, D., Kumar, A., Gross, M., Dietz, R., and Friedrich, M.G. (2004). Delayed enhancement and T2-weighted cardiovascular magnetic resonance imaging differentiate acute from chronic myocardial infarction. *Circulation* **109**(20), 2411-6.

(13) Majno, G., and Joris, I. (1995). Apoptosis, oncosis, and necrosis. An overview of cell death. *Am. J. Pathol.* **146**(1), 3-15.

(14) Vinnakota, K.C., and Bassingthwaighte, J.B. (2004). Myocardial density and composition: a basis for calculating intracellular metabolite concentrations. *Am. J. Physiol. Heart Circ. Physiol.* **286**(5), H1742-9.

(15) Jennings, R.B., Ganote, C.E., and Reimer, K.A. (1975). Ischemic tissue injury. *Am. J. Pathol.* **81**(1), 179-98.

(16) Powell, W.J., Jr., DiBona, D.R., Flores, J., and Leaf, A. (1976). The protective effect of hyperosmotic mannitol in myocardial ischemia and necrosis. *Circulation* **54**(4), 603-15.

(17) Jennings, R.B., Schaper, J., Hill, M.L., Steenbergen, C., Jr., and Reimer, K.A. (1985). Effect of reperfusion late in the phase of reversible ischemic injury. Changes in cell volume, electrolytes, metabolites, and ultrastructure. *Circ. Res.* **56**(2), 262-78.

(18) Reimer, K.A., Jennings, R.B., and Hill, M.L. (1981). Total ischemia in dog hearts, in vitro 2. High energy phosphate depletion and associated defects in energy metabolism, cell volume regulation, and sarcolemmal integrity. *Circ. Res.* **49**(4), 901-11.

(19) Jennings, R.B., Reimer, K.A., and Steenbergen, C. (1986). Myocardial ischemia revisited. The osmolar load, membrane damage, and reperfusion. *J. Mol. Cell. Cardiol.* **18**(8), 769-80.

(20) Buja, L.M. (2005). Myocardial ischemia and reperfusion injury. *Cardiovasc Pathol* **14**(4), 170-5.

(21) Garcia-Dorado, D., and Oliveras, J. (1993). Myocardial oedema: a preventable cause of reperfusion injury? *Cardiovasc. Res.* **27**(9), 1555-63.

(22) Tranum-Jensen, J., Janse, M.J., Fiolet, W.T., Krieger, W.J., D'Alnoncourt, C.N., and Durrer, D. (1981). Tissue osmolality, cell swelling, and reperfusion in acute regional myocardial ischemia in the isolated porcine heart. *Circ. Res.* **49**(2), 364-81.

(23) Messroghli, D.R., Walters, K., Plein, S., Sparrow, P., Friedrich, M.G., Ridgway, J.P., and Sivananthan, M.U. (2007). Myocardial T1 mapping: application to patients with acute and chronic myocardial infarction. *Magn. Reson. Med.* **58**(1), 34-40.

(24) Dall'Armellina, E., Piechnik, S.K., Ferreira, V.M., Si, Q.L., Robson, M.D., Francis, J.M., Cuculi, F., Kharbanda, R.K., Banning, A.P., Choudhury, R.P., *et al.* (2012). Cardiovascular magnetic resonance by non contrast T1-mapping allows assessment of severity of injury in acute myocardial infarction. *J. Cardiovasc. Magn. Reson.* **14**, 15.

(25) Goldfarb, J.W., Arnold, S., and Han, J. (2007). Recent myocardial infarction: assessment with unenhanced T1-weighted MR imaging. *Radiology* **245**(1), 245-50.

(26) Yan, A.T., Shayne, A.J., Brown, K.A., Gupta, S.N., Chan, C.W., Luu, T.M., Di Carli, M.F., Reynolds, H.G., Stevenson, W.G., and Kwong, R.Y. (2006). Characterization of the peri-infarct zone by contrast-enhanced cardiac magnetic resonance imaging is a powerful predictor of post-myocardial infarction mortality. *Circulation* **114**(1), 32-9.

(27) Reimer, K.A., and Jennings, R.B. (1979). The "wavefront phenomenon" of myocardial ischemic cell death. II. Transmural progression of necrosis within the framework of ischemic bed size (myocardium at risk) and collateral flow. *Lab. Invest.* **40**(6), 633-44.

(28) Ugander, M., Zemedkun, M., Hsu, L.-Y., Oki, A.J., Booker, O.J., Kellman, P., Greiser, A., Aletras, A.H., and Arai, A.E. (2011). Non-contrast quantitative T1-mapping indicates that salvaged myocardium develops edema during coronary occlusion, whereas infarction exhibits evidence of additional reperfusion injury. *J. Cardiovasc. Magn. Reson.*(13 (Suppl 1)), O63.

(29) Nucifora, G., Aquaro, G.D., Masci, P.G., Barison, A., Todiere, G., Pingitore, A., and Lombardi, M. (2011). Lipomatous metaplasia in ischemic cardiomyopathy: current knowledge and clinical perspective. *Int. J. Cardiol.* **146**(1), 120-2.

(30) Ferreira, V.M., Holloway, C.J., Piechnik, S.K., Karamitsos, T.D., and Neubauer, S. (2013). Is it really fat? Ask a T1-map. *Eur. Heart J. Cardiovasc. Imaging.* **14**(11), 1060.

(31) Higgins, C.B., Herfkens, R., Lipton, M.J., Sievers, R., Sheldon, P., Kaufman, L., and Crooks, L.E. (1983). Nuclear magnetic resonance imaging of acute myocardial infarction in dogs: alterations in magnetic relaxation times. *Am. J. Cardiol.* **52**(1), 184-8.

(32) McNamara, M.T., Higgins, C.B., Schechtmann, N., Botvinick, E., Lipton, M.J., Chatterjee, K., and Amparo, E.G. (1985). Detection and characterization of acute myocardial infarction in man with use of gated magnetic resonance. *Circulation* **71**(4), 717-24.

(33) Vignaux, O., Dhote, R., Duboc, D., Blanche, P., Devaux, J.Y., Weber, S., and Legmann, P. (2002). Detection of myocardial involvement in patients with sarcoidosis applying T2-weighted, contrast-enhanced, and cine magnetic resonance imaging: initial results of a prospective study. *J. Comput. Assist. Tomogr.* **26**(5), 762-7.

(34) Lund, G., Morin, R.L., Olivari, M.T., and Ring, W.S. (1988). Serial myocardial T2 relaxation time measurements in normal subjects and heart transplant recipients. *J. Heart Transplant.* **7**(4), 274-9.

(35) Simonetti, O.P., Finn, J.P., White, R.D., Laub, G., and Henry, D.A. (1996). "Black blood" T2-weighted inversion-recovery MR imaging of the heart. *Radiology* **199**(1), 49-57.

(36) Friedrich, M.G., Kim, H.W., and Kim, R.J. (2011). T2-weighted imaging to assess post-infarct myocardium at risk. *JACC Cardiovasc. Imaging* **4**(9), 1014-21.

(37) Giri, S., Chung, Y.C., Merchant, A., Mihai, G., Rajagopalan, S., Raman, S.V., and Simonetti, O.P. (2009). T2 quantification for improved detection of myocardial edema. *J. Cardiovasc. Magn. Reson.* **11**, 56.

(38) Fernandez-Jimenez, R., Sanchez-Gonzalez, J., Aguero, J., Garcia-Prieto, J., Lopez-Martin, G.J., Garcia-Ruiz, J.M., Molina-Iracheta, A., Rossello, X., Fernandez-Friera, L., Pizarro, G.*, et al.* (2015). Myocardial edema after ischemia/reperfusion is not stable and follows a bimodal pattern: imaging and histological tissue characterization. *J. Am. Coll. Cardiol.* **65**(4), 315-23.

(39) Rapoport, S., Sostman, H.D., Pope, C., Camputaro, C.M., Holcomb, W., and Gore, J.C. (1987). Venous clots: evaluation with MR imaging. *Radiology* **162**(2), 527-30.

(40) Pedersen, S.F., Thrysoe, S.A., Robich, M.P., Paaske, W.P., Ringgaard, S., Botker, H.E., Hansen, E.S., and Kim, W.Y. (2012). Assessment of intramyocardial hemorrhage by T1-weighted cardiovascular magnetic resonance in reperfused acute myocardial infarction. *J. Cardiovasc. Magn. Reson.* **14**, 59.

(41) Fishbein, M.C., Maclean, D., and Maroko, P.R. (1978). The histopathologic evolution of myocardial infarction. *Chest* **73**(6), 843-9.

(42) O h-Ici, D., Ridgway, J.P., Kuehne, T., Berger, F., Plein, S., Sivananthan, M., and Messroghli, D.R. (2012). Cardiovascular magnetic resonance of myocardial edema using a short inversion time inversion recovery (STIR) black-blood technique: diagnostic accuracy of visual and semi-quantitative assessment. *J. Cardiovasc. Magn. Reson.* **14**, 22.

(43) Huber, S., Muthupillai, R., Cheong, B., Wible, J.H., Jr., Shah, D., Woodard, P., Grothues, F., Mahrholdt, H., Rochitte, C.E., Masoli, O.*, et al.* (2008). Safety of gadoversetamide in patients with acute and chronic myocardial infarction. *J. Magn. Reson. Imaging* **28**(6), 1368-78.

(44) Arai, A.E. (2011). Gadolinium can depict area at risk and myocardial infarction: a double-edged sword? *JACC Cardiovasc. Imaging* **4**(6), 619-21.

(45) Ugander, M., Bagi, P., Booker, J., Hsu, L.-Y., Oki, A., Greiser, A., Kellman, P., Aletras, A., and Arai, A. (2012). Understanding why edema in salvaged myocardium is difficult to detect by late gadolinium enhancement. *J. Cardiovasc. Magn. Reson.* **14**(Suppl 1), O63.

(46) Kloner, R.A., and Jennings, R.B. (2001). Consequences of brief ischemia: stunning, preconditioning, and their clinical implications: part 2. *Circulation* **104**(25), 3158-67.

(47) Aletras, A.H., Tilak, G.S., Natanzon, A., Hsu, L.Y., Gonzalez, F.M., Hoyt, R.F., Jr., and Arai, A.E. (2006). Retrospective determination of the area at risk for reperfused acute myocardial infarction with T2-weighted cardiac magnetic resonance imaging: histopathological and displacement encoding with stimulated echoes (DENSE) functional validations. *Circulation* **113**(15), 1865-70.

(48) Ubachs, J.F.A., Engblom, H., Koul, S., Kanski, M., Andersson, P., van der Pals, J., Carlsson, M., Erlinge, D., and Arheden, H. (2012). Myocardium at risk can be determined by ex vivo T2-weighted magnetic resonance imaging even in the presence of gadolinium: comparison to myocardial perfusion single photon emission computed tomography. *Eur Heart J Cardiovasc Imaging* **14**(3), 261-8.

(49) Buda, A.J., Aisen, A.M., Juni, J.E., Gallagher, K.P., and Zotz, R.J. (1985). Detection and sizing of myocardial ischemia and infarction by nuclear magnetic resonance imaging in the canine heart. *Am. Heart J.* **110**(6), 1284-90.

(50) Ugander, M., Bagi, P.S., Oki, A.J., Chen, B., Hsu, L.Y., Aletras, A.H., Shah, S., Greiser, A., Kellman, P., and Arai, A.E. (2012). Myocardial Edema as Detected by Pre-Contrast T1 and T2 CMR Delineates Area at Risk Associated With Acute Myocardial Infarction. *JACC Cardiovasc. Imaging* **5**(6), 596-603.

(51) Wong, T.C., Piehler, K., Meier, C.G., Testa, S.M., Klock, A.M., Aneizi, A.A., Shakesprere, J., Kellman, P., Shroff, S.G., Schwartzman, D.S.*, et al.* (2012). Association between extracellular matrix expansion quantified by cardiovascular magnetic resonance and short-term mortality. *Circulation* **126**(10), 1206-16.

(52) Flett, A.S., Hayward, M.P., Ashworth, M.T., Hansen, M.S., Taylor, A.M., Elliott, P.M., McGregor, C., and Moon, J.C. (2010). Equilibrium contrast cardiovascular magnetic resonance for the measurement of diffuse myocardial fibrosis: preliminary validation in humans. *Circulation* **122**(2), 138-44.

(53) Ugander, M., Oki, A.J., Hsu, L.Y., Kellman, P., Greiser, A., Aletras, A.H., Sibley, C.T., Chen, M.Y., Bandettini, W.P., and Arai, A.E. (2012). Extracellular volume imaging by magnetic resonance imaging provides insights into overt and sub-clinical myocardial pathology. *Eur. Heart J.* **33**(10), 1268-78.

(54) Sado, D.M., Flett, A.S., Banypersad, S.M., White, S.K., Maestrini, V., Quarta, G., Lachmann, R.H., Murphy, E., Mehta, A., Hughes, D.A.*, et al.* (2012). Cardiovascular magnetic resonance measurement of myocardial extracellular volume in health and disease. *Heart* **98**(19), 1436-41.

(55) Beltrami, C.A., Finato, N., Rocco, M., Feruglio, G.A., Puricelli, C., Cigola, E., Quaini, F., Sonnenblick, E.H., Olivetti, G., and Anversa, P. (1994). Structural basis of end-stage failure in ischemic cardiomyopathy in humans. *Circulation* **89**(1), 151-63.

(56) Ugander, M., Bagi, P.S., Booker, J.O., Hsu, L.-y., Oki, A.J., Greiser, A., Kellman, P., Aletras, A.H., and Arai, A.E. (2012). Understanding why edema in salvaged myocardium is difficult to detect by late gadolinium enhancement. *J. Cardiovasc. Magn. Reson.*(14 (Suppl 1)), O63.

(57) Look, D.C., and Locker, D.R. (1970). Time Saving in Measurement of NMR and EPR Relaxation Times. *Rev. Sci. Instrum.* **41**(2), 250-251.

(58) Chow, K., Flewitt, J.A., Green, J.D., Pagano, J.J., Friedrich, M.G., and Thompson, R.B. (2013). Saturation recovery single-shot acquisition (SASHA) for myocardial T1 mapping. *Magn. Reson. Med.*

(59) Kawel, N., Nacif, M., Zavodni, A., Jones, J., Liu, S., Sibley, C.T., and Bluemke, D.A. (2012). T1 mapping of the myocardium: Intra-individual assessment of the effect of field strength, cardiac cycle and variation by myocardial region. *J. Cardiovasc. Magn. Reson.* **14**(1), 27.

(60) Reiter, U., Reiter, G., Dorr, K., Greiser, A., Maderthaner, R., and Fuchsjager, M. (2014). Normal diastolic and systolic myocardial T1 values at 1.5-T MR imaging: correlations and blood normalization. *Radiology* **271**(2), 365-72.

(61) Messroghli, D.R., Plein, S., Higgins, D.M., Walters, K., Jones, T.R., Ridgway, J.P., and Sivananthan, M.U. (2006). Human myocardium: single-breath-hold MR T1 mapping with high spatial resolution--reproducibility study. *Radiology* **238**(3), 1004-12.

(62) Liu, C.Y., Liu, Y.C., Wu, C., Armstrong, A., Volpe, G.J., van der Geest, R.J., Liu, Y., Hundley, W.G., Gomes, A.S., Liu, S.*, et al.* (2013). Evaluation of age-related interstitial myocardial fibrosis with cardiac magnetic resonance contrast-enhanced T1 mapping: MESA (Multi-Ethnic Study of Atherosclerosis). *J. Am. Coll. Cardiol.* **62**(14), 1280-7.

(63) Moon, J.C., Messroghli, D.R., Kellman, P., Piechnik, S.K., Robson, M.D., Ugander, M., Gatehouse, P.D., Arai, A.E., Friedrich, M.G., Neubauer, S.*, et al.* (2013). Myocardial T1 mapping and extracellular volume quantification: a Society for Cardiovascular Magnetic Resonance (SCMR) and CMR Working Group of the European Society of Cardiology consensus statement. *J. Cardiovasc. Magn. Reson.* **15**, 92.

(64) Ferreira, V., Piechnik, S., Dall'Armellina, E., Karamitsos, T., Francis, J., Friedrich, M., Robson, M., and Neubauer, S. (2011). Quantification of acute myocardial injury by ShMOLLI T1-Mapping, T2-weighted and late gadolinium imaging in patients presenting with chest pain, positive troponins and non-obstructive coronary arteries. *J. Cardiovasc. Magn. Reson.* **13**(Suppl 1), P16.

(65) Saeed, M., Hetts, S.W., Do, L., and Wilson, M.W. (2013). Coronary Microemboli Effects in Preexisting Acute Infarcts in a Swine Model: Cardiac MR Imaging Indices, Injury Biomarkers, and Histopathologic Assessment. *Radiology* **268**(1), 98-108.

(66) Liu, S., Han, J., Nacif, M.S., Jones, J., Kawel, N., Kellman, P., Sibley, C.T., and Bluemke, D.A. (2012). Diffuse myocardial fibrosis evaluation using cardiac magnetic resonance T1 mapping: sample size considerations for clinical trials. *J. Cardiovasc. Magn. Reson.* **14**, 90.

Chapter 4 - Closed Chest Model of Ischemia reperfusion

4.1 Abstract

Current models for real-time study of the effects of myocardial ischemia/reperfusion (I/R) have major limitations and confounders, including the surgical stresses of a thoracotomy and the abnormal physiology of an open chest. The need to reposition the animal after induction and termination of ischemia in conventional models interferes with the study of the early changes associated with ischemia, rendering a direct comparison of pre-ischemia and post-ischemia images difficult. We developed a novel “closed chest” model of I/R to overcome these issues (1).

Following thoracotomy, we sutured a balloon occluder to the left coronary artery (LCA). We used both visual inspection and ECG to assess for successful occlusion and reperfusion of the coronary artery at the time of operation by brief inflation and deflation of the balloon. The tubing was then placed under the skin, and the incision closed. Following a recovery period (5-10 days), the animals underwent MRI. We performed a baseline assessment of left ventricular (LV) function, then inflated the balloon was inflated and repeated LV measurement using cine MRI.

The occluder was successfully placed in 40 of 44 animals. 4 developed intraoperative complications; 2 large myocardial infarction, 2 terminal bleeding. 6 died in the week following surgery, (4 sudden deaths (presumed arrhythmic), 1 anterior infarction, 1 sepsis). Cine-MRI demonstrated localised hypokinesia in 31 of the remaining 34 animals. LV ejection fraction (EF) was reduced from 63% ± 7% at baseline to 49% ± 9% during coronary occlusion. LV EF removed to 61% ± 2%. The area at risk as measured by staining of the heart was 41.9% ± 16%.

This method allows the effects of ischemia/reperfusion to be studied before, during, and after coronary occlusion. Ischemia can be caused while the animal is in the MRI. This new and clinically relevant small animal model is a valuable tool to study the effects of single or repeated coronary occlusion/reperfusion in real-time.

4.2 Background

Experimental myocardial occlusion has been used as a model to study the effects of coronary ischemia (2, 3) and ischemia/reperfusion (3) for many years. Initial studies involved the use of larger mammals (dogs, pigs, etc.) but issues of cost and ethics led to the increasing use of small animals such as mice and rats as models for cardiovascular disease.

Models of myocardial ischemia in small animals have typically used one of a number of open-chest techniques. The basic permanent occlusion model is one where the left coronary artery (LCA) is sutured closed (4). The simplest open chest myocardial ischemia/reperfusion (I/R) models involve a suture fastened around the LCA for a period before being released (5). In an alternative model, a suture is passed around the LCA, and then both ends are passed through a piece of plastic tubing. Tightening the suture and securing it causes ischemia, releasing the suture allows reperfusion. Closed chest models have been developed involving the use of snares (6, 7) or a system of sutures around the LCA (8).

However, all of these models have important limiting factors. While the animal is in the coil, access is limited. The need to induce ischemia, then place the animal in the coil means the study of the initial, or of brief periods of ischemia, is not possible. Ideally, animals would be studied at baseline, during, and following I/R. The need to reposition and repeat the localiser scans following each manipulation can interfere with this.

All open-chest models involve a high mortality in the first 24 hours, for example, 40-50% in the paper from Pfeffer et al. (4). This mortality not only plays an important role in the planning of experiments but also is a significant factor in animal welfare and ethical approval of studies.

Our study goal was to develop a closed-chest model of I/R in the rat allowing for repetitive opening and occlusion of a coronary artery in both laboratory and CMR environments.

4.3 Methods

All procedures were approved by local animal care authorities. Male Sprague Dawley rats (n=44, weight 367 ± 67 g) underwent thoracotomy for surgical preparation of the coronary arteries. After a recovery period of 5 to 7 days, animals were taken to an MRI system and subjected to coronary occlusion (15 - 90 minutes) and subsequent reperfusion while in the MRI.

The occluder (VO-1.5F, DocXS Biomedical Products, Ukiah, CA, USA) consists of a length of silicone rubber tubing of 1.5 mm diameter with an inflatable balloon of 3.5mm width with an eyelet at one end (Figure 4-1). The balloon can be secured in place with suture material via the eyelet. The balloon is inflated by injecting air or liquid into the balloon and deflated by simply withdrawing the air or liquid. A 20G cannula or blunted needle may be used to access the tubing. A cannula can be attached to extension tubing of various lengths to allow inflation and deflation of the balloon from a distance.

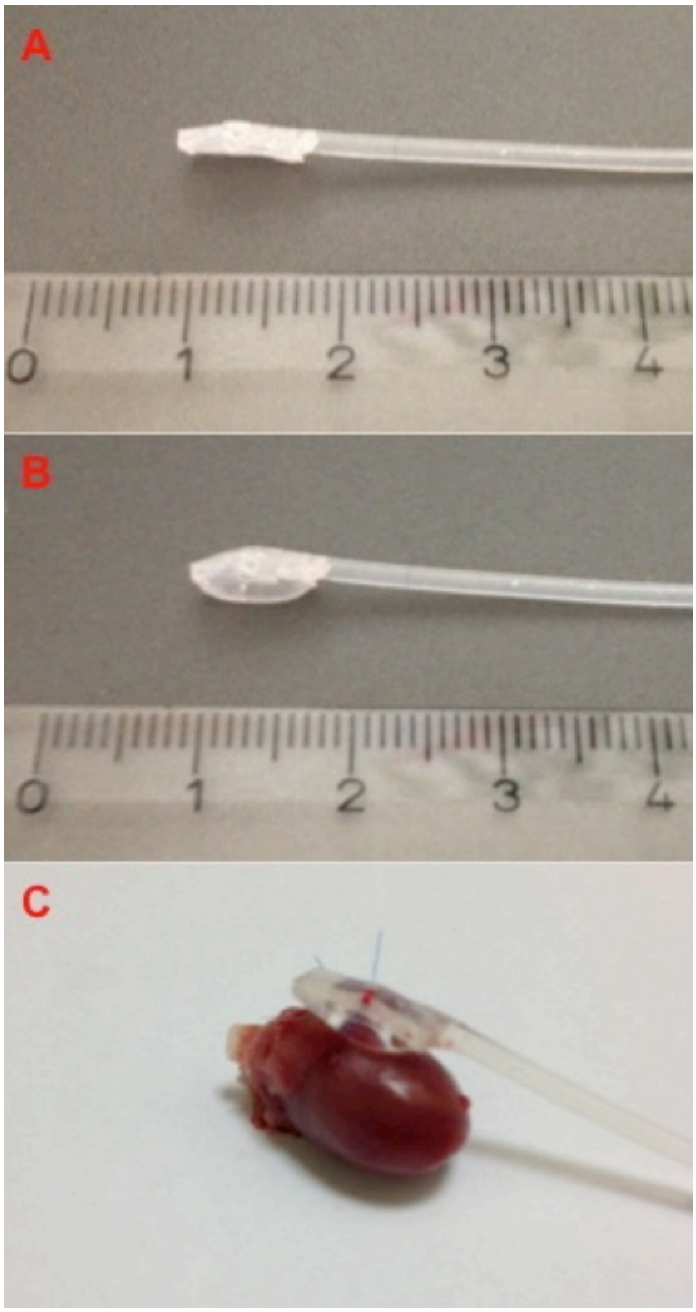

Figure 4-1. Photos of the occluder when deflated (A and B) and in-situ in an ex-vivo rat heart (C).

4.3.1 Surgery

Rats were anaesthetized with an initial dose of 4% isoflurane in an air/oxygen (4:1) mixture using an induction chamber, intubated, and ventilated at a rate of 70 breaths per minute (7025 Rodent Ventilator, Ugo Basile, Comerio VA – Italy). Anesthesia was maintained using 1.5-2% Isoflurane in an air/oxygen (4:1) mixture during the surgery. Body temperature was recorded and maintained at 37.5° using a flexible rectal temperature-sensing probe with Homeothermic Blanket Control Unit (Harvard Apparatus). ECG electrodes were attached to the paws, and a baseline ECG was obtained (PowerLab, AD Instruments, Colorado Springs, CO, USA). Heart rate and ECG were continuously monitored during the surgery (PowerLab, AD Instruments, Colorado Springs, CO, USA).

We performed an incision in the left mid-clavicular line then with blunt dissection separated the pectoralis muscles to expose the ribcage. A Barraquer eye speculum was used to keep the chest muscles widely separated. Thoracotomy was performed via fourth intercostal space. A rib spreader was used to obtain a clear view of the heart. The pericardium was gently torn open, avoiding damage to the heart or blood vessels.

In the rat, the LCA consists of a single vessel with few branches. There is no true circumflex, and collaterals are rare. This allows the creation of large, quite uniform areas of ischemia/infarction. A 6-0 Ethicon prolene blue monofilament polypropylene suture was passed under the LCA, from below the left atrial appendage to below the pulmonary outflow tract. The suture was then passed through the eyelet of the occluder. Finally, the occluder was loosely secured around the mid-portion of the LCA (Figure 4-1). Briefly inflating and deflating the balloon tested for reversible occlusion. Both the ECG, with ST segment elevation and resolution, and reversible myocardial blanching and hypokinesis, were used to confirm ischemia. The non-balloon end of the occluder was then passed from the chest cavity, via the second intercostal space, and looped in a pouch created under the skin of the animal. After instrumentation, the chest was closed following the evacuation of the air inside the chest. After surgery, the animals were placed in a recovery cage for 2 hours, then transferred to the animal care facility for further recovery. Animals received 0.03 mg/kg of buprenorphine subcutaneously pre-operatively, followed by a further dose ever 8-12 hours if required. Rats were also given Acetaminophen 5mg/ml in their drinking water for 72 hours following surgery.

4.3.2 MRI

After induction of inhalative anaesthesia (isoflurane-oxygen, 2.5%) and weighing, the feet were cleaned before attaching MRI-compatible electrocardiogram (ECG) electrodes. A small incision was performed to locate the occluder tubing. The distal end was then attached to a 20G plastic cannula and 3-way stopcock. Extension tubing was attached to allow the balloon to be inflated and deflated from a distance of 1 metre. The animals were then placed on and fixed to a dedicated animal bed, and the bed then positioned within the MRI coil. A warm water heating mat was placed over the rat. The temperature was monitored using a fibre-optic rectal probe (Luxtron FOT Lab Kit, LumaSense Technologies, Inc., Santa Clara, USA) and maintained at 37C ± 1°C. Throughout the examination, anaesthesia was maintained via inhalation of isoflurane-oxygen (0.8– 1.5%). After the initial MRI images were acquired, the artery was occluded for 15 minutes. Occlusion was confirmed with ECG Tracing and by hypokinesis of the LV wall on cine MR imaging.

Following the specified duration of ischemia, the occluder was opened. Animals were then maintained in the scanner for a minimum of 90 minutes, before being removed. The animals were subsequently euthanized and the hearts removed for staining.

A 3-T clinical MRI system (Achieva; Philips Healthcare, Best, The Netherlands) equipped with a dedicated solenoid coil for rats was used for all studies. After generation of survey images and of a long-axis set of cine images, a stack of left ventricular (LV) short-axis cine images was acquired (phases, 30; repetition time, 6.8 ms; echo time, 3.3 ms; flip angle, 15°; field of view, 80 x 64 mm; acquired voxel size, 0.4 x 0.4 x 1.5 mm; number of signal averages, 2; slices, 7; interslice gap adjusted to allow for coverage of the entire LV range, -0.3 to 0.0 mm, where a negative gap refers to a slice overlap). Short axis cine images were repeated after inflation of the occluder to assess LV function.

Histology was performed to confirm the presence of infarction and assess the area-at-risk in all animals similarly to methods previously described (9). Animals were euthanized by exsanguination following an overdose of isoflurane anesthetic. Briefly, the heart with occluder attached was swiftly removed. Re-inflating the occluder balloon re-occluded the LCA. Evan's blue dye (2%, 1 ml) was injected retrogradely into the ascending aorta to delineate the area at risk (Figure 4-2). The heart was cut parallel to the atrio-ventricular groove at the centre of the risk

area. It was then cut into 1-mm thick slices that were incubated in 1% triphenyltetrazolium chloride (TTC) at 37°C for 20 min. Viable myocardium stains red while necrotic myocardium remains unstained by TTC. The slices were photographed using a colour camera (Canon Powershot G12). The images were stored on a computer and analysed using ImageJ (Rasband, W.S., ImageJ, U.S. National Institutes of Health, Bethesda, Maryland, USA, http://imagej.nih.gov/ij/, 1997-2011). The area stained by a blue dye is identified as perfused area and the unstained area as the area at risk (AAR). The infarcted area is identified as the unstained white area by TTC. AAR was normalized by the whole LV area as AAR/LV.

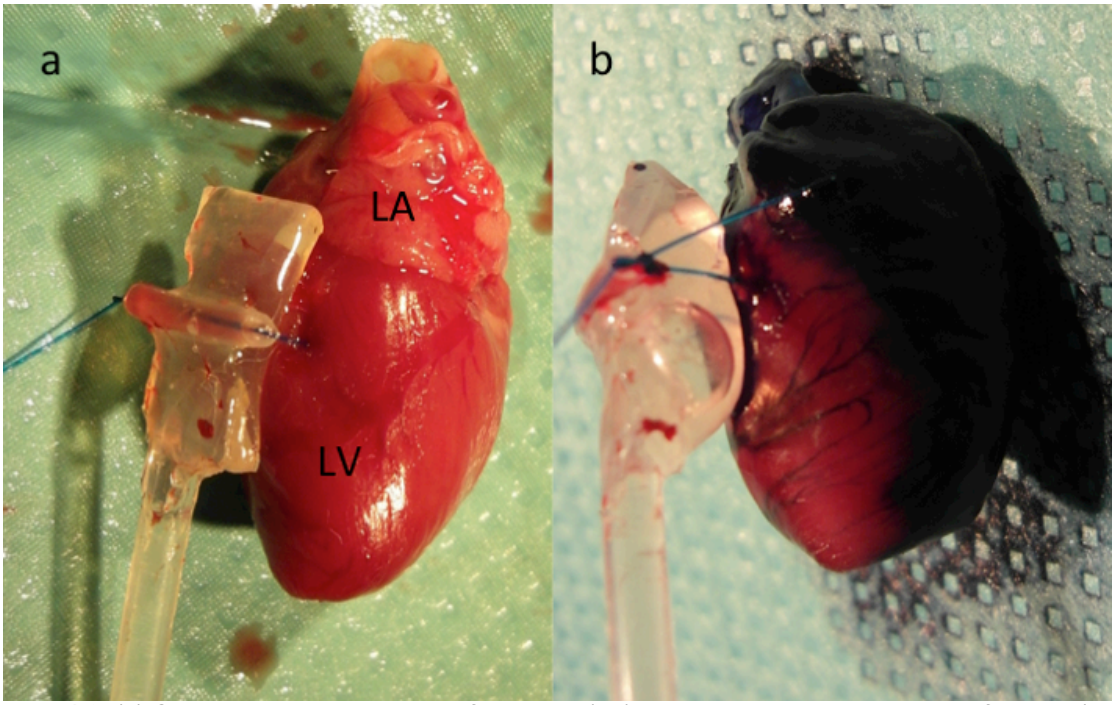

Figure 4-2. (a) Occluder in position on the left ventricle (LV), sutured in position below the left atrium (LA). (b) Reinflating the occluder occludes the left coronary artery. Blue dye is then perfused into the aorta but does not enter the territory of the occluded artery.

4.4 Results

4.4.1 Surgery

40 of 44 animals operated had the coronary occluder successfully placed. Typical intraoperative ECG findings can be seen in Figure 4-3, showing ST elevation and normalization on inflation and deflation of the occluder. Immediate mortality of the surgical procedure was low at 9% (2 animals developed a large infarction following occluder placement and were euthanized. 2 animals developed terminal bleeding following passage of the needle through the myocardium). Most animals resumed normal behaviour shortly after the surgery.

In the week following the surgery, 6 of the remaining animals died, (4 sudden deaths (presumed arrhythmic), 1 large anterior infarction, 1 abdominal sepsis from intraoperative injury).

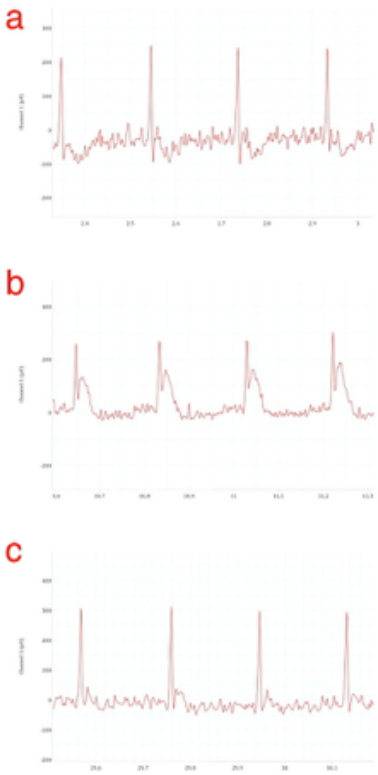

Figure 4-3. Sample ECG of the Rat showing (a) normal ECG prior to occluder inflation, (b) ST elevation on occluder inflation, and (c) ST resolution following occluder deflation

4.4.2 MRI

We had successful I/R in 31 of the remaining 34 animals. I/R was confirmed by cine MRI, which demonstrated localised myocardial hypokinesia (Figure 4-4). Typical ECG changes of ST segment change, followed by loss of R wave height were seen in 29 of the 33 animals. Arrhythmia (ventricular ectopy or ventricular fibrillation) developed in most animals (29 of the 31 with confirmed ischemia). One animal developed terminal ventricular fibrillation following 15 minutes of myocardial ischemia; however, all other animals spontaneously reverted to sinus rhythm, even after prolonged periods of arrhythmia (up to 90 seconds).

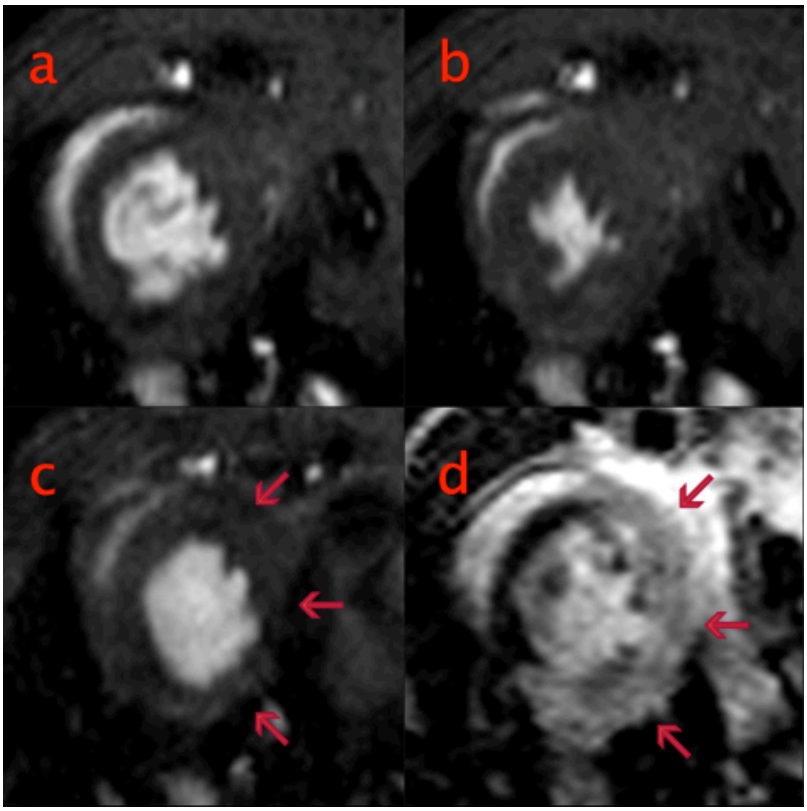

Figure 4-4. SSFP Short Axis still images through the left ventricle (LV) before occluder inflation in diastole (a). Normal LV systolic function can be seen in the systolic image (b). A large area of anterolateral hypokinesia (arrows) can be seen during occluder inflation (c). Inversion recovery images early following gadolinium injection (d) demonstrate the hyperenhanced anterolateral area at risk (arrows).

Baseline LV ejection fraction (EF) was measured at 63% ± 7%. During coronary occlusion, EF decreased to 49% ± 9% during coronary occlusion. Following reopening of the artery, LV EF removed to 61% ± 2% one hour following reperfusion.

In the 3 animals without changes in the ECG or LV function, the occluder was not surrounding the LCA (2 animals) or the suture fastening the occluder to the myocardium had become loose (1 animal).

After removing the heart, we were able to re-occlude the coronary artery by reinflating the occluder in all animals with confirmed ischemia. The AAR was 41.9% ± 16%. Typical staining of the heart can be seen in Figure 4-5. The AAR of infarction remains red while the rest of the heart, supplied by the right coronary artery is stained dark blue. In addition, one animal also had a small infarction localised to the area of suture placement.

.

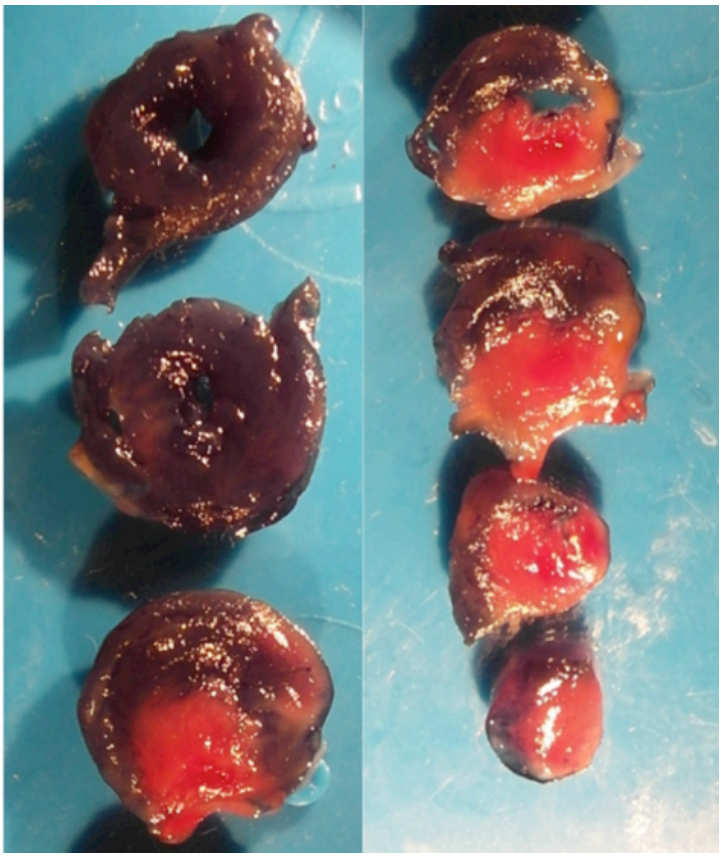

Figure 4-5. Staining of the heart showing the large area at risk of myocardial infarction (stained red) supplied by the left coronary artery. The myocardium stained blue is supplied by the right coronary artery.

4.5 Discussion

In this study, we present a novel small animal model that allows for studying the effects of I/R with or without preceding or subsequent episodes of brief occlusion (conditioning) in space-constrained environments such as MRI.

The availability of realistic small animal models is important for cardiovascular research, as preclinical studies help to generate and test hypotheses for new therapeutic strategies and provide the link between basic and clinical research. The presented model allows the investigation of the course and mechanisms of I/R without confounding influences from major surgery. Furthermore, the effects of ischemic preconditioning and postconditioning can be studied as opening and occlusion of the coronary artery can be performed repetitively.

The extent of myocardial damage that is caused by myocardial ischemia is not only determined by the duration of coronary occlusion, but also by the metabolic pathways that are activated immediately before, during, and after ischemia. In the open-chest model, a number of factors can cause systemic stresses that influence these pathways. Surgical blood loss may cause

hypovolemia leading to increased sympathetic activity and ultimately to acidosis, endothelial dysfunction, and redox state, as well as stimulation of inflammatory and anti-inflammatory cascades. Surgery itself causes an inflammatory response. Lifting and moving the heart to access the LCA can directly damage the heart, or result in twisting or kinking of the aorta, which reduces coronary blood flow and act as an unwanted preconditioning episode. Ventricular geometry may change with the removal of the pericardium in an open chest. Finally, the open chest exposes the core of the body, increasing the risk of hypothermia. Mechanical ventilation can further exacerbate this problem. Hypothermia can critically influence the experimental outcome. For example, a fall in temperature by only 1°C reduces infarct size by 10% (10).

The use of a closed-chest model allows for separating surgery-related systemic effects from the specific effects of I/R experiments. In a previous experiment, Michael et al. (6) found that, in sham-operated animals, the acute surgical trauma associated with open-chest preparations resulted in significant and highly variable background levels of inflammation. These systemic effects could interfere with the measurement of inflammation due to I/R. Other studies have looked at the effects of the open-chest model on the recovery of systolic thickening after ischemia and found that the open chest model greatly exaggerated the effects of myocardial stunning (11). The time required to minimise the confounding effects of surgery is unknown. Inflammatory processes including leukocyte recruitment play a major role in the extension of myocardial damage after ischemia and reperfusion (12). Sham-operated animals have been found to have significant levels of inflammation, which can be indistinguishable from that of animals that undergo I/R (13). It has been shown that inflammatory markers (TNF-α and IL-6 mRNA) in sham-operated mice return to normal within three days of operation (14). In our experiments, we waited at least five days from time of operation to allow the effects of the operation to be minimised.

In our series, the model was associated with a mortality rate of 23%, with only one animal dying during the I/R experiments. For open-chest models, examples of mortality rates range from 35% (15) to 65% (16). A reduction in overall mortality could be expected, as the I/R experiments are performed when the animals have recovered from the impact of the thoracotomy and thus are in a much more stable condition. The AAR in our experiments was broadly similar to other techniques of myocardial ischemia and infarction, such as 4-59% in the paper from Pfeffer et al.

(4). Technically, the operation is very similar to the traditional suturing of a coronary artery, and, therefore, those skilled in the basic procedure should be able to perform this operation without significant difficulty.

Between the thoracotomy and I/R experiments, the tubing of the occluder was placed subcutaneously. Exposed tubing would act as an infection source, and animals could not be housed in groups in cages, which is a less stressful arrangement than isolated housing.

The ability to occlude the artery without disturbing the position of the animal is crucial for imaging experiments. If the animal remains in the same position, the pre- and post-occlusion images can be compared without a need for repeated scanning or the need for image correction.

MRI has been shown to detect myocardial oedema and wall motion abnormalities in clinical patients. With the proposed model, MRI can be used for comprehensive non-invasive characterization of the course of myocardial injury during experimental I/R.

4.6 Conclusion

In summary, the presented model overcomes several limitations of previous models and enables in-vivo research in the effects of various schemes of I/R on the myocardium in rats. It provides the possibility of causing myocardial ischemia of varying durations, with the advantage of not having to reposition the animal. This is crucial to study the rapid metabolic and structural changes that occur during myocardial ischemia.

4.7 References:

(1) O h-Ici, D., Jeuthe, S., Dietrich, T., Berger, F., Kuehne, T., Kozerke, S., and Messroghli, D.R. (2015). Closed-chest small animal model to study myocardial infarction in an MRI environment in real time. *Int. J. Cardiovasc. Imaging* **31**(1), 115-21.

(2) Heimburger, R.F. (1946). Injection into pericardial sac and ligation of coronary artery of the rat. *Arch. Surg.* **52**, 677-89.

(3) Selye, H., Bajusz, E., Grasso, S., and Mendell, P. (1960). Simple techniques for the surgical occlusion of coronary vessels in the rat. *Angiology* **11**, 398-407.

(4) Pfeffer, M.A., Pfeffer, J.M., Fishbein, M.C., Fletcher, P.J., Spadaro, J., Kloner, R.A., and Braunwald, E. (1979). Myocardial infarct size and ventricular function in rats. *Circ. Res.* **44**(4), 503-12.

(5) Smith, E.F., 3rd, Egan, J.W., Bugelski, P.J., Hillegass, L.M., Hill, D.E., and Griswold, D.E. (1988). Temporal relation between neutrophil accumulation and myocardial reperfusion injury. *Am. J. Physiol.* **255**(5 Pt 2), H1060-8.

(6) Michael, L.H., Entman, M.L., Hartley, C.J., Youker, K.A., Zhu, J., Hall, S.R., Hawkins, H.K., Berens, K., and Ballantyne, C.M. (1995). Myocardial ischemia and reperfusion: a murine model. *Am. J. Physiol.* **269**(6 Pt 2), H2147-54.

(7) Sievers, R.E., Schmiedl, U., Wolfe, C.L., Moseley, M.E., Parmley, W.W., Brasch, R.C., and Lipton, M.J. (1989). A model of acute regional myocardial ischemia and reperfusion in the rat. *Magn. Reson. Med.* **10**(2), 172-81.

(8) Himori, N., and Matsuura, A. (1989). A simple technique for occlusion and reperfusion of coronary artery in conscious rats. *Am. J. Physiol.* **256**(6 Pt 2), H1719-25.

(9) Schwarz, E.R., Somoano, Y., Hale, S.L., and Kloner, R.A. (2000). What is the required reperfusion period for assessment of myocardial infarct size using triphenyltetrazolium chloride staining in the rat? *J. Thromb. Thrombolysis* **10**(2), 181-7.

(10) Chien, G.L., Wolff, R.A., Davis, R.F., and van Winkle, D.M. (1994). "Normothermic range" temperature affects myocardial infarct size. *Cardiovasc. Res.* **28**(7), 1014-7.

(11) Triana, J.F., Li, X.Y., Jamaluddin, U., Thornby, J.I., and Bolli, R. (1991). Postischemic myocardial "stunning". Identification of major differences between the open-chest and the conscious dog and evaluation of the oxygen radical hypothesis in the conscious dog. *Circ. Res.* **69**(3), 731-47.

(12) Jolly, S.R., Kane, W.J., Hook, B.G., Abrams, G.D., Kunkel, S.L., and Lucchesi, B.R. (1986). Reduction of myocardial infarct size by neutrophil depletion: effect of duration of occlusion. *Am. Heart J.* **112**(4), 682-90.

(13) Bohl, S., Medway, D.J., Schulz-Menger, J., Schneider, J.E., Neubauer, S., and Lygate, C.A. (2009). Refined approach for quantification of in vivo ischemia-reperfusion injury in the mouse heart. *Am. J. Physiol. Heart Circ. Physiol.* **297**(6), H2054-8.

(14) Nossuli, T.O., Lakshminarayanan, V., Baumgarten, G., Taffet, G.E., Ballantyne, C.M., Michael, L.H., and Entman, M.L. (2000). A chronic mouse model of myocardial ischemia-reperfusion: essential in cytokine studies. *Am. J. Physiol. Heart Circ. Physiol.* **278**(4), H1049-55.

(15) Fu, Y., Wang, Z., Chen, W.L., Moore, P.K., and Zhu, Y.Z. (2007). Cardioprotective effects of nitric oxide-aspirin in myocardial ischemia-reperfused rats. *Am. J. Physiol. Heart Circ. Physiol.* **293**(3), H1545-52.

(16) MacLeod, B.A., Augereau, P., and Walker, M.J. (1983). Effects of halothane anesthesia compared with fentanyl anesthesia and no anesthesia during coronary ligation in rats. *Anesthesiology* **58**(1), 44-52.

Chapter 5 - Validation of SALLI Imaging

5.1 Abstract

Small-Animal Look-Locker Inversion Recovery (SALLI) is a multi-modal imaging method that simultaneously generates cardiac T_1 maps, cine MRI and inversion recovery (IR)-prepared images for high heart rates. T_1 mapping by SALLI has been validated against histology in an animal model of hypertensive heart disease (1), however the assessment of left ventricular (LV) function by SALLI-Cine MR and infarct size by SALLI-LGE have not yet been validated. Our aim was to compare the measurement of LV function between the SALLI-Cine sequence and the standard Cine MRI sequence, and infarct size between late gadolinium enhancement (LGE) using SALLI-LGE and histology.

Six healthy rats and 18 rats with surgically induced myocardial infarction were imaged. MRI was performed on a whole-body 3.0T MR unit with a 70 mm solenoid coil for rats. A stack of LV short-axis cine images was acquired from apex to base. Short axis SALLI MR imaging was performed in the same seven short axis orientations, before and after gadolinium contrast injection. Following imaging, the hearts were harvested, stained with triphenyltetrazolium chloride (TTC) and infarct size was measured. Image quality was visually assessed and compared between imaging modalities and between pre- and post-contrast SALLI images. Ejection fraction was compared between standard cine and SALLI-Cine imaging. Infarct size by SALLI-LGE was compared with infarct size by TTC staining.

Image quality was good or adequate in all cases. LV function and infarct size were similar with SALLI-Cine vs. Cine (EF 59.8 ± 12% vs. 60.8 ± 12%, p=0.42) and SALLI-LGE vs. histology (infarct size 21.9 ± 18% vs. 23.5 ± 18%, p=0.28), respectively. SALLI-LGE generated good contrast between infarcted and normal myocardium, however, contrast between blood and infarcted myocardium was less marked. Image quality was similar between the pre- and post-contrast SALLI-Cine images, with comparable measured ejection fraction.

SALLI multimodal imaging provides an alternative to conventional cine MR and IR sequences. SALLI measurements of ejection fraction and infarct size are comparable to standard MR Cine imaging and histology across a range of ventricular function and infarct sizes. Image quality is comparable between both MRI methods. SALLI offers an efficient alternative method to

conventional Cine MR and LGE MR imaging methods. As SALLI generates multimodal images from the same dataset, this approach could not only be time saving but has the advantage of allowing direct comparison of findings without further image registration.

5.2 Introduction

Cardiac Magnetic Resonance Imaging (CMR) is the clinical reference standard for assessment of ventricular function and detection of myocardial infarction (2). When compared to standard clinical MRI, small animal MRI presents additional challenges, including the high heart rates (200 to 600 beats per minute) and small size of the animals. To maximise the signal-to-noise ratio, most small animal imaging is carried out on dedicated high field systems with field strengths ranging from 4.7 to 11 Tesla (T) (3). However, these dedicated scanners are not as widely available as standard clinical scanners, which operate at lower field strengths of 1.5 to 3 T. In addition, dedicated pulse sequences are required to allow cardiac imaging. The ability to perform imaging on clinical scanners in a time efficient manner could allow the development of new research opportunities.

However, there are a number of challenges in adapting these scanners for small animal CMR. Reliable ECG signal is required to perform triggered imaging. Options to allow this include the use of neonatal electrodes attached to the clinical ECG system, or a dedicated small animal ECG monitor. The software on the scanner should be adjusted to allow for the high heart rates of the small animals. As breath holding is not possible, signal averaging or respiratory gating is required to minimize the artefact from respiratory motion.

Anaesthesia is required for the examination. Inhaled anaesthetics, such as isoflurane, are the most practical method, however, specialised small animal gas delivery and extraction systems are then required. These anaesthetics have been found to have minimal effects on cardiac function (4). As animal temperature rapidly falls during anaesthesia, temperature needs to be monitored and controlled by the use of heating pads or warm water systems.

The spatial resolution required in small animal imaging is 5-10 times that of standard clinical imaging, with a resulting loss in SNR. This places increased demands on the hardware, requiring high field strengths with strong and fast switching gradients. These need to be combined with dedicated small animal radiofrequency receiver coils, although other small volume coils such as wrist coils can be used.

In small animals, the most frequently used method to study cardiac structure and function is a T_1-weighted cine gradient-echo (GRE) technique (Figure 5-1). This pulse sequence acquires data

from multiple heart phases for a single imaging slice. As the heart is moving so rapidly, segmented k-space acquisitions must be used. This allows myocardial mass, LV size, mass, shape, wall thickness, epicardial and endocardial contours and ejection fraction (EF) to be measured (5).

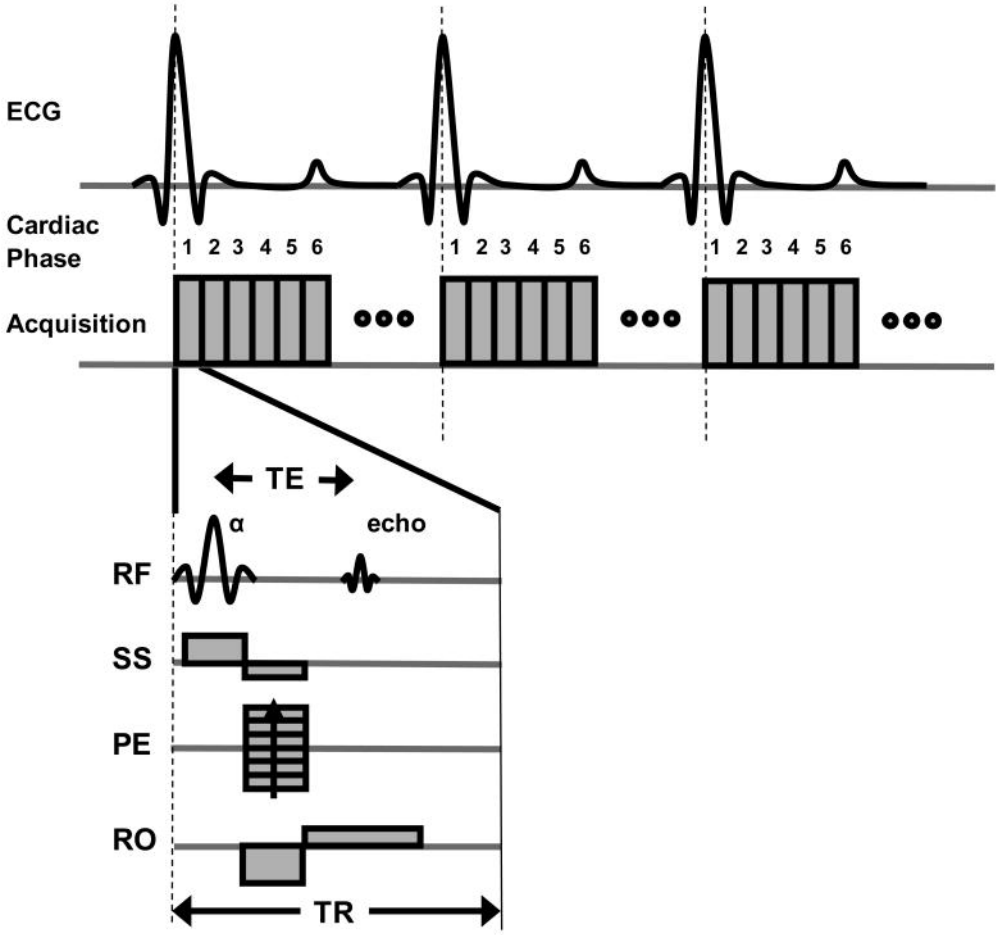

Figure 5-1. A typical ECG-gated gradient-echo (GRE) cine MRI acquisition. For the GRE sequence diagram (bottom), the RF (radiofrequency) excitation pulse (α) and echo can be seen. Each slice is acquired using slice-select (SS), phase encode (PE), and readout (RO) gradients. The echo time (TE) is the time between the RF excitation pulse and the MR signal. The repetition time (TR) is the time between excitation RF pulses and determines the temporal resolution. Individual images are acquired at different phases (e.g., 1, 2, 3…) of the cardiac cycle. The maximum number of cardiac phases that can be acquired is determined by the TR and the interval between consecutive heartbeats. The phase encoding gradient changes over multiple heartbeats to acquire a complete image. From (3), used with permission.

The standard MRI technique to assess myocardial infarct size is late gadolinium enhancement (LGE) imaging (6), which is based on an IR-prepared pulse sequence (Figure 5-2).. The diagnostic quality of this method depends on the selection of an appropriate inversion time. While this is easy to achieve at human heart rates where inversion and readout pulses can be performed within the same cardiac cycle, inversion timing becomes challenging at heart rates of >200 bpm where several cardiac cycles have to be included. Some studies in small animals have

reported adaptations of clinical IR based sequences (7, 8), or conventional T_1 weighted sequences (9, 10) to overcome some of these issues.

.

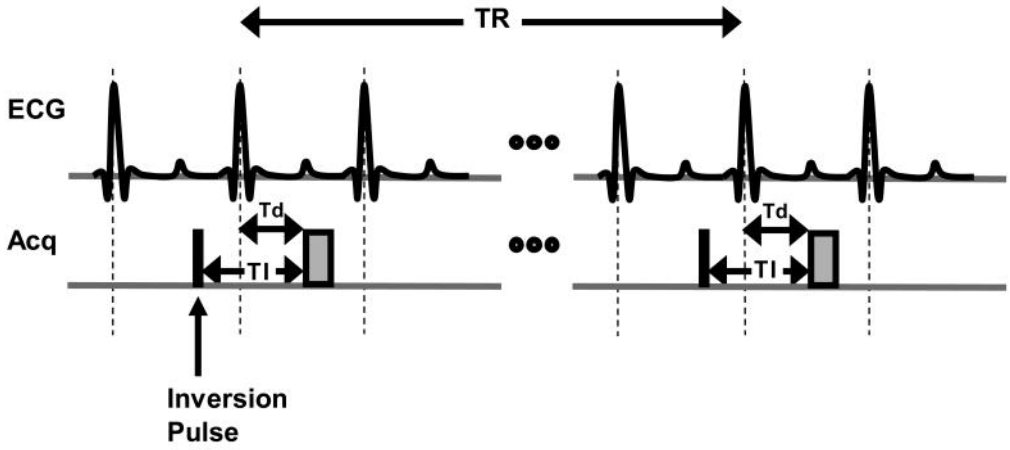

Figure 5-2. An inversion recovery (IR) spoiled gradient-echo sequence for late gadolinium enhancement (LGE) imaging. A non-selective inversion pulse (black box) is applied at an inversion time (TI) prior to the image acquisition (grey box) in mid-diastole. A long TR 2–3 times the T_1 of normal myocardium is chosen to allow sufficient recovery of the inverted magnetisation. The trigger delay Td is chosen to allow imaging in diastole, the time of cardiac motion. Because a non-selective inversion pulse is used, multi-slice image acquisition can be used to maximize imaging efficiency and allow improved coverage of the heart. From (3), used with permission.

Performing T_1 mapping in small animals is challenging as the high heart rates prevent the use of single-shot acquisitions and require segmented imaging to allow for the shorter cardiac cycles. As previously mentioned, much small animal imaging is performed at high field strength, which results in increased T_1 times. This, in turn, prolongs scan times due to the need for near-total signal recovery in IR-based methods.

In general, CMR of large animals is similar to humans, as the dimensions and heart rate are comparable. However, for reasons including cost, ethics and the availability of genetically modified animals, small animal research plays an important role in the study of cardiovascular disease. Whereas the anatomy of rats and mice is similar to that of humans, the rapid movements of the heart require high temporal resolution. Blood flow artifacts provide additional challenges to successful imaging. The small dimensions are yet another challenge, with an average size of a rat heat being about 20mm from apex to atria with a wall thickness of 2-3mm.

Small Animal Look-Locker Inversion Recovery (SALLI) is a multi-modal imaging technique that simultaneously generates cardiac T_1 maps and cine and IR-prepared images at high heart rates (11). The pulse sequence diagrams can be seen in Chapter 2 (Figure 2-13, Figure 2-14). This method allows for time-efficient assessment of T_1 properties, function, and late gadolinium enhancement from a single set of image data. SALLI generates multiple IR based LGE images with a variety of predefined steps of inversion time (TI) (e.g. 25 ms) from the image data available within the interval. This avoids the necessity of performing a pre-scan to obtain information on optimal nulling of healthy myocardium. In addition, images of corresponding heart phases from all three modalities always spatially match each other. A direct comparison of findings is then possible without the need for further image registration. T_1 mapping using SALLI has been validated (1), however the other two datasets of cine images and IR images, used to assess myocardial function and myocardial infarction following gadolinium contrast administration respectively, remain to be validated. In this study, we aimed to compare SALLI-cine MR versus conventional cine MR and SALLI-LGE against histology for assessment of LV function and myocardial viability, respectively.

5.3 Methods

All procedures and experimental protocols were approved by local authorities and performed in accordance with both the Federation of European Laboratory Animal Science Associations (FELASA) guidelines and recommendations and German federal law regarding the protection of animals.

5.3.1 Infarct Procedure

Male Sprague-Dawley rats (n=24; age, 16-22 weeks; weight, 170-340g), (Charles River, Sulzfeld, Germany) were studied. To allow the study of a range of LV function, the rats were divided into 2 groups, a group with myocardial ischemia/infarction of various duration (18) and a smaller control group (6).

The infarct operation was carried out as described in Chapter 3. Briefly, following anesthetization, intubation and ventilation, a thoracotomy was performed via fourth intercostal space. A coronary occluder was sutured in position by passing a 5-0 Ethicon prolene blue monofilament polypropylene suture around the left coronary artery (LCA). Correct positioning was confirmed by ST segment elevation and resolution on ECG, and by myocardial blanching and hypokinesia on inflation and deflation. After surgery, the animals were placed in a recovery cage for 2 hours, then returned to the animal care facility.

After a 1-week recovery period, the animals were re-anesthetized, and the coronary occluder was inflated to occlude the LCA. The duration of ischemia was 15 (6 rats), 30 (6 rats), or 60 minutes (6 rats) to provide a range of infarct sizes and left ventricular function. The control group received the same operation but did not undergo coronary occlusion.

The animals were allowed to recover, and MRI was performed 1 week after myocardial ischemia. On completion of the final MRI study, animals were euthanized and their hearts were excised. The control group comprised of rats who did not undergo myocardial ischemia who were imaged once.

5.3.2 MRI Protocol

Experiments were carried out with a whole-body 3.0-T MR unit (Intera and Achieva; Philips Healthcare, Best, the Netherlands) equipped with a dedicated coil for rats. After generation of

survey images and of a long-axis set of cine images, a stack of left ventricular (LV) short-axis cine images was acquired (phases, 30; repetition time (TR), 6.8 ms; echo time (TE), 4.60 ms; flip angle, 15°; field of view, 80×64 mm; acquired voxel size, 0.4×0.4×1.5 mm; number of signal averages, 4; slices, 7; slice thickness 1.5 mm).

Short axis SALLI MR imaging was performed in the identical 7 short axis slices from apex to base both before and after an injection of 0.3 mmol/kg of gadolinium contrast medium (gadobutrol [Gadovist]; Bayer-Schering AG, Berlin, Germany). Typical SALLI parameters were: acquisition duration, 4000 ms; relaxation duration, 4000 ms; phases, 4; flip angle, 10°; field of view, 56×56 mm; acquired voxel size, 0.6×0.6×2.4 mm; TR, 7.6 ms; TE, 3.1 ms; number of signal averages, 4; total acquisition time, 5 minutes 40 seconds.

5.3.3 Image Analysis

Images were reconstructed using a customized reconstruction framework (ReconFrame; Gyrotools, Zurich, Switzerland) implemented with Matlab software (MathWorks, Natick, USA). Images were transferred to a CMR analysis software package (CMR42 version 4.0; Circle Cardiovascular Imaging Inc, Calgary, Alberta, Canada) and analyzed. For each of the sets of data, the image quality was visually assessed (good, no artifacts = 1, minor artifacts = 2, non-evaluable, major artifacts = 3). Endocardial contours were manually traced in systole and diastole to allow calculation of LV ejection fraction from both cine MR and SALLI datasets. To evaluate if the presence of contrast agents altered image quality or LV function measurement, a subset of 10 animals had left ventricular function measured in both pre- and post-contrast SALLI images.

Infarct size was calculated from the SALLI-LGE dataset. Firstly, the optimum TI was manually selected. On the selected images, subepicardial and subendocardial contours of the LV myocardium were manually traced. The infarct volume was then manually traced. Total infarcted area was expressed as percentage of the LV volume, given by the sum of the volume of high signal intensity on LGE (necrosis/scar) for all slices divided by the sum of the LV myocardial cross-sectional volumes (%LV).

We chose to quote contrast resolution to give a comparative estimate of contrast between the blood, infarcted and remote myocardium, as there are a number of challenges with calculating

SNR (12). Contrast resolution is defined as CR = (SA-SB)/(SA+SB). The image with optimal TI was defined visually as the value at which the signal intensity (SI) of the viable myocardium was nulled. Signal intensities in the LV blood pool, healthy and infarcted myocardium were measured in 3 consecutive slices containing both infarcted and healthy myocardium using Osirix (Pixmeo SARL, Bernex Switzerland). For each slice, an elliptical region of interest (ROI) was selected to include the largest continuous area of enhanced myocardium possible; a second ROI of the same size was placed in an area of remote healthy myocardium, typically within the septum.

5.3.4 Histology

Staining was performed to assess the presence and extent of myocardial infarction (13). Animals were euthanized by exsanguination following an overdose of isoflurane anesthetic. The heart, with occluder attached, was swiftly removed. The coronary artery was occluded in the same position by re-inflating the occluder balloon. Evan's blue dye (2%, 0.6ml) was injected retrogradely into the ascending aorta to delineate the area at risk. The heart was cut parallel to the atrio-ventricular groove in 1-mm thick slices. These were then incubated in 1% triphenyltetrazolium chloride (TTC) at 37°C for 20 min followed by 90 minutes in formalin. Viable myocardium stains red and necrotic area remains unstained by TTC. The slices were photographed using a color camera (Canon Powershot G12). The images were analyzed using ImageJ (Rasband, W.S., ImageJ, National Institutes of Health, Bethesda, Maryland, USA). The area stained blue was defined as the remote area and the unstained area as the area at risk (AAR). The AAR was then divided into infarction (stained white), viable tissue with AAR (stained red), and remote tissue (stained blue).

5.3.5 Statistical Analysis

Continuous variables are expressed as mean ± standard deviation (SD). Normal distribution of the infarct size data was confirmed using by Normal plots and Shapiro-Wilk testing. A line of identity on a scattergram was drawn between each technique to allow a visual assessment of agreement. The Bland– Altman limits of agreement were also determined, with the difference in EF between techniques established for each subject along with the range of values within which 95% of the differences were expected to lie (14). Results are presented as mean ± standard deviation. The mean differences in EF and infarction size were calculated between each

technique, and Student's t-test was used to determine statistical significance. All tests were two-tailed; $p<0.05$ was considered significant.

5.4 Results

5.4.1 Cine Assessment - SALLI Cine MR versus Cine MR

Data was available for 24 rats. Average Heart rate over the entire exam was 330 (± 30). Representative images can be seen in Figure 5-3, and image quality was good or adequate in all cases. Image quality was comparable ($p=0.56$) between cine-MR (1.2 ± 0.4) and SALLI (1.4 ± 0.5). Left ventricular function as measured by both methods was very similar. The EF by cine MR was 60.8 ± 12% and by SALLI it was 59.8 ± 12%. There was good correlation between both methods of measurement ($r = 0.93$). No significant difference was found between the methods of measurement (mean difference -0.5 ± 3%, $p=0.42$). The measured EF in both techniques is demonstrated in Figure 5-4, which shows a narrow scatter around the line of agreement.

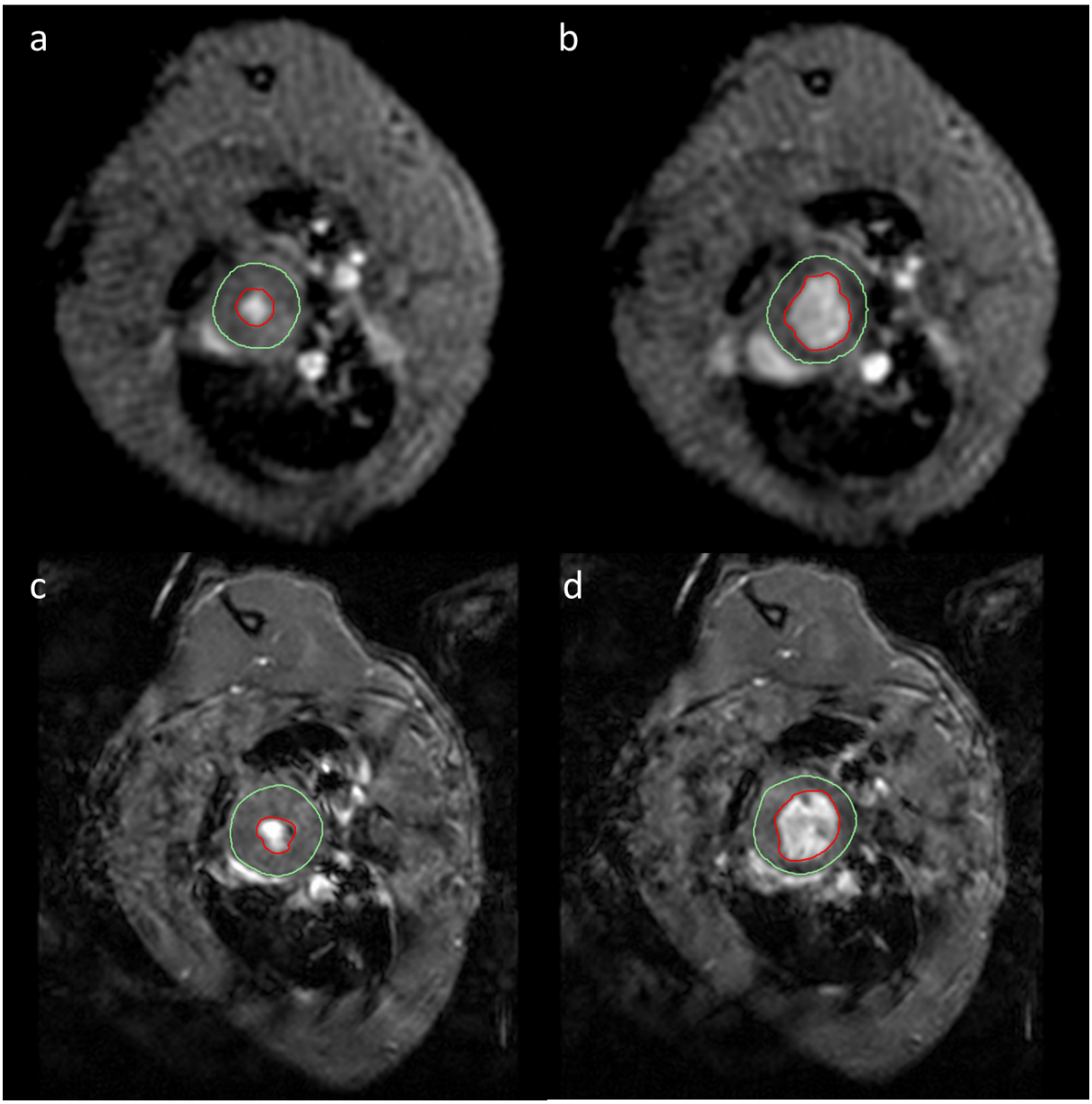

Figure 5-3. Comparison of SALLI-cine images in systole (a) and diastole (b) with Cine MR images in systole (c) and diastole (d)

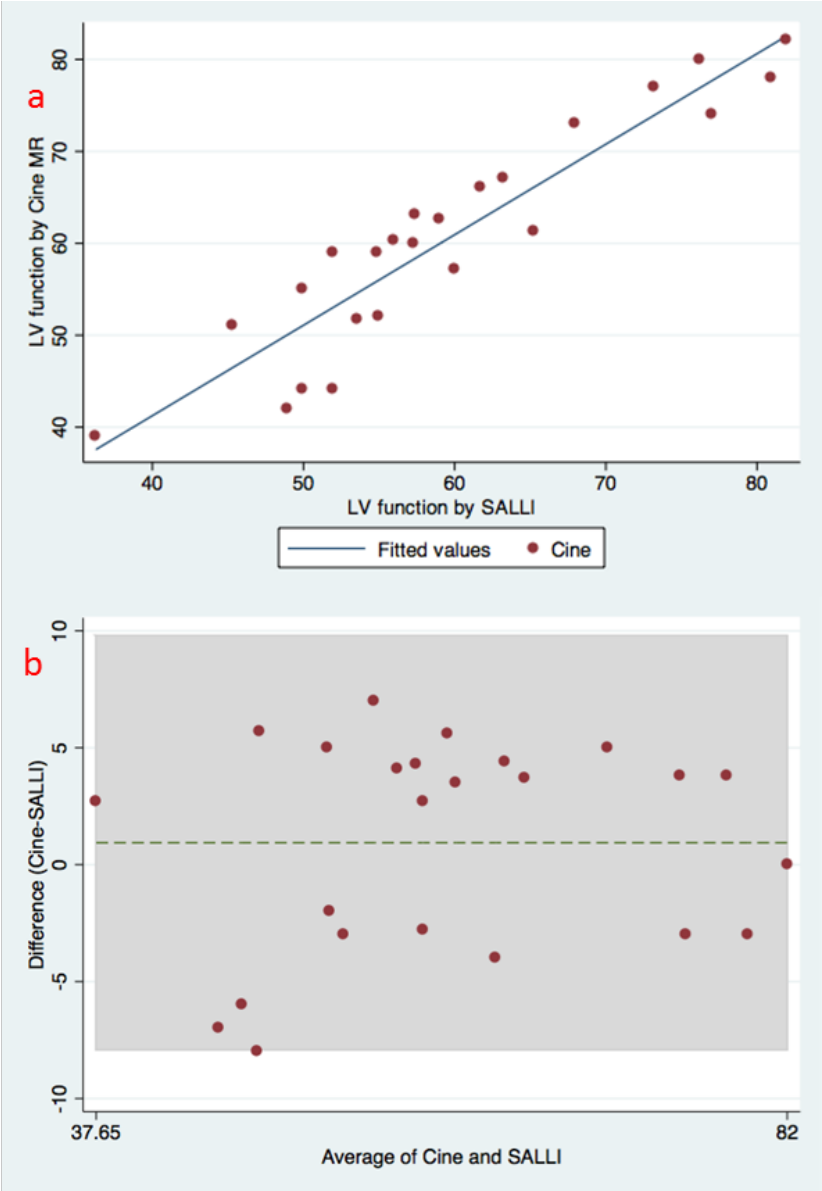

Figure 5-4. (a) Scatter plots with line of agreement and (b) Bland–Altman plots for comparisons between techniques.

Table 5-1. The Mean Differences and Standard Deviation (SD) for Ejection Fraction between each Technique, Together with the Student's t-test. The Bland–Altman Limits of Agreement are also Illustrated and Represent Ejection Fraction (%)

	Mean Difference ± SD (%)	p-value	Bland–Altman Limits (%)	Range of Bland–Altman Limits (%)
Cine – SALLI	0.9 ± 5	0.48	- 3.6, 5.4	38 - 82

Image quality was similar between the pre- and post-contrast SALLI-cine images, and there was no significant difference in the measured ejection fraction (p=0.63) (Figure 5-5).

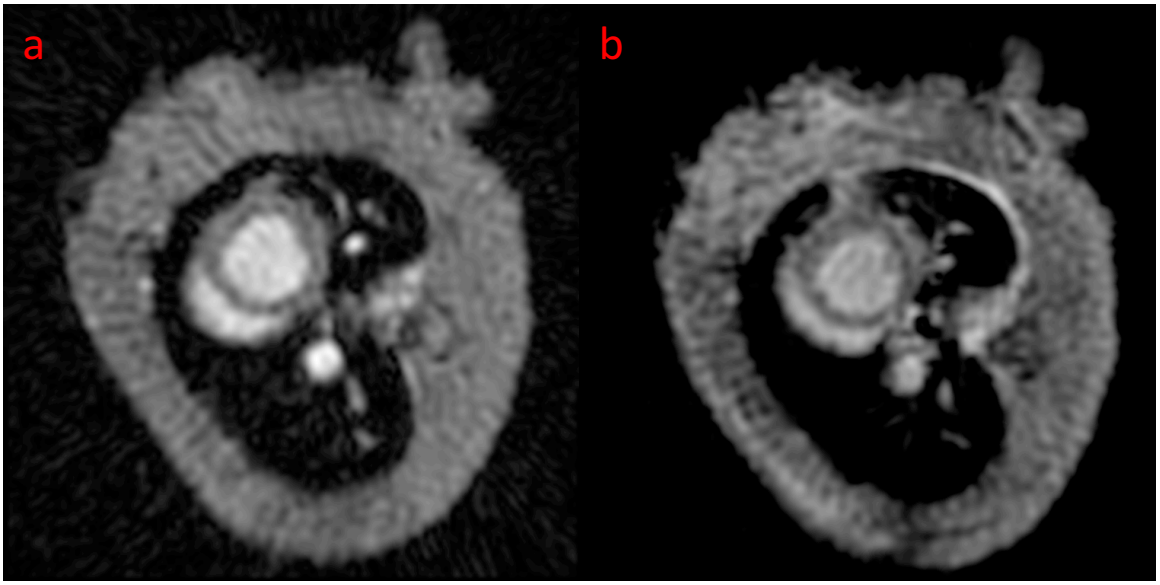

Figure 5-5. Comparison of (a) pre- and (b) post-contrast SALLI-cine images.

5.4.2 Infarct Size Assessment - SALLI -LGE versus Histology

Data was available for 24 Rats. Image quality was good or adequate in all cases (1.3 ± 0.5). None of the control rats had infarction detectable by SALLI-LGE. Infarcts were typically transmural as can be seen in Figure 5-6.

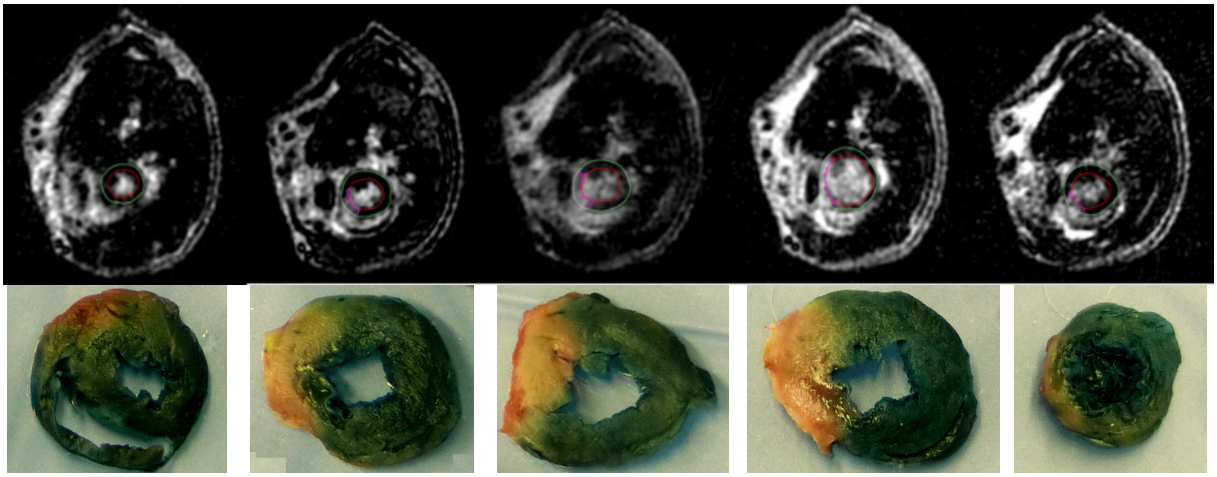

Figure 5-6. SALLI-LGE images and Evan's Blue/TTC stained slices of a heart that underwent 60 minutes of myocardial ischemia. The Infarct is stained white while the remote myocardium is stained blue.

Infarct size was comparable between both methods, with infarct size by staining 23.5 ± 18% and by SALLI-LGE 21.9 ± 18%. No significant difference was found between the methods of measurement (mean difference 1.05 ± 5%, p=0.28). There was a good correlation between both methods of measurement (r = 0.95). Both staining and SALLI-LGE of which demonstrate a narrow scatter around the line of agreement Figure 5-7.

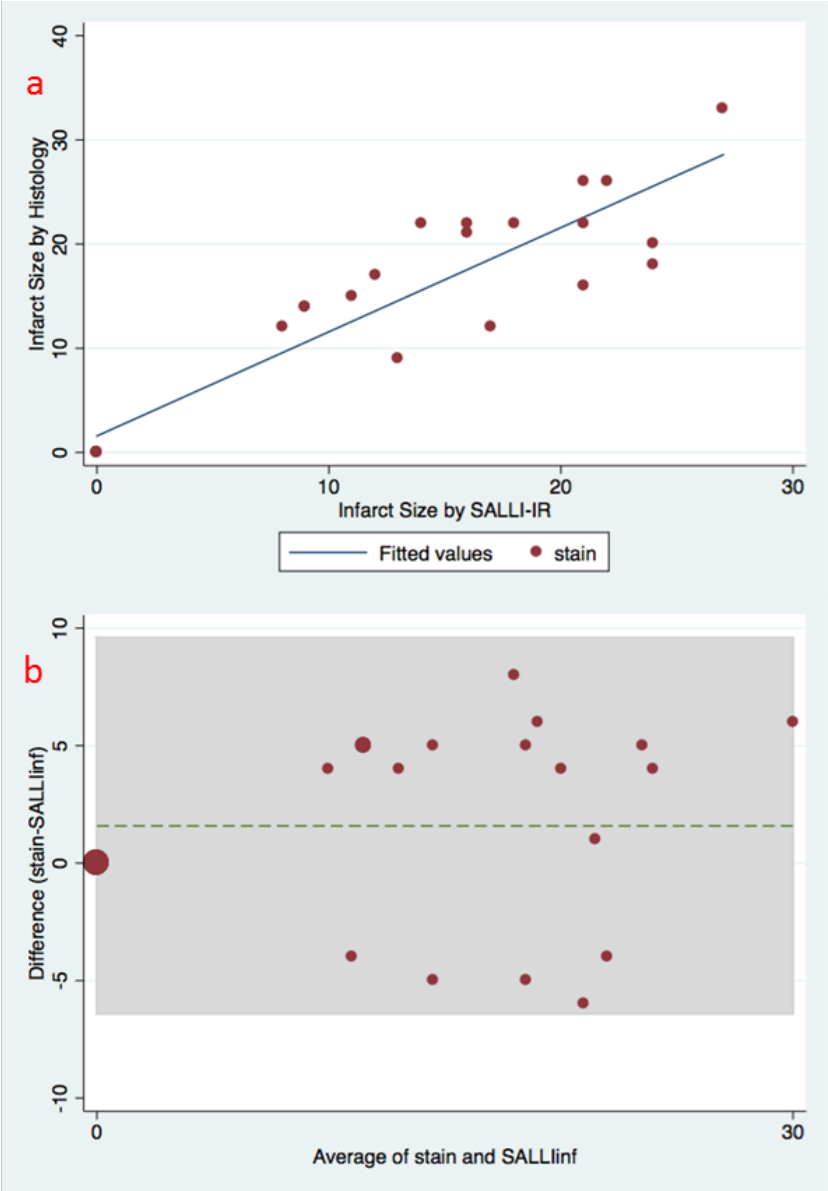

Figure 5-7. (a) Scatter plots with line of agreement and (b) Bland–Altman plots for comparisons between techniques.

Table 5-2. The Mean Differences and Standard Deviation (SD) for Infarct Size Between Each Technique, Together with the Student's t-test. The Bland–Altman Limits of Agreement Are Also Illustrated and Represent Infarct Size (%)

	Mean Difference ± SD (%)	p-value	Bland–Altman Limits (%)	Range of Bland–Altman Limits (%)
Staining – SALLI	1.6 ± 4	0.296	-2.5, 9.8	0 – 30

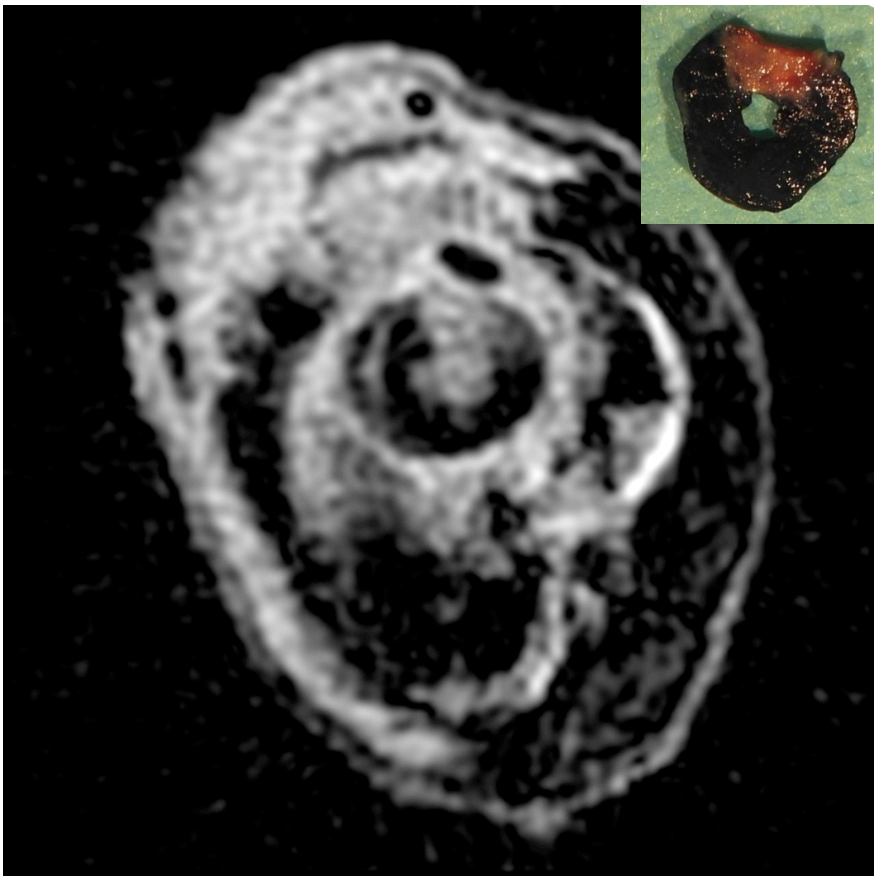

Figure 5-8. Comparison of infarct size by staining (upper right) and by SALLI-LGE.

5.4.3 Contrast Resolution

Contrast resolution between infarcted and remote myocardium was measured in SALLI-LGE images as 53.2 ± 13%. Contrast resolution between infarct and blood pool was lower at 15.1 ± 11 % in rats. A sample image can be seen in Figure 5-8. An advantage of SALLI is that the LV borders can be delineated from the Cine images in the same phase, and then copied to the LGE image to allow accurate measurement of infarct size and LV volumes.

5.5 Discussion

In a model of myocardial infarction, SALLI imaging was able to accurately assess LV function and characterise myocardial infarction in a time efficient fashion. LV systolic function was comparable to standard cine MRI across a wide range of LV function, from normal to severe LV impairment. SALLI-LGE was able to detect even small myocardial infarctions, and correctly identified normal myocardial tissue in control animals.

Small animal contrast imaging has important differences relative to clinical scanning, resulting from the high heart rate of the animals. Diastole is much shorter, 20-30 ms, which allows fewer

lines of k space to be acquired per inversion. However, to allow time for adequate relaxation, the TR should be at least 2-3 times the T_1 of myocardium (approx. 1100 ms at 3 T). The combination of long TR and multiple acquisitions could result in prolonged examination times (3). Modifications of the IR FLASH method have been proposed, with a different number of echoes (typically 4-16) acquired after each pulse and various gating strategies applied. These include magnetisation-prepared FLASH (7) for 2D imaging and a 3D sequence (15). An alternative to the IR method includes the Cine FLASH method, proposed by a number of groups (9, 16). This method offers the advantage of obtaining both functional and LGE data in one acquisition.

SALLI offers the advantage of functional, LGE and T_1 mapping in a single acquisition. To shorten acquisition duration, SALLI uses temporal undersampling and radial acquisition. However, this radial sampling leads to some loss of resolution in the fine details, as the periphery of k-space is more sparsely sampled. Using a clinical 3 T MR system with high-performance gradient system, individual slices could be acquired in 5-6 minutes, with T_1 mapping, cine and LGE images of the whole heart in 40 minutes approximately. Acquisition times could be further reduced if a dedicated preclinical MR system with a faster gradient system were used.

A number of methods for small animal MRI imaging have been developed on preclinical systems, offering very rapid cine and inversion-recovery LGE imaging at high resolutions. These include 2D multislice imaging providing whole heart functional assessment in 6 minutes on a pre-clinical 7T MRI system (8, 17). The use of multislice sampling allows the use of larger flip angles, which then results in higher signal-to-noise ratios. The use of a 3D sequence can provide even greater levels of SNR efficiency, offering rapid functional imaging (18) and whole heart T_1 mapping (19).

SALLI generates multiple IR images with different TIs. As most small animal LGE sequences take a number of minutes to generate each image, the optimal TI will vary following contrast injection for each slice. SALLI has the advantage of allowing the image with the best contrast to be selected for analysis, without the necessity to pre-select or change the selected TI. As images with multiple TIs are reconstructed, a Look-Locker sequence is not required to detemine optimal inversion time, offering potential time savings. However, a number of studies have found that at high field strength using higher doses of gadolinium contrast agent, the optimal TI is less important, and the imaging can be simply triggered every second or third heartbeat (8, 16). Contrast resolution using SALLI-LGE was adequate to accurately define myocardial infarction.

The value of 50.1% is comparable to the contrast resolution in other studies, which used higher field strengths and higher doses of contrast agent (8).

As SALLI is a segmented image sequence, excellent ECG triggering and stability of the heart rate are required to allow image acquisition. In animals with large infarctions, there may be loss of ECG R-wave height, leading to challenges with recognition of the R-wave for triggering. Rigorous preparation of the electrical contact points of the ECG is required to minimize these issues. A dedicated small animal ECG system could allow for more sensitive ECG acquisition, or a self-gated sequence could overcome these difficulties.

In contrast with some T_1 mapping approaches, where the relaxation curve is influenced at intervals determined by individual heart rate, there is no heart rate dependency expected for T_1 values obtained with SALLI since there is a permanent readout of predefined duration (4000 ms in our example) that does not change with heart rate.

SALLI generates three types of images from one image data set. Not only is this potentially time saving, the images of corresponding heart phases from all three modalities will spatially match each other. A direct comparison of findings is then possible without the need for further image registration. Imaging parameters can be adjusted to optimize the acquisition for the specific needs of the investigator. Acquisition duration (AD) and relaxation duration (RD) can be adjusted to the maximum expected T_1 of the tissue of interest (e.g. 600 ms for post-contrast myocardium at 3 Tesla); b) temporal undersampling or low numbers of cardiac phases can be used where cine data is of less interest; c) increasing the NSA is helpful to increase SNR. For example, for the in-vivo images of the animal with myocardial infarction it would be possible to reduce the duration of post-contrast imaging by temporal undersampling or reducing the number of cardiac phases as the functional information is already available from the pre-contrast image. Increasing the number of signal averages would would allow improved spatial resolution. The imaging parameters could also be optimized for situations where myocardial changes are global rather than focal, such as in myocarditis. SALLI might be used to serially study acute myocardial injury in vivo in small animals, enabling parallel assessment of myocardial oedema and function and reducing the number of animals necessary for longitudinal experiments.

5.5.1 Study Limitations

SALLI-LGE was not compared with conventional IR methods for infarct quantification. It was felt that quantification should be against the reference standard of histology, rather than other methods of LGE imaging.

The sequence used has a resolution of 0.60 x 0.60 mm. This is reasonable resolution for rat myocardium (2-3 mm thick), but may miss very small or subendocardial infarcts. Higher spatial resolution could be achieved by use of a preclinical high-field MR system.

5.6 Conclusions

SALLI provides an acceptable alternative to conventional cine MR imaging and LGE methods for small animals. Both methods provided very similar results across a range of ventricular function and infarct size. Image quality was similar between both methods and interpretable in all cases. In addition, SALLI generates multimodal (in this case, cine MR, T_1 maps and Inversion-Recovery prepared) images from the same dataset, with the advantage not only of potential time saving, but also of the comparison of findings without the need for further image registration.

The multimodal approach of SALLI could speed up and facilitate the comprehensive and quantitative assessment of myocardial injury in small animal models of myocardial disease.

5.7 References

(1) Messroghli, D.R., Nordmeyer, S., Dietrich, T., Dirsch, O., Kaschina, E., Savvatis, K., D, O h.-Ici, Klein, C., Berger, F., and Kuehne, T. (2011). Assessment of diffuse myocardial fibrosis in rats using small-animal Look-Locker inversion recovery T1 mapping. *Circ Cardiovasc Imaging* **4**(6), 636-40.

(2) Kim, H.W., Farzaneh-Far, A., and Kim, R.J. (2009). Cardiovascular magnetic resonance in patients with myocardial infarction: current and emerging applications. *J. Am. Coll. Cardiol.* **55**(1), 1-16.

(3) Gilson, W.D., and Kraitchman, D.L. (2007). Cardiac magnetic resonance imaging in small rodents using clinical 1.5 T and 3.0 T scanners. *Methods* **43**(1), 35-45.

(4) Kober, F., Iltis, I., Cozzone, P.J., and Bernard, M. (2004). Cine-MRI assessment of cardiac function in mice anesthetized with ketamine/xylazine and isoflurane. *MAGMA* **17**(3-6), 157-61.

(5) Heijman, E., Aben, J.P., Penners, C., Niessen, P., Guillaume, R., van Eys, G., Nicolay, K., and Strijkers, G.J. (2008). Evaluation of manual and automatic segmentation of the mouse heart from CINE MR images. *J. Magn. Reson. Imaging* **27**(1), 86-93.

(6) Kim, R.J., Wu, E., Rafael, A., Chen, E.L., Parker, M.A., Simonetti, O., Klocke, F.J., Bonow, R.O., and Judd, R.M. (2000). The use of contrast-enhanced magnetic resonance imaging to identify reversible myocardial dysfunction. *N. Engl. J. Med.* **343**(20), 1445-53.

(7) Chapon, C., Herlihy, A.H., and Bhakoo, K.K. (2008). Assessment of myocardial infarction in mice by late gadolinium enhancement MR imaging using an inversion recovery pulse sequence at 9.4T. *J. Cardiovasc. Magn. Reson.* **10**, 6.

(8) Price, A.N., Cheung, K.K., Lim, S.Y., Yellon, D.M., Hausenloy, D.J., and Lythgoe, M.F. (2011). Rapid assessment of myocardial infarct size in rodents using multi-slice inversion recovery late gadolinium enhancement CMR at 9.4T. *J. Cardiovasc. Magn. Reson.* **13**, 44.

(9) Thomas, D., Dumont, C., Pickup, S., Misselwitz, B., Zhou, R., Horowitz, J., and Ferrari, V.A. (2006). T1-weighted cine FLASH is superior to IR imaging of post-infarction myocardial viability at 4.7T. *J. Cardiovasc. Magn. Reson.* **8**(2), 345-52.

(10) Yang, Z., Berr, S.S., Gilson, W.D., Toufektsian, M.C., and French, B.A. (2004). Simultaneous evaluation of infarct size and cardiac function in intact mice by contrast-

enhanced cardiac magnetic resonance imaging reveals contractile dysfunction in noninfarcted regions early after myocardial infarction. *Circulation* **109**(9), 1161-7.

(11) Messroghli, D.R., Nordmeyer, S., Buehrer, M., Kozerke, S., Dietrich, T., Kaschina, E., Becher, P.M., Hucko, T., Berger, F., Klein, C.*, et al.* (2011). Small animal Look-Locker inversion recovery (SALLI) for simultaneous generation of cardiac T1 maps and cine and inversion recovery-prepared images at high heart rates: initial experience. *Radiology* **261**(1), 258-65.

(12) Kellman, P., and McVeigh, E.R. (2005). Image reconstruction in SNR units: a general method for SNR measurement. *Magn. Reson. Med.* **54**(6), 1439-47.

(13) Bohl, S., Medway, D.J., Schulz-Menger, J., Schneider, J.E., Neubauer, S., and Lygate, C.A. (2009). Refined approach for quantification of in vivo ischemia-reperfusion injury in the mouse heart. *Am. J. Physiol. Heart Circ. Physiol.* **297**(6), H2054-8.

(14) Bland, J.M., and Altman, D.G. (1986). Statistical methods for assessing agreement between two methods of clinical measurement. *Lancet* **1**(8476), 307-10.

(15) Bohl, S., Lygate, C.A., Barnes, H., Medway, D., Stork, L.A., Schulz-Menger, J., Neubauer, S., and Schneider, J.E. (2009). Advanced methods for quantification of infarct size in mice using three-dimensional high-field late gadolinium enhancement MRI. *Am. J. Physiol. Heart Circ. Physiol.* **296**(4), H1200-8.

(16) Protti, A., Sirker, A., Shah, A.M., and Botnar, R. (2010). Late gadolinium enhancement of acute myocardial infarction in mice at 7T: cine-FLASH versus inversion recovery. *J. Magn. Reson. Imaging* **32**(4), 878-86.

(17) Buonincontri, G., Methner, C., Krieg, T., Carpenter, T.A., and Sawiak, S.J. (2013). A fast protocol for infarct quantification in mice. *J. Magn. Reson. Imaging* **38**(2), 468-73.

(18) Nieman, B.J., Szulc, K.U., and Turnbull, D.H. (2009). Three-dimensional, in vivo MRI with self-gating and image coregistration in the mouse. *Magn. Reson. Med.* **61**(5), 1148-57.

(19) Coolen, B.F., Geelen, T., Paulis, L.E., Nauerth, A., Nicolay, K., and Strijkers, G.J. (2011). Three-dimensional T1 mapping of the mouse heart using variable flip angle steady-state MR imaging. *NMR Biomed.* **24**(2), 154-62.

Chapter 6 T_1 Measurement in Acute Myocardial Ischemia/Reperfusion

6.1 Abstract

Myocardial ischemia causes local oedema, leading to prolongation of both T_1 and T_2. In clinical MRI, T2-weighted techniques are commonly used to visualize myocardial oedema. With standard MRI techniques, it is not possible to detect differences in oedema formation due to different reperfusion schemes such as preconditioning. Thus, these techniques cannot be used to compare the effects of reperfusion strategies. The aims were to study the acute T_1 changes in-vivo in a novel closed chest animal model of myocardial ischemia/reperfusion using T_1 mapping and to test if this parametric approach could provide additional diagnostic information as compared to conventional MRI (1).

Five groups of rats had an inflatable balloon coronary occluder surgically inserted via thoracotomy. They were allowed to recover for seven days. MRI was performed to obtain a baseline measurement of ventricular function. T_1 mapping was performed using the Small-Animal Look-Locker Inversion Recovery (SALLI) technique. Short axis SALLI MR imaging was performed in the mid-ventricle distal to the occluder, with SALLI parameters as previously described. Without removing the animals from the scanner, the left coronary artery was occluded for 15, 30 or 60 minutes. Two groups of animals underwent three cycles of 5 minutes of preconditioning before 30 and 60 minutes of ischemia. Myocardial T_1 measurements were repeated at 15-minute intervals during the experiment, throughout ischemia and the 90 minutes of reperfusion. MRI was performed on a whole-body 3.0-T MR unit with a dedicated rat coil.

Myocardial T_1 increased in the area-at-risk (AAR) within the first 15 minutes of ischemia. T_1 values increased slightly more with longer periods of ischemia but did not change with myocardial reperfusion. Preconditioning led to a more gradual and lesser increase in myocardial T_1 in the AAR. Changes in T_1 persisted at three and seven days.

Myocardial T_1 mapping can be used to study the changes in myocardial T_1 in real-time in a model of ischemia/reperfusion. Changes in myocardial T_1, likely reflecting myocardial water content, occur early following the onset of myocardial ischemia and values remain elevated for at least seven days following ischemia. Preconditioning appears to lead to less myocardial oedema,

which may explain some of its protective effects in myocardial ischemia. T_1 mapping might provide an in-vivo imaging marker for monitoring the quality of myocardial reperfusion.

6.2 Introduction

In the myocardium, metabolic changes occur in the seconds following coronary occlusion. Anaerobic glycolysis becomes the sole source of high-energy phosphates, with lactate and protons as the principal end products (2). As described in more detail in chapter 6, myocardial cells have a low Adenosine Tri-Phosphate (ATP) content. Anaerobic glycolysis is unable to keep up with the metabolic demands of the cell (3). Intracellular ATP concentration decreases, and there is increased lactate production and a decrease in pH. A markedly decreased pH inhibits glycolysis and interferes with the residual metabolic pathways in the cell.

The lack of ATP results in cessation of contraction. If ischemia is prolonged, the cell is unable to provide energy to maintain homeostasis, eventually leading to cellular bulging (4). In an attempt to control pH, the Na^+/H^+ exchanger in myocardial cells excrete excess H^+ ions, leading to a Na^+ influx (5), followed by Cl^- and water. These factors combine with the failure of ATP-dependent cellular pumps, ATPases, such as the Na^+/K^+ ATPase, ATP-dependent Ca^{2+} reuptake, and active Ca^{2+} excretion. This results in Ca^{2+} overload, and eventually the opening of the mitochondrial permeability transition pore (MPTP). This pore opens in response to increased levels of calcium and the reactive oxygen species generated by the ischemic cell. The combination of these and other changes lead to increases in cell membrane permeability, with disruption of intracellular electrolytes. The cell swells with the final event, the breakdown of the cellular wall.

Reperfusion is the obvious treatment for coronary artery occlusion. Rapid reperfusion, either by thrombolysis or percutaneous revascularization, has been shown to reduce infarct size, and preserve left ventricular function, leading to improved survival (6, 7). However, the effects of reperfusion are complex. The limitation in ischemic injury by restoration of oxygen supply and normalization of pH are countered, in part, by reperfusion injury. Reperfusion injury was first described over 50 years ago (8) and is clinically manifested by arrhythmia, microvascular dysfunction, myocardial stunning, and myocyte death. The rapid normalisation of the pH outside the cell causes an extreme H^+ gradient, leading to Na^+/H^+ exchange, and a further Na^+ influx. This gradient also leads the passive Na^+/ Ca^{2+}exchanger to excrete Na^+ for Ca^{2+}, leading to further Ca^{2+} overload. The rapid changes of pH within the cell result in the opening of the MPTP, causing the mitochondria to swell and ultimately rupture. Mitochondrial rupture results in ATP

hydrolysis rather than production. The release of mitochondrial proteins and lack of ATP increase the likelihood of cell death.

The acute injury described above can ultimately lead to various modes of cell death, including both necrosis and apoptosis. Necrosis is the predominant form of cell death in acute myocardial ischemia and is characterised by cellular swelling of the cell and its organelles, and the final breakdown of the cell membrane (9). Apoptosis is usually triggered by intracellular Ca^{2+} overload, leading to the release of apoptosis-inducing factor and ultimately to irreversible cellular dysfunction. Ca^{2+} overload also triggers H^{+} influx into the mitochondria, resulting in mitochondrial swelling and apoptotic changes (10). The breakdown of cell membranes and release of intracellular components leads to activation of an inflammatory response, which can lead to damage to neighbouring cells. This inflammatory response is accelerated and increased on myocardial reperfusion (11).

In 1996, it was found that short bouts of ischemia and reperfusion (ischemic preconditioning) prior to prolonged myocardial ischemia (index ischemia) could reduce the size of myocardial (12). This original report of a reduction in myocardial infarct size in dogs was reproduced in other species, from rats (13) to pigs (14). It is of course not possible to perform ischemic preconditioning experiments in humans, however, both percutaneous coronary intervention (PCI) and bypass surgery involve brief periods of myocardial ischemia. These have been used to study the effects of preconditioning and demonstrated a reduction in markers of myocardial damage (15) (16). The exact mechanism of the benefits remains to be elucidated. Indeed, whether preconditioning improves clinical outcomes has yet to be determined.

In summary, myocardial ischemia-reperfusion leads to cellular electrolyte alterations, myocardial cell swelling and inflammation. T_1 mapping is a powerful way to study changes in myocardial water content. As described in Chapter 3, myocardial "native T_1" increases with myocardial water content or oedema. Quantitative in vivo measurement of water content using MRI is based on the proportionality of the MR signal to the number of protons in an image volume, which is again proportional to the water content in that volume.

The aim of the present study was to assess in-vivo the sequential changes following myocardial ischemia and reperfusion. The closed-chest model developed in chapter 3 was used to study

dynamic changes in myocardial T_1. Measurements were repeated to study the development of myocardial oedema during myocardial ischemia of varying durations and myocardial reperfusion. Imaging was repeated at 1 week following ischemia/reperfusion. Data were correlated with regional function using cine MR imaging and to the AAR as determined by Evan's blue staining.

6.3 Methods

All procedures and experimental protocols were performed in accordance with the Federation of European Laboratory Animal Science Associations (FELASA) guidelines and recommendations, German federal law regarding the protection of animals and were approved by local authorities.

6.3.1 Surgery

The closed-chest model of myocardial ischemia/reperfusion as described in Chapter 3 was used to avoid the surgical trauma and inflammation associated with open-chest models, and to allow ischemia/reperfusion to be induced with the animal in the bore of the MRI.

6.3.2 Myocardial Ischemia Protocol

Rats were anaesthetized with an initial dose of 4% isoflurane in an air/oxygen (4:1) mixture. A small incision was performed to locate the tip of the occluder. The tip was then attached to a 20G plastic cannula and extension tubing. The balloon could then be inflated and deflated without moving the animal in the bore of the scanner. One 26G iv cannula was placed in the tail to allow continuous potassium infusion to minimise cardiac arrhythmia (17).

Anaesthesia was maintained using 1-2% isoflurane in an air/oxygen (4:1) mixture during the imaging. Body temperature was maintained at 37-38 °C using heating mats. The animals were positioned on a dedicated animal bed and positioned within the MRI coil.

6.3.3 Imaging Protocol

All MRI studies were performed on a 3-T clinical MRI system (Intera and Achieva, Philips Healthcare, Best, The Netherlands) equipped with a dedicated solenoid coil for rats. Animals were positioned in the coil head first and supine with ECG electrodes placed on the rats' feet. Anaesthesia was maintained throughout the examination via inhalation of 1-2% isoflurane.

Using a long-axis set of cine images (2-chamber view and 4-chamber view) and a left ventricular (LV) cine short-axis stack (phases, 30; repetition time (TR), 6.8 ms; echo time (TE), 4.60 ms; flip angle, 15°; field of view, 80×64 mm; acquired voxel size, 0.4×0.4×1.5 mm; number of signal averages, 4; slices, 7; slice thickness 1.5 mm) the following parameters were assessed: LV ejection fraction, end-diastolic volume, end-systolic volume and cardiac output.

After functional analysis, T_1 parameters were measured before and after gadolinium contrast injection (gadobutrol [Gadovist]; Bayer-Schering AG, Berlin, Germany, 0.3 mmol/kg) at the same location in a mid-cavity short-axis slice using Small Animal Look-Locker Inversion Recovery (SALLI; acquisition duration, 4000 ms; relaxation duration, 4000 ms; phases, 4; flip angle, 10°; field of view, 56×56 mm; acquired voxel size, 0.6×0.6×2.4 mm; TR, 7.6 ms; TE, 3.1 ms; number of signal averages, 4; total acquisition time, 5 minutes 40 seconds).

6.3.4 Coronary Occlusion Protocol

Animals were divided into five groups, 15, 30 or 60 minutes of ischemia, and 30 and 60 minutes of ischemia proceeded by three cycles of 5 minutes of myocardial preconditioning. After baseline measurement, the left coronary artery (LCA) was occluded by inflating the balloon of the occluder with 0.2 ml of water and closing the 3-way stopcock. Ischemia was confirmed by ECG changes and localised hypokinesia on cine MR imaging. For the preconditioning groups, the artery was occluded for 5 minutes, followed by 5 minutes of reperfusion, which was repeated for three cycles. The LCA was then re-occluded, and after 15, 30 or 60 minutes of ischemia, the occluder balloon was deflated. SALLI was performed throughout, at baseline, and every 15 minutes during myocardial ischemia and for 90 minutes reperfusion following the reopening of the LCA. Cine MR imaging was repeated at the end of the protocol. To confirm successful reperfusion and estimate myocardial injury, SALLI-late gadolinium enhancement (SALLI-LGE) imaging was performed at the end of the protocol.

Animals were re-imaged at three days and one week following ischemia/reperfusion including cine imaging and whole heart SALLI imaging for repeated T_1 mapping and LGE imaging, as described above. The overall experimental protocol is illustrated in Figure 6-1.

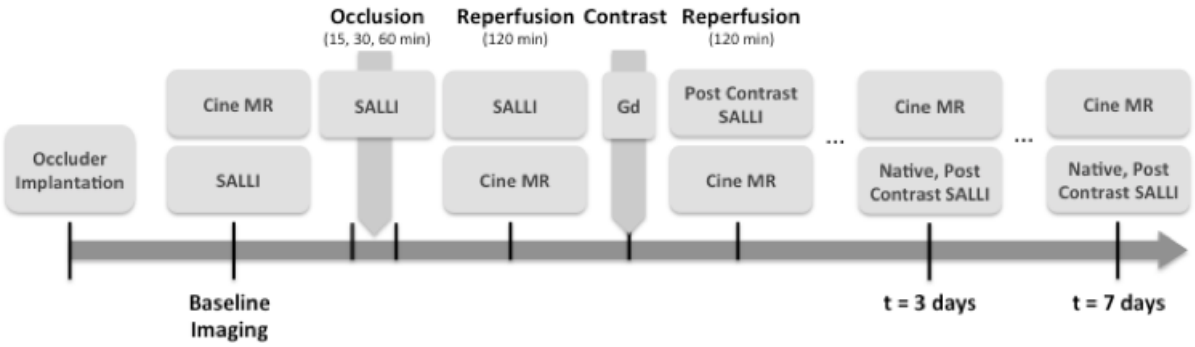

Figure 6-1. Outline of Experimental Protocol

6.3.5 Image Processing

Native (pre-contrast) and post-contrast T_1 values were measured in the area at risk (AAR), the remote zone (typically the interventricular septum) and the blood pool (left ventricular cavity) from the SALLI T_1 maps using Osirix v6.0 (Pixmeo SARL, Bernex, Switzerland) (18). The AAR was defined from the myocardial staining in the mid slice of the left ventricle. LV functional parameters were analysed in a CMR analysis software package (CMR42 version 3.4.1; Circle Cardiovascular Imaging Inc, Calgary, Alberta, Canada).

6.3.6 Staining

Staining was performed to confirm the presence of potential infarction and to assess the area-at-risk in all animals similarly to methods previously described in Chapter 3 (19). Animals were euthanised by exsanguination following an overdose of isoflurane anaesthetic. Briefly, the heart with occluder attached was swiftly removed. The coronary artery was occluded in the same position by re-inflating the occluder balloon. Evan's blue dye (2%, 0.6ml) was injected retrogradely into the ascending aorta to delineate the area at risk. The heart was cut parallel to the atrioventricular groove in 1-mm thick slices. These were then incubated in 1% triphenyltetrazolium chloride (TTC) at 37°C for 20 min followed by 90 minutes in formalin. Viable myocardium stains red and necrotic area remains unstained by TTC. The slices were photographed using a colour camera (Canon Powershot G12). The images were analysed using ImageJ (Rasband, W.S., ImageJ, National Institutes of Health, Bethesda, Maryland, USA). The area stained blue was defined as the remote area and the unstained area as the area at risk (AAR). The AAR was then divided into infarcted (white) and viable (red) myocardium.

6.3.7 Statistical Analysis

Continuous variables are expressed as mean ± standard deviation (SD). The Wilcoxon matched-pairs signed rank test was used to assess the statistical significance of differences measured at the different stages upon reperfusion. Results were considered to be significant at $P < 0.05$.

6.4 Results

6.4.1 Groups

Full datasets were available for 5, 5, 4, 5, and 4 animals in groups 1 to 5, respectively.

6.4.2 Left Ventricular Function

Baseline left ventricular function was measured at 69 ± 5%. At the end of each protocol, ejection fraction had reduced to 64 ± 4%. (15 minutes), 55 ± 6% (30 minutes), 47 ± 6% (60 minutes).

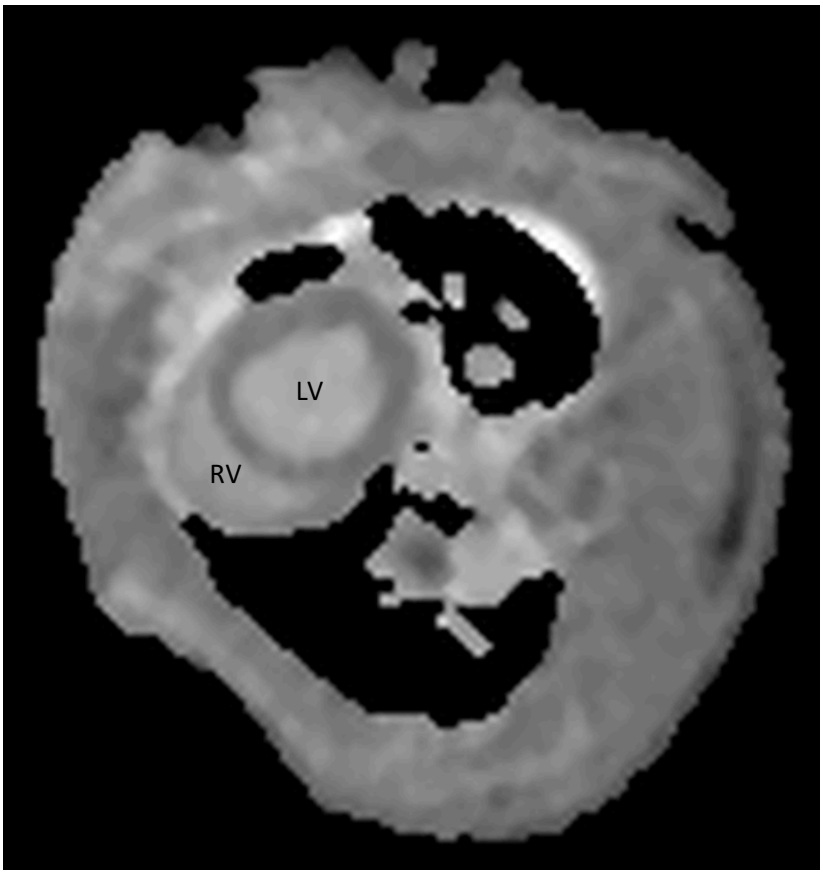

Figure 6-2. Short axis T_1 map of the left ventricle (LV) prior to myocardial ischemia demonstrating homogenous signal across the myocardium at baseline. The walls of the right ventricle (RV) may also be identified.

6.4.3 Infarct Size and Area at Risk

The area at risk (AAR) was measured at 39.8% ± 12%. The AAR did not differ between groups (p=0.93). In the groups without preconditioning, infarct size was larger with increasing duration of ischemia (15 minutes 7.8% ± 3%, 30 minutes 35.0% ± 7%, 60 minutes 51.3% ± 7%). Infarct size tended to be smaller in both the 30-minute preconditioned groups (26.5% ± 6% versus 35.0% ± 7%, p =0.097) and the 60-minute preconditioned group (42.5% ± 4% versus 51.3% ± 7%, p = 0.079), however neither of these values reached statistical significance.

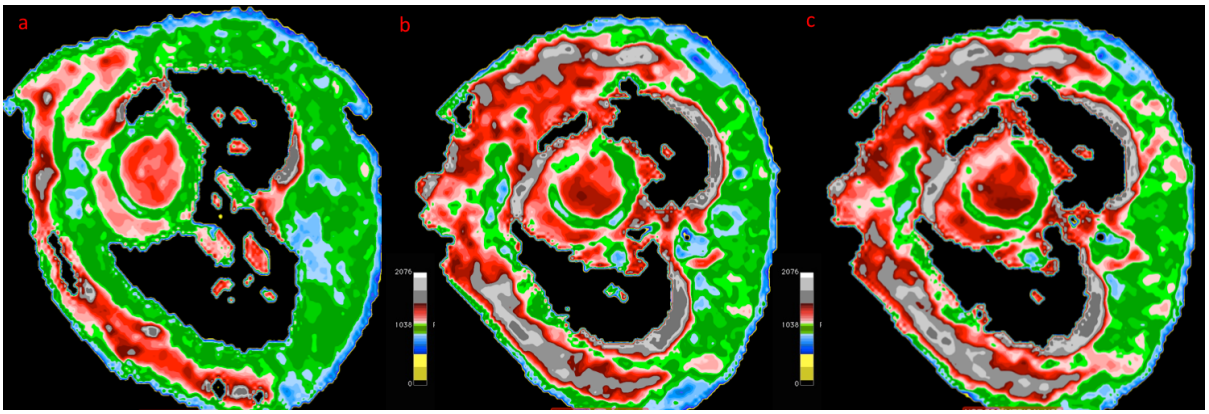

Figure 6-3. Sequential colour T_1 maps in one animal demonstrating the gradual evolution of changes in T_1 values in the anterior segment of myocardium (a) before, (b) after 15 minutes and (c) after 60 minutes of ischemia.

6.4.4 Acute Alteration in T_1 Values

Baseline T_1 values were 1049 ± 37 ms. Following 15 minutes of myocardial ischemia, T_1 values in the area at risk increased significantly to 1205 ± 21ms ($p<0.001$) and remained significantly elevated at each stage of ischemia. An example of the changes can be seen in the T_1 maps in Figure 6-4. However, following the initial increase in myocardial T_1, T_1 values increased only modestly between 15 (1205 ± 21ms) and 60 minutes of ischemia (1241 ± 21ms) ($p<0.05$) (Figure 6-4).

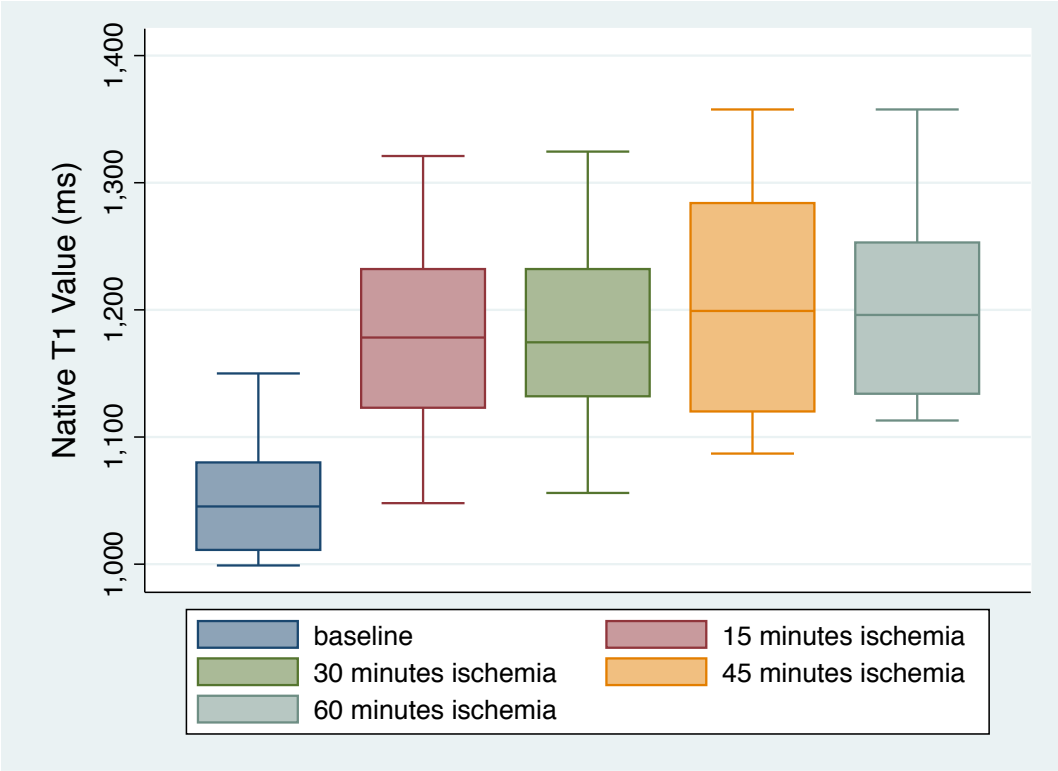

Figure 6-4. Box plots show changes in native T_1 between baseline, after 15, 30 and 60 minutes of myocardial ischemia.

6.4.5 Effects of Myocardial Reperfusion.

Myocardial reperfusion was not associated with a significant change in myocardial T_1. Myocardial T_1 remained elevated at approximately 1200ms during the 90 minutes of reperfusion, irrespective of whether the ischemic duration was 15, 30 or 60 minutes (p=ns) (Figure 6-5).

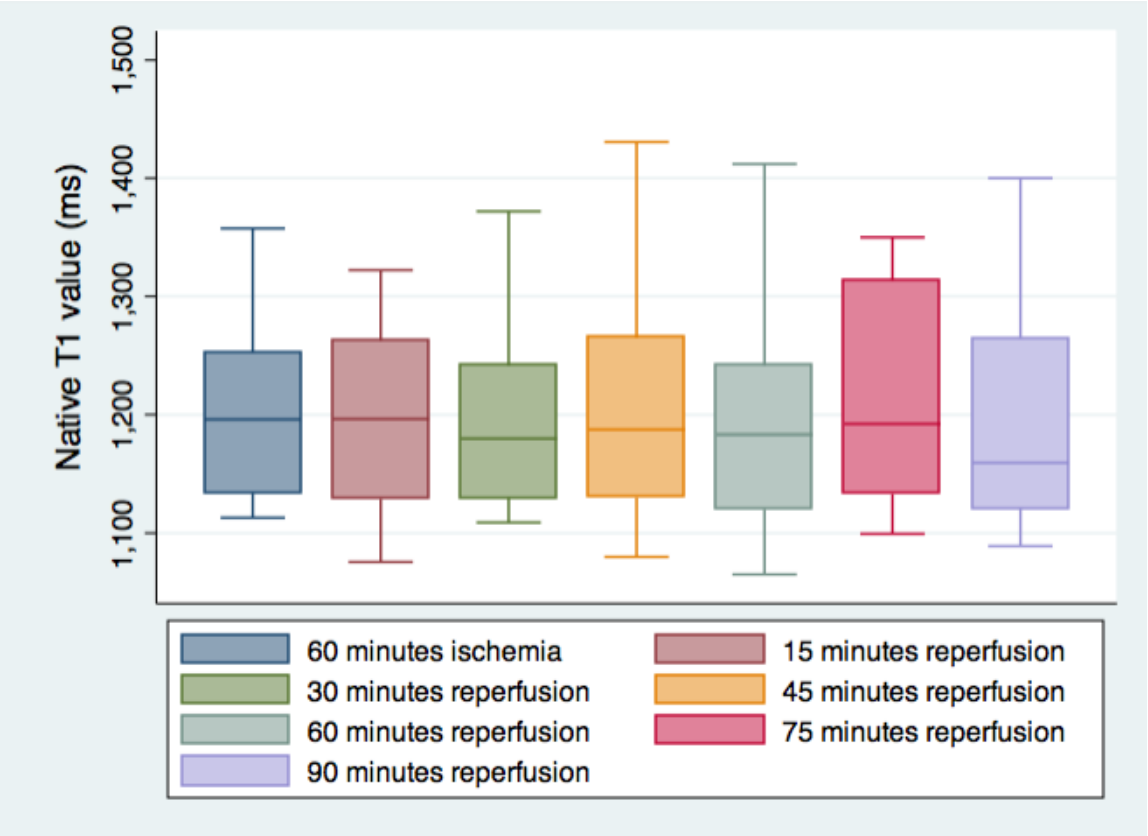

Figure 6-5. Box plots comparing the native T_1 after 60 minutes of ischemia with the various stages of reperfusion.

6.4.6 Effects of Preconditioning

Following three cycles of 5 minutes of ischemic conditioning, myocardial T_1 in the area at risk increased more slowly to reach a peak of 1166 ± 40 at 60 minutes. The T_1 value at each stage ischemia in the conditioned myocardium was significantly less than that of the non-conditioned ischemic myocardium ($p<0.05$) (Figure 6-6).

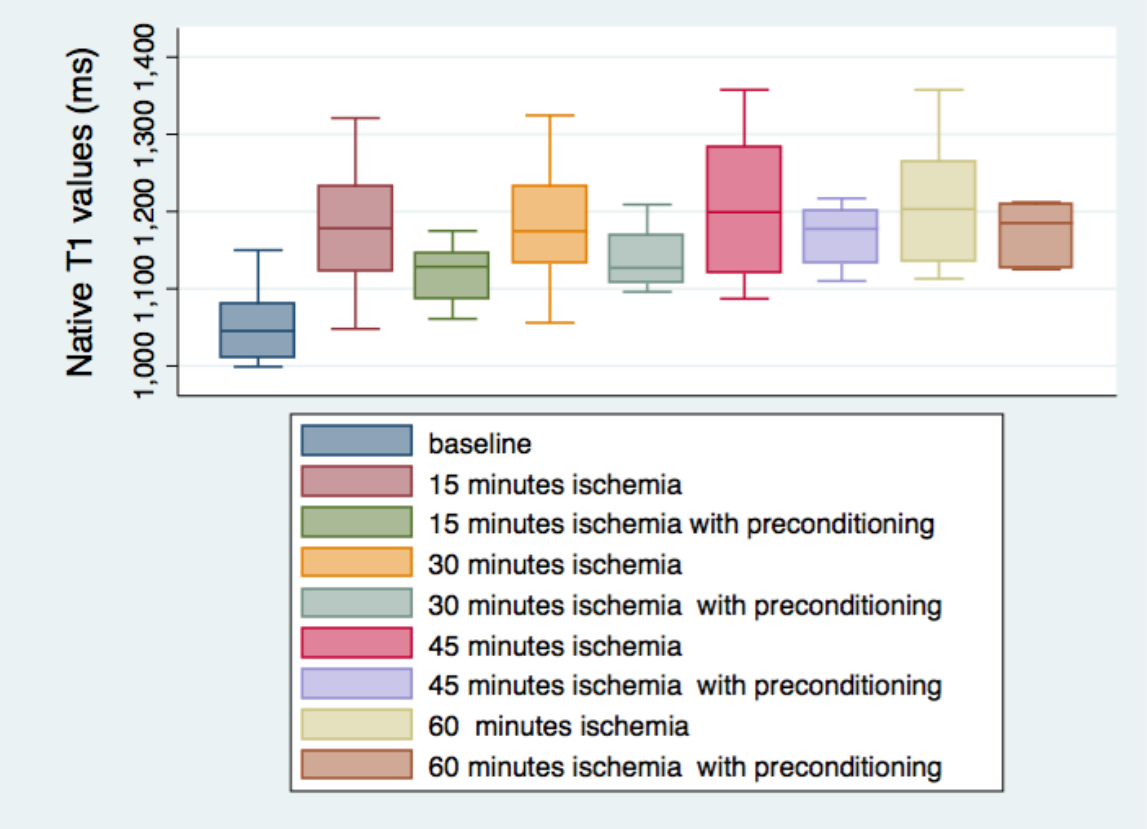

Figure 6-6. Comparison of the effect of preconditioning on the rise in T_1 values at each stage of ischemia.

6.4.7 Findings at Three and Seven Days

T_1 values in the AAR remained elevated at three (1203 ± 79ms) and seven days (1240 ± 79ms). There were no significant differences between the T_1 values at the end of reperfusion to those at three or seven days ($p=0.06$). These values were significantly higher than the T_1 of remote myocardium at both of these time points ($p<0.001$) (Figure 6-9).

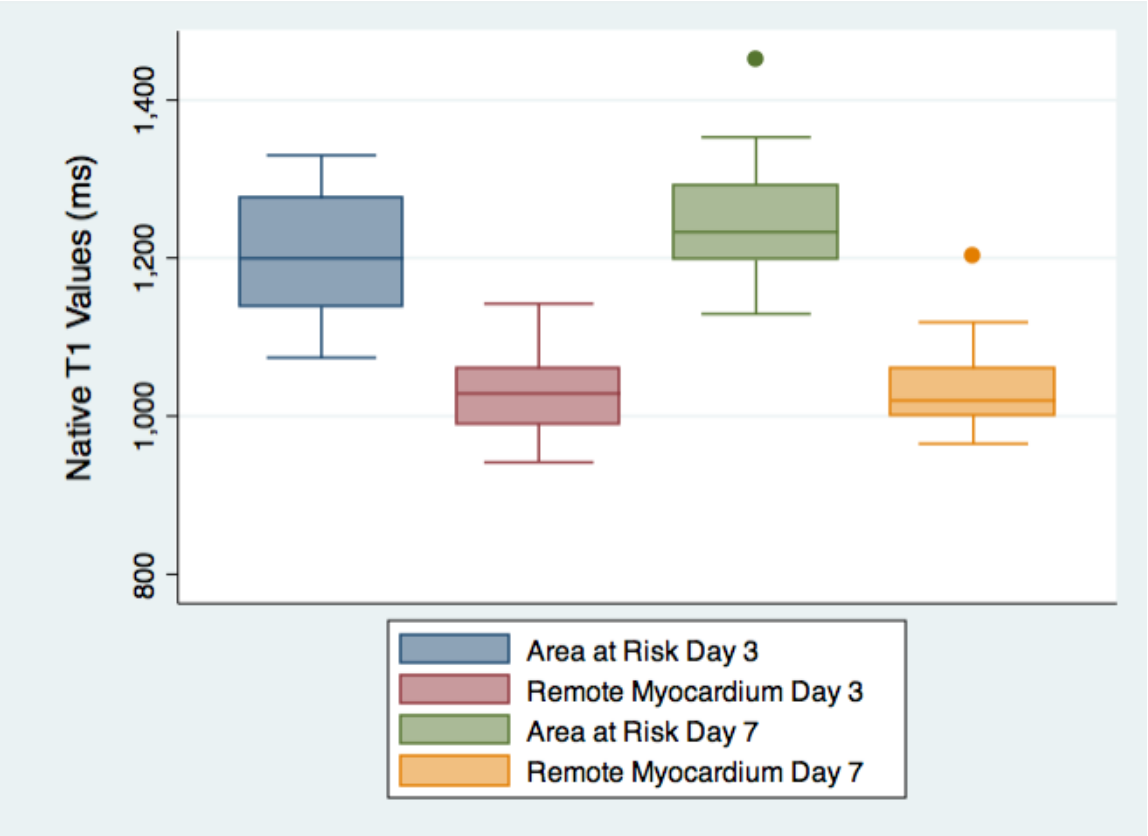

Figure 6-7. Comparison of the native T_1 values in the area at risk (AAR) and remote myocardium at three and seven days.

6.4.8 Post-Contrast T_1 Values

Following injection of iv gadolinium contrast agent, T_1 values in the AAR was significantly shorter than that in remote myocardium at both three (392 ± 51 vs 521 ± 71) and seven days (368 ± 111 vs 500 ± 134). A post-contrast colour T_1 map can be seen in Figure 6-8. There was no significant change in the post-contrast T_1 values at three or seven days (Figure 6-9).

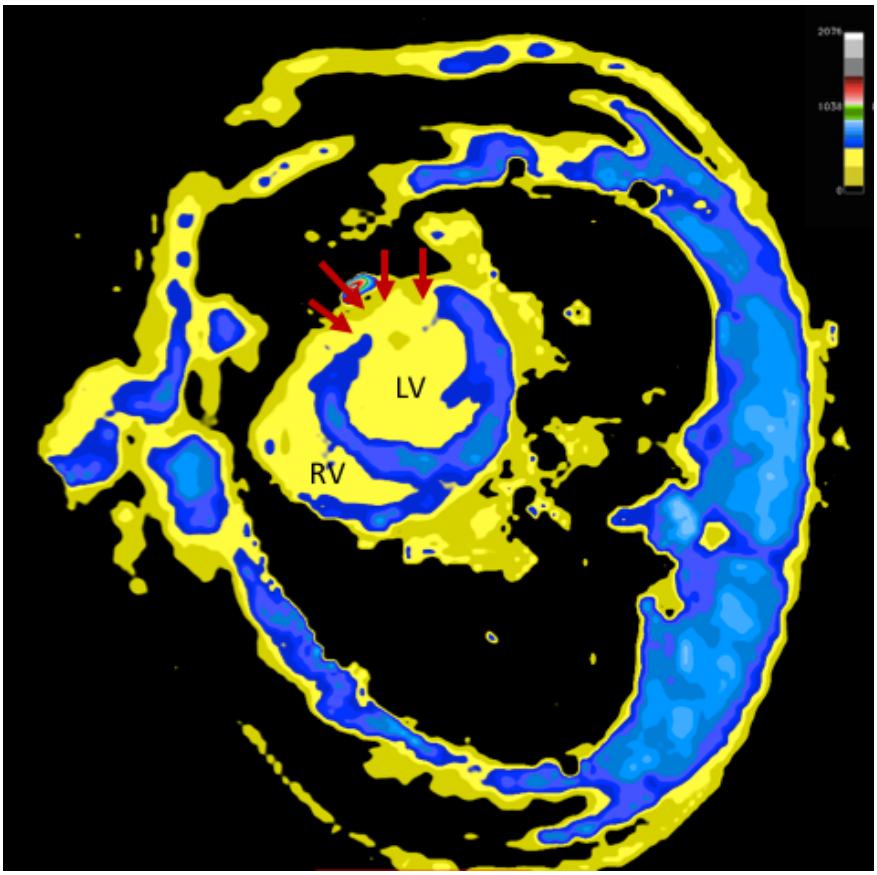

Figure 6-8. Post contrast T_1 map demonstrating a large anterior segment of myocardial injury (arrows) in the left ventricle following 60 minutes of myocardial ischemia.

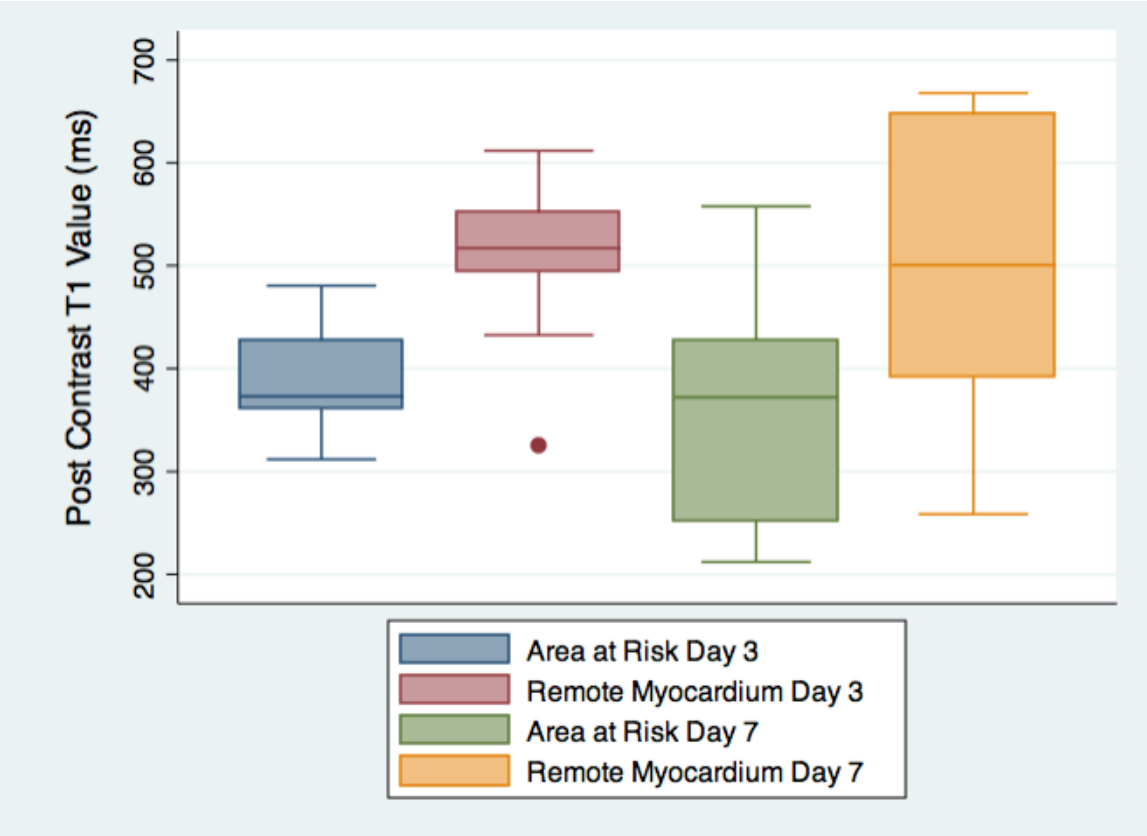

Figure 6-9. Comparison post-contrast T_1 values in the area-at-risk (AAR) and remote myocardium at three and seven days.

6.5 Discussion

In this study, we found that the T_1 values in ischemic myocardium change in the first 15 minutes following the onset of myocardial ischemia. Myocardial T_1 in the AAR was only slightly longer after 60 minutes of ischemia that after 15 minutes of ischemia. These values remain elevated during the first 90 minutes following myocardial reperfusion, irrespective of the duration of the index ischemia. Preconditioning lead to a more gradual increase in myocardial T_1 in ischemic myocardium, and was significantly lower in preconditioned ischemic myocardium than in non-conditioned myocardium. T_1 values remained elevated in the AAR at both three and seven days and were significantly lower in the AAR following the injection of gadolinium contrast agent that in remote myocardium at both of these stages.

Using the novel animal model, we were able to study the acute development of myocardial oedema in real-time. Following just 15 minutes of myocardial ischemia, native T_1 values were significantly increased, indicating an early increase in myocardial water content. Control of water content is tightly regulated aspect of cellular homoeostasis. Following the onset of ischemia,

myocardial cells are unable to control water content, leading to myocardial oedema, both intracellular and extracellular. This early swelling has been demonstrated to be predominantly intracellular (20). Following reperfusion, there is an increase in interstitial oedema (20), thought to be due to reactive hyperaemia and leakage from damaged capillaries.

CMR has a number of properties that allow it to characterise myocardium, and to evaluate myocardial water content. T_2 weighted sequences have been used to demonstrate increased myocardial water content and oedema in both ischemic myocardium (21, 22) and myocarditis (23). T_2 weighted imaging can be technically challenging, and, like LGE does not offer quantitative measurements to allow comparison between subjects and different studies. These studies have recently been supplemented by newer studies using T_2 mapping techniques that demonstrated similar increases in T_2 values in both myocardial ischemia (24, 25) and myocarditis (26). In fact, a recent study found that T_2 values were closely related to the changes in myocardial water content following myocardial ischemia (27).

Similar to T_2 values, it has been known for over thirty years that T_1 increases in ischemic myocardium (28, 29). Changes in both T_2 and native T_1 values have been validated by microspheres in dog models of myocardial ischemia (24), with excellent agreement between both measurements to detect the myocardial AAR. T_1 mapping has the advantage that native and post-contrast values can be used to study changes the composite water signal from interstitium and myocytes (native values), whereas changes in post-contrast T_1 reflects the extravascular compartment.

We did not notice a significant change in T_1 values following myocardial reperfusion, as might be expected from earlier studies. In the case of the briefer periods of ischemia, the reactive hyperemia may have been balanced by a return to baseline of normal cellular and intracellular oedema (30). It may also be that our study was underpowered to detect differences in myocardial oedema at reperfusion after 60 minutes of ischemia.

We found that three cycles of 5 minutes of preconditioning with 5 minutes of reperfusion led to a more gradual increase in myocardial T_1, with peak T_1 values not reaching that of remote myocardium. Lower T_1 values are in keeping the finding that preconditioning reduced myocardial oedema in studies of both rats (31) and pigs (32). It is thought that one of the actions of

preconditioning is to make myocardial cells more resistant to membrane rupture when challenged with hypotonic media (33). Alterations in channels involved in cell volume regulation, therefore, might be involved in the cardioprotection achieved by ischemic preconditioning.

Preconditioning is thought to stimulate the release of a large number of substrates, including adenosine, acetylcholine, catecholamines, bradykinin, endothelin and opioids. For example, adenosine, formed from the breakdown of ATP in ischemic cells, has been demonstrated to cause preconditioning in humans (34). These substrates, in turn, are thought to activate a number of critical pathways. These include the activation of protein kinases, including protein kinase C, and the opening of ATP-dependent potassium channels. For example, opening the mitochondrial ATP-dependent potassium channels can lead to reduced cardiac output and improved myocardial survival (35). Ultimately, these pathways inhibit the opening of the mitochondrial permeability transition pore. It thought that the opening of this pore leads to both cellular apoptosis and necrosis.

Preconditioning has not only demonstrated reduced oedema in myocardial cells, but it has also been found to reduce cerebral oedema as a result of cerebral artery occlusion (36). It is thought that channels involved in cell volume regulation are activated, preventing cell rupture and death (37). Another possibility is that preconditioned cells have less accumulation of lactate and phosphate catabolites during ischemia, as these have been reduced by the episodes of preconditioning. Lower level of these catabolites results in less osmotic cellular swelling during reperfusion (32). It has been proposed that acutely oedematous cardiac cells are more prone to cell death following reperfusion (38), which would support a strategy of the reduction of acute cellular oedema. Our finding that preconditioning was associated with a smaller increase in myocardial T_1 supports the conclusions of previous studies that found a preconditioning resulted in reduced cellular oedema.

Elevated T_1 was persistent both three and seven days after index ischemia. A recent study using T_2 mapping in a pig model of myocardial ischemia (27) found that the formation of oedema was a bimodal process, with an early increase in myocardial water content, followed by a decrease on day one. Water content increased again on day four before reaching a peak on day seven. We found that T_1 was slightly, but not significantly, lower on day three than at day seven. We did not

measure T_1 values at day one following ischemia, and cannot therefore confirm acute variations in T_1 values following myocardial ischemia.

6.5.1 Study Limitations

Our model typically creates an AAR of 42%, with the AAR involving predominantly the anterior and anterolateral segments of the heart. As the rat has no collateral vessels, the AAR is transmural. However, the size of the rat heart and resolution of our imaging mean we are unable to determine transmural variations in T_1 values.

6.6 Conclusion

In a small animal model of myocardial ischemia, native T_1 values increase early following the onset of myocardial ischemia. Longer periods of ischemia resulted in slightly higher T_1 values; however, myocardial reperfusion was not associated with an increase in T_1. Native T_1 values remained elevated at both three and seven days following myocardial ischemia. Preconditioning led to a more gradual increase in myocardial T_1, with values not reaching those of non-conditioned myocardium, suggesting that preconditioning leads to a reduction in myocardial oedema. T_1 mapping might serve as a non-invasive tool for assessing the immediate impact of reperfusion strategies.

6.7 References:

(1) O h-Ici, D., Jeuthe, S., Kuehne, T., Berger, F., Kozerke, S., and Messroghli, D. (2015). Validation of SALLI, a multimodal T1 mapping method, for the evaluation of ventricular systolic function and late gadolinium enhancement. *Submitted*.

(2) Kubler, W., and Spieckermann, P.G. (1970). Regulation of glycolysis in the ischemic and the anoxic myocardium. *J. Mol. Cell. Cardiol.* **1**(4), 351-77.

(3) Lopaschuk, G.D., Ussher, J.R., Folmes, C.D., Jaswal, J.S., and Stanley, W.C. (2010). Myocardial fatty acid metabolism in health and disease. *Physiol. Rev.* **90**(1), 207-58.

(4) Allen, D.G., and Orchard, C.H. (1987). Myocardial contractile function during ischemia and hypoxia. *Circ. Res.* **60**(2), 153-68.

(5) Sanada, S., Komuro, I., and Kitakaze, M. (2011). Pathophysiology of myocardial reperfusion injury: preconditioning, postconditioning, and translational aspects of protective measures. *Am. J. Physiol. Heart Circ. Physiol.* **301**(5), H1723-41.

(6) White, H.D., and Van de Werf, F.J. (1998). Thrombolysis for acute myocardial infarction. *Circulation* **97**(16), 1632-46.

(7) Keeley, E.C., Boura, J.A., and Grines, C.L. (2003). Primary angioplasty versus intravenous thrombolytic therapy for acute myocardial infarction: a quantitative review of 23 randomised trials. *Lancet* **361**(9351), 13-20.

(8) Jennings, R.B., Sommers, H.M., Smyth, G.A., Flack, H.A., and Linn, H. (1960). Myocardial necrosis induced by temporary occlusion of a coronary artery in the dog. *Arch. Pathol.* **70**, 68-78.

(9) Searle, J., Kerr, J.F., and Bishop, C.J. (1982). Necrosis and apoptosis: distinct modes of cell death with fundamentally different significance. *Pathol. Annu.* **17 Pt 2**, 229-59.

(10) Kalogeris, T., Baines, C.P., Krenz, M., and Korthuis, R.J. (2012). Cell biology of ischemia/reperfusion injury. *Int. Rev. Cell Mol. Biol.* **298**, 229-317.

(11) Frangogiannis, N.G., Smith, C.W., and Entman, M.L. (2002). The inflammatory response in myocardial infarction. *Cardiovasc. Res.* **53**(1), 31-47.

(12) Murry, C.E., Jennings, R.B., and Reimer, K.A. (1986). Preconditioning with ischemia: a delay of lethal cell injury in ischemic myocardium. *Circulation* **74**(5), 1124-36.

(13) Li, Y., and Kloner, R.A. (1993). The cardioprotective effects of ischemic 'preconditioning' are not mediated by adenosine receptors in rat hearts. *Circulation* **87**(5), 1642-8.

(14) Schott, R.J., Rohmann, S., Braun, E.R., and Schaper, W. (1990). Ischemic preconditioning reduces infarct size in swine myocardium. *Circ. Res.* **66**(4), 1133-42.

(15) Deutsch, E., Berger, M., Kussmaul, W.G., Hirshfeld, J.W., Jr., Herrmann, H.C., and Laskey, W.K. (1990). Adaptation to ischemia during percutaneous transluminal coronary angioplasty. Clinical, hemodynamic, and metabolic features. *Circulation* **82**(6), 2044-51.

(16) Yellon, D.M., Alkhulaifi, A.M., and Pugsley, W.B. (1993). Preconditioning the human myocardium. *Lancet* **342**(8866), 276-7.

(17) Curtis, M.J., and Hearse, D.J. (1989). Ischaemia-induced and reperfusion-induced arrhythmias differ in their sensitivity to potassium: implications for mechanisms of initiation and maintenance of ventricular fibrillation. *J. Mol. Cell. Cardiol.* **21**(1), 21-40.

(18) Rosset, A., Spadola, L., and Ratib, O. (2004). OsiriX: an open-source software for navigating in multidimensional DICOM images. *J. Digit. Imaging* **17**(3), 205-16.

(19) Bohl, S., Medway, D.J., Schulz-Menger, J., Schneider, J.E., Neubauer, S., and Lygate, C.A. (2009). Refined approach for quantification of in vivo ischemia-reperfusion injury in the mouse heart. *Am. J. Physiol. Heart Circ. Physiol.* **297**(6), H2054-8.

(20) Whalen, D.A., Jr., Hamilton, D.G., Ganote, C.E., and Jennings, R.B. (1974). Effect of a transient period of ischemia on myocardial cells. I. Effects on cell volume regulation. *Am. J. Pathol.* **74**(3), 381-97.

(21) Abdel-Aty, H., Zagrosek, A., Schulz-Menger, J., Taylor, A.J., Messroghli, D., Kumar, A., Gross, M., Dietz, R., and Friedrich, M.G. (2004). Delayed enhancement and T2-weighted cardiovascular magnetic resonance imaging differentiate acute from chronic myocardial infarction. *Circulation* **109**(20), 2411-6.

(22) O h-Ici, D., Ridgway, J.P., Kuehne, T., Berger, F., Plein, S., Sivananthan, M., and Messroghli, D.R. (2012). Cardiovascular magnetic resonance of myocardial edema using a short inversion time inversion recovery (STIR) black-blood technique: diagnostic accuracy of visual and semi-quantitative assessment. *J. Cardiovasc. Magn. Reson.* **14**, 22.

(23) Abdel-Aty, H., Boye, P., Zagrosek, A., Wassmuth, R., Kumar, A., Messroghli, D., Bock, P., Dietz, R., Friedrich, M.G., and Schulz-Menger, J. (2005). Diagnostic performance of cardiovascular magnetic resonance in patients with suspected acute myocarditis: comparison of different approaches. *J. Am. Coll. Cardiol.* **45**(11), 1815-22.

(24) Ugander, M., Bagi, P.S., Oki, A.J., Chen, B., Hsu, L.Y., Aletras, A.H., Shah, S., Greiser, A., Kellman, P., and Arai, A.E. (2012). Myocardial Edema as Detected by Pre-Contrast T1 and T2 CMR Delineates Area at Risk Associated With Acute Myocardial Infarction. *JACC Cardiovasc. Imaging* **5**(6), 596-603.

(25) Verhaert, D., Thavendiranathan, P., Giri, S., Mihai, G., Rajagopalan, S., Simonetti, O.P., and Raman, S.V. (2011). Direct T2 quantification of myocardial edema in acute ischemic injury. *JACC Cardiovasc. Imaging* **4**(3), 269-78.

(26) Thavendiranathan, P., Walls, M., Giri, S., Verhaert, D., Rajagopalan, S., Moore, S., Simonetti, O.P., and Raman, S.V. (2012). Improved detection of myocardial involvement in acute inflammatory cardiomyopathies using T2 mapping. *Circ. Cardiovasc. Imaging* **5**(1), 102-10.

(27) Fernandez-Jimenez, R., Sanchez-Gonzalez, J., Aguero, J., Garcia-Prieto, J., Lopez-Martin, G.J., Garcia-Ruiz, J.M., Molina-Iracheta, A., Rossello, X., Fernandez-Friera, L., Pizarro, G.*, et al.* (2015). Myocardial edema after ischemia/reperfusion is not stable and follows a bimodal pattern: imaging and histological tissue characterization. *J. Am. Coll. Cardiol.* **65**(4), 315-23.

(28) Higgins, C.B., Herfkens, R., Lipton, M.J., Sievers, R., Sheldon, P., Kaufman, L., and Crooks, L.E. (1983). Nuclear magnetic resonance imaging of acute myocardial infarction in dogs: alterations in magnetic relaxation times. *Am. J. Cardiol.* **52**(1), 184-8.

(29) Williams, E.S., Kaplan, J.I., Thatcher, F., Zimmerman, G., and Knoebel, S.B. (1980). Prolongation of proton spin lattice relaxation times in regionally ischemic tissue from dog hearts. *J. Nucl. Med.* **21**(5), 449-53.

(30) Jennings, R.B., Schaper, J., Hill, M.L., Steenbergen, C., Jr., and Reimer, K.A. (1985). Effect of reperfusion late in the phase of reversible ischemic injury. Changes in cell volume, electrolytes, metabolites, and ultrastructure. *Circ. Res.* **56**(2), 262-78.

(31) Kevelaitis, E., Peynet, J., Mouas, C., Launay, J.M., and Menasche, P. (1999). Opening of potassium channels: the common cardioprotective link between preconditioning and natural hibernation? *Circulation* **99**(23), 3079-85.

(32) Sanz, E., Garcia Dorado, D., Oliveras, J., Barrabes, J.A., Gonzalez, M.A., Ruiz-Meana, M., Solares, J., Carreras, M.J., Garcia-Lafuente, A., Desco, M.*, et al.* (1995).

Dissociation between anti-infarct effect and anti-edema effect of ischemic preconditioning. *Am. J. Physiol.* **268**(1 Pt 2), H233-41.

(33) Armstrong, S., Downey, J.M., and Ganote, C.E. (1994). Preconditioning of isolated rabbit cardiomyocytes: induction by metabolic stress and blockade by the adenosine antagonist SPT and calphostin C, a protein kinase C inhibitor. *Cardiovasc. Res.* **28**(1), 72-7.

(34) Mullane, K., and Bullough, D. (1995). Harnessing an endogenous cardioprotective mechanism: cellular sources and sites of action of adenosine. *J. Mol. Cell. Cardiol.* **27**(4), 1041-54.

(35) Miura, T., Kawamura, S., Tatsuno, H., Ikeda, Y., Mikami, S., Iwamoto, H., Okamura, T., Iwatate, M., Kimura, M., Dairaku, Y.*, et al.* (2001). Ischemic preconditioning attenuates cardiac sympathetic nerve injury via ATP-sensitive potassium channels during myocardial ischemia. *Circulation* **104**(9), 1053-8.

(36) Masada, T., Hua, Y., Xi, G., Ennis, S.R., and Keep, R.F. (2001). Attenuation of ischemic brain edema and cerebrovascular injury after ischemic preconditioning in the rat. *J. Cereb. Blood Flow Metab.* **21**(1), 22-33.

(37) Diaz, R.J., Losito, V.A., Mao, G.D., Ford, M.K., Backx, P.H., and Wilson, G.J. (1999). Chloride channel inhibition blocks the protection of ischemic preconditioning and hypo-osmotic stress in rabbit ventricular myocardium. *Circ. Res.* **84**(7), 763-75.

(38) Ruiz-Meana, M., Garcia-Dorado, D., Gonzalez, M.A., Barrabes, J.A., and Soler-Soler, J. (1995). Effect of osmotic stress on sarcolemmal integrity of isolated cardiomyocytes following transient metabolic inhibition. *Cardiovasc. Res.* **30**(1), 64-9.

Chapter 7 Hyperpolarised Metabolic MR Imaging of Acute Myocardial Changes and Recovery upon Ischemia-Reperfusion in a Small Animal Model

7.1 Abstract

The aim of this study was to implement hyperpolarised MR imaging in an animal model of ischemia/reperfusion and to assess in-vivo the regional changes in pyruvate metabolism within the first hour and at one week upon a brief episode of coronary occlusion and subsequent reperfusion.

All animal experiments were performed in adherence to the Swiss law of Animal Protection and approved by the Zurich cantonal veterinary office. A closed-chest rat model was implemented using an inflatable balloon secured around the left coronary artery. The rats were placed in an MR system 5-7 days after surgery. [1-^{13}C]pyruvate was polarised using a home-built multi-sample hyperpolariser. Rats were injected with hyperpolarised pyruvate at five stages: baseline, on reperfusion after 15 minutes of coronary occlusion, after 30 and 60 minutes and 1 week later. The conversion of pyruvate to lactate and bicarbonate was imaged using dedicated MR sequences alongside wall motion and delayed enhancement imaging. Following imaging, the heart was removed and stained to delineate the area-at-risk. Differences between AAR and remote myocardium were assessed using a repeated measures analysis of variance (ANOVA) and a posthoc Bonferroni multiple comparison test.

Data were collected in 12 animals. Occlusion led to hypokinesia of the anterior or anterolateral segments of the myocardium. On reperfusion, the average lactate/bicarbonate area-under-the-curve ratio increased in the AAR relative to baseline (from 1.93±0.5 to 3.01±0.7, $p<0.001$) and was significantly higher compared to the remote area (1.91±0.4, $p<0.001$). In the 60 minutes following occlusion the lactate/bicarbonate ratio in the AAR recovered but was still elevated relative to the remote area. One week after ischemia/reperfusion no difference between the AAR and the remote area could be detected.

Hyperpolarised metabolic MR imaging successfully detects acute changes in [1-^{13}C]pyruvate metabolism following ischemia/reperfusion. Myocardial metabolism was abnormal in the area-at-risk during the first 60 minutes following ischemia but returned to normal one week later.

7.2 Introduction

Myocardial ischemia occurs when myocardial oxygen supply is insufficient to maintain normal metabolism. Increasing levels of ischemia will lead to progressive changes, beginning with diastolic dysfunction, systolic dysfunction, electrographic changes, and finally angina, a process known as the ischemic cascade (1). If the ischemia is severe, homeostasis is compromised. Prolonged ischemia will ultimately lead to cell death unless normal perfusion returns.

Currently, ischemia is predominantly detected indirectly, using electrical changes during ECG stress testing (2), relative changes in perfusion using nuclear or CMR imaging (3, 4), or abnormal myocardial function in stress echocardiography (5) or CMR (5). Although PET does have a role in quantifying metabolism, PET predominantly measures perfusion and accumulation of a tracer, but it is unable to detect downstream metabolites from the injected tracer. As metabolic changes are an initial event in the ischemic cascade, a method of detecting abnormal myocardial metabolism might allow the improved detection of myocardial ischemia.

Indeed, until now, there was no method to detect these metabolic alterations in-vivo. In addition, the metabolic changes of ischemia and subsequent reperfusion could not be studied in-vivo. Myocardial reperfusion can paradoxically compound the biochemical and metabolic changes that occur in ischemia, with the best-established manifestation of this being myocardial stunning - prolonged post-ischemic dysfunction of viable tissue salvaged by reperfusion (6). The lack of a tool to assess reperfusion injury in patients has prohibited the development of interventional or pharmacologic strategies to successfully prevent or at least minimise reperfusion injury in humans.

Hyperpolarised MR has emerged as a promising tool to address the limited sensitivity of MR imaging when probing metabolic processes. It provides the possibility to study the rapid changes in metabolism during myocardial ischemia and reperfusion, enabling the in-vivo analysis of myocardial injury with different reperfusion strategies. Using the dissolution Dynamic Nuclear Polarisation (DNP) principle (7), the MR sensitivity is increased by a factor of >10,000 allowing the study of metabolic changes occurring in the heart in real-time. Some studies have demonstrated the ability of hyperpolarised MR to interrogate substrate metabolism in the ex-vivo and in-vivo heart under various conditions (8-13). Most have used non-selective or slice-selective

MR spectroscopy to study global changes in the heart. More recently, also metabolic images have been obtained to assess regional differences in metabolism in-vivo in the pig following myocardial ischemia (15) and in the isolated perfused rat heart (16). However, there have been no in-vivo studies demonstrating regional differences in metabolism following ischemia/reperfusion in the acute and recovery phase so far.

In relation to hyperpolarised MR studies of the heart, pyruvate has been of main interest given its central role at the crossroads between glycolysis and oxidative phosphorylation and because of its relatively long relaxation times which allowing observation of metabolic turnover. With adequate oxygen supply, pyruvate is irreversibly metabolised in the mitochondria to CO_2 and Acetyl-CoA. Carbon dioxide is rapidly converted to bicarbonate (HCO_3^-) to allow for CO_2 transport and to maintain cellular pH. The presence of HCO_3^- therefore, reflects the formation of Acetyl-CoA, which then enters the Krebs cycle. Reduced bicarbonate signal may be due to reduced flux through the Krebs cycle, a switch from the metabolism of carbohydrates to oxidation of fats or ketones, or a combination of both of these two factors. Without sufficient oxygen supply, pyruvate is metabolised to lactate. This process generates a small amount of ATP and, more importantly, NAD^+, which is required for glycolysis. Therefore, regional ischemia should be marked metabolically by reduced HCO_3^- and increased lactate in the area affected or the area-at-risk (AAR). This lactate/bicarbonate ratio has been suggested as a marker of ischemia, as ischemia inhibits pyruvate metabolism to bicarbonate while simultaneously increasing tissue lactate (17).

The aim of the present study was to implement and validate hyperpolarised MR imaging in an animal model of ischemia/reperfusion and to assess in-vivo the regional changes in pyruvate metabolism within the first hour and at one week upon a brief episode of coronary occlusion and subsequent reperfusion.

7.3 Methods

All animal experiments were performed in adherence to the Swiss law of Animal Protection and approved by the Zurich cantonal veterinary office.

7.3.1 Surgery

To avoid the surgical trauma and inflammation associated with open-chest models, and to allow ischemia/reperfusion to be induced with the animal in the bore of the MRI scanner, a closed-chest model of myocardial ischemia/reperfusion was implemented as described in Chapter 3 (17).

7.3.2 Animal Preparation

Rats were anaesthetized with 4% isoflurane in an air/oxygen (4:1) mixture, endotracheally intubated and ventilated. Anesthesia was maintained using 1-2% isoflurane. Body temperature was kept at 37-38 °C using a warm water heating mat. The occluder tubing was located and the tip attached to a 20G plastic cannula and extension tubing. Two 26G i.v. cannulae were placed in opposite sides of the tail, one to allow injection of the DNP substrate, one for continuous glucose infusion (15 mg/kg/min glucose and 10 mmol/kg/min potassium) to keep blood glucose levels constant (18). Blood glucose was measured following each experiment (OneTouch Ultra 2, LifeScan, Switzerland).Anesthesia was maintained using 1-2% isoflurane in an air/oxygen (4:1) mixture during imaging. Body temperature was maintained at 37-38 °C using a warm water heating mat.

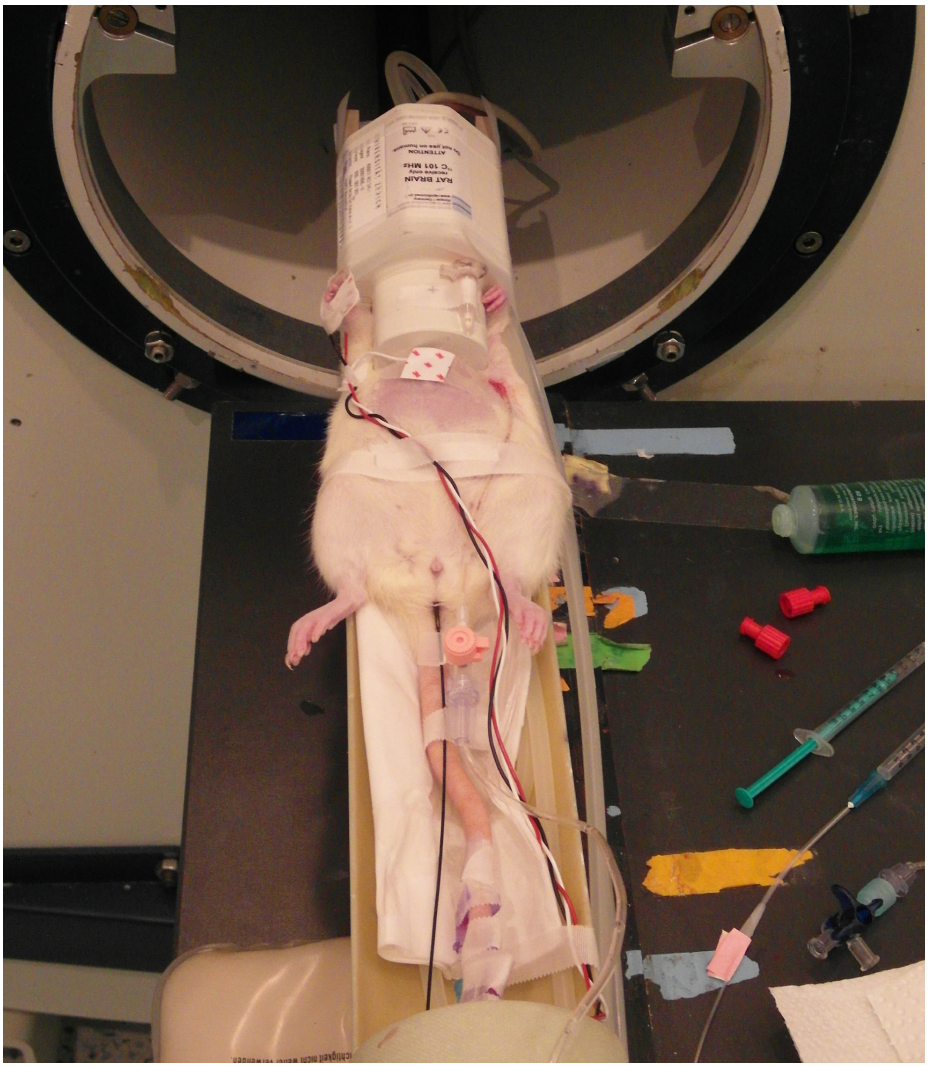

Figure 7-1. Initial setup of the Rat with temperature probe, ECG pads, iv canulae and occluder tubing in place. The warming mat is then placed over the animal to maintain a constant temperature.

7.4 Hyperpolarisation

A home-built multi-sample DNP polariser (19) was used to polarise samples consisting of 25.4 µL [1-^{13}C]pyruvic acid (Sigma-Aldrich) and 13.5 mM trityl radical (tris(8-carboxyl-2,2,6,6-tetra(2-(1-hydroxyethyl))-benzo[1,2-d;4,5-d']bis(1,3)dithiole-4-yl) methyl sodium salt)) (GE Healthcare), doped with 1.5 mM Dotarem (Guerbet, Paris, France). After 90 minutes of polarisation at 1.3 K, the sample was dissolved in 8 mL Tris buffer and neutralized with sodium hydroxide, resulting in a 44-mM [1-^{13}C]pyruvate solution at room temperature. Liquid state-polarisation of hyperpolarised [1-^{13}C]pyruvate was measured as 18.7 ± 2% at t = 30 sec after dissolution in phantom experiments and extrapolated back to t = 0 sec resulting in polarisation values of 36.4±5% for measured T_1 values of 45.2 ± 4 sec at 9.4T. To perform metabolic imaging, 1.4 mL of the hyperpolarised substrate was injected over 4 sec into the tail vein of the animals.

7.4.1 Imaging Protocol

MR imaging experiments were performed on a 9.4T Bruker Biospec 94/30 small animal MR system (Bruker BioSpin GmbH, Karlsruhe, Germany). A birdcage dual 1H/13C coil (Rapid Biomedical, Wurzburg, Germany) was used for excitation, and a 13C surface coil with sensitivity area 40 x 30 mm2 from the same vendor was placed over the thorax for signal reception.

Initially, axial and longitudinal scout images were acquired to plan the 2-chamber long-axis view. The animal was repositioned to locate the heart in the isocentre of the scanner. A 4-chamber long-axis view was then acquired perpendicular to the 2-chamber orientation, after which a series of short-axis cine MR images was obtained perpendicular to the LV long-axes from the 2- and 4-chamber images. Cine MR images were acquired using an ECG-triggered Fast Low Angle Shot (FLASH) sequence with TR/TE of 8/1.9ms, flip angle 15°, FOV 60x60 mm2, matrix = 192x192, signal averages = 4 and spatial resolution 0.31x0.31x1.27 mm3.

Before ^{13}C image acquisition, first order shimming was performed by minimizing the water line width using a localized spectroscopic pulse sequence with a voxel covering the left ventricle. The same pulse sequence was used to determine the frequency of the water peak, which then was scaled to adjust the ^{13}C centre frequency on pyruvate in the heart. The ^{13}C pulse angle was calibrated on a phantom consisting of 5M ^{13}C-labeled sodium acetate solution doped with 0.5 M gadolinium-DOTA, which was attached to the surface coil.

Metabolic data, metabolic data were acquired with a multi-band radiofrequency pulse in combination with a multi-echo single-shot EPI readout as described previously (20). In contrast to the original publication partial Fourier acquisition with 69% coverage in phase-encode direction and a smaller field of view (FOV) were used to allow for shorter echo and readout times and higher resolution. Seven echoes were acquired with an initial echo time of 5.31 ms and an echo time increment of 383 µs. The EPI readout used a matrix of 96 x 22 and a FOV of 60 x 40 mm2. Two-fold oversampling in readout direction was applied which resulted in an in-plane resolution of 1.25 x 1.25 mm2. The slice thickness was 5 mm. Each readout was triggered to end systole, and the seven readouts were repeated every 1.5 s during a total scan duration of 5 min.

To assess the reproducibility of the setup, two repeat measurements separated by 20 minutes were performed in ten healthy rats prior to the actual study.

7.4.2 Coronary Occlusion Protocol

After the baseline measurement in each operated rat, the left coronary artery (LCA) was occluded by inflating the balloon of the occluder with 0.2 mL of water and closing the 3-way stopcock. Ischemia was confirmed by ECG changes and localized hypokinesia on cine MR imaging. After 15 minutes of ischemia, the occluder balloon was deflated. Metabolic imaging was performed at four stages, at baseline, immediately after reopening of the LCA, and at 30 and 60 minutes. Cine MR imaging was performed at each of these stages. To confirm successful reperfusion and estimate myocardial injury, late gadolinium enhancement (LGE) imaging was performed at 60 minutes.

A subgroup of 8 animals was planned to be re-examined one week following ischemia/reperfusion including metabolic, cine and LGE imaging, as described above. The overall experimental protocol is illustrated in Figure 7-2.

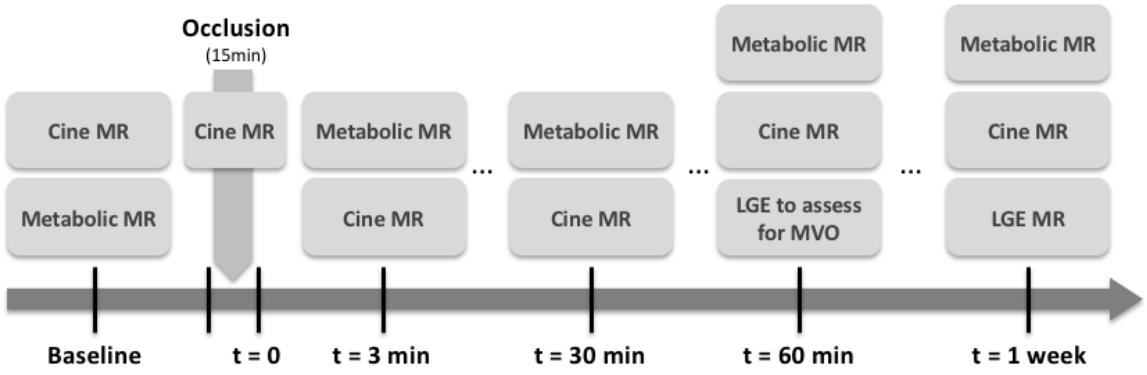

Figure 7-2. Study timeline indicating the imaging experiments performed at each step.

7.4.3 Image Processing

Metabolic images were reconstructed using the IDEAL approach (21) encoding pyruvate, lactate, bicarbonate, pyruvate hydrate and alanine resonances. After metabolite separation, EPI chemical shift was corrected for each metabolite frequency. The images were normalized to noise (determined from a late dynamic when all hyperpolarised signal has decayed) and then adjusted for the sensitivity of the ^{13}C surface coil using data acquired in a uniform 3M ^{13}C urea disk phantom. For display, metabolic maps of pyruvate, lactate and bicarbonate were overlaid

onto 1H reference images. Average signals within four myocardial sectors were computed after applying a time-averaged phase correction term for each pixel to remove phase effects due to spatially varying magnetic field inhomogeneity and to add the pixels within each ROI in phase. The signal was masked by drawing the blood pool and the four myocardial segments on the 1H reference image. Signal intensity-time curves of pyruvate, lactate and bicarbonate were integrated to obtain the area-under-the-curve (AUC).

Left ventricular function and LGE were assessed using cmr42 (Circle CVI, Calgary, Alberta, Canada). Enhanced regions were determined using the full-width-half-maximum thresholding method. Four regions were evaluated, lateral, inferior, septal, and anterior. Regional wall motion and systolic wall thickening were scored using a five-point grading scale: 1, normal; 2, mildly hypokinetic; 3, severely hypokinetic; 4, akinetic; and 5, dyskinetic. LGE was quantified on the basis of the relative area of hyperenhancement in the 4 midventricular slices of each region using the following scale: 0 - no LGE; 1 - 0-33% LGE; 2 - 34-66% LGE; 3 - 67-100% LGE.

7.4.4 Staining

Staining was performed to define myocardium as remote myocardium or area-at-risk (AAR) and to detect myocardial infarction. Full details are presented in the supplemental content. The four myocardial segments used in the analysis of the metabolic maps, wall motion and LGE data were classified as AAR or remote area according to the staining results. Similar to LGE, staining was quantified on the basis of the area of AAR to remote myocardium in the midventricular slice of each region using the following scale: 0 - no AAR; 1 - 0-33% AAR; 2 - 34-66% AAR; 3 - 67-100% AAR.

7.4.5 Statistical Analysis

Continuous variables are expressed as mean ± standard deviation (SD). A line of identity on a scattergram was drawn between each measurement to allow a visual assessment of agreement. The Bland–Altman limits of agreement were then determined. Statistical significance between AAR and remote area and between different time points was assessed using a repeated measures analysis of variance (ANOVA) and a posthoc Bonferroni multiple comparison test. A value $p<0.05$ was considered significant.

7.5 Results

In the 10 healthy animals used to test reproducibility, mean ± standard deviations of the difference in the area-under-the-curve of the lactate/bicarbonate ratio between injections were 3.5±6%, 7.0 ± 12%, 5.1 ± 12% and 0.5 ± 10% for anterior, septal, inferior and lateral myocardial segments, respectively. Bland Altman plots and regression lines can be seen in Figure 7-3.

Ischemia/reperfusion data were collected on 12 animals. Reperfusion was successful in 11 of 12 animals as evidenced by recovery of systolic function, and ECG changes. One animal without reperfusion developed further ST segment/R wave changes on ECG and continued to have severe localized hypokinesia. On LGE imaging, a central core of microvascular obstruction was observed. This animal died at the end of the initial imaging protocol and was not included in the analysis as the myocardium was not reperfused following ischemia. One other animal had evidence of infection around the occluder and heart and was also excluded.

Myocardial systolic function was normal in all regions before coronary occlusion (wall motion score 1.03 ± 0.1). All animals developed akinesia or severe hypokinesia of the anterior and lateral regions of the myocardium (3.4 ± 1.1). Function remained unchanged in remote regions (1.1 ± 0.3). Systolic function in the AAR improved on reperfusion (1.95 ± 0.9) and had recovered to near normal by 60 minutes (1.5 ± 0.5). Blood glucose at the end of scanning was 15.8 ± 1 mmol/L across all animals.

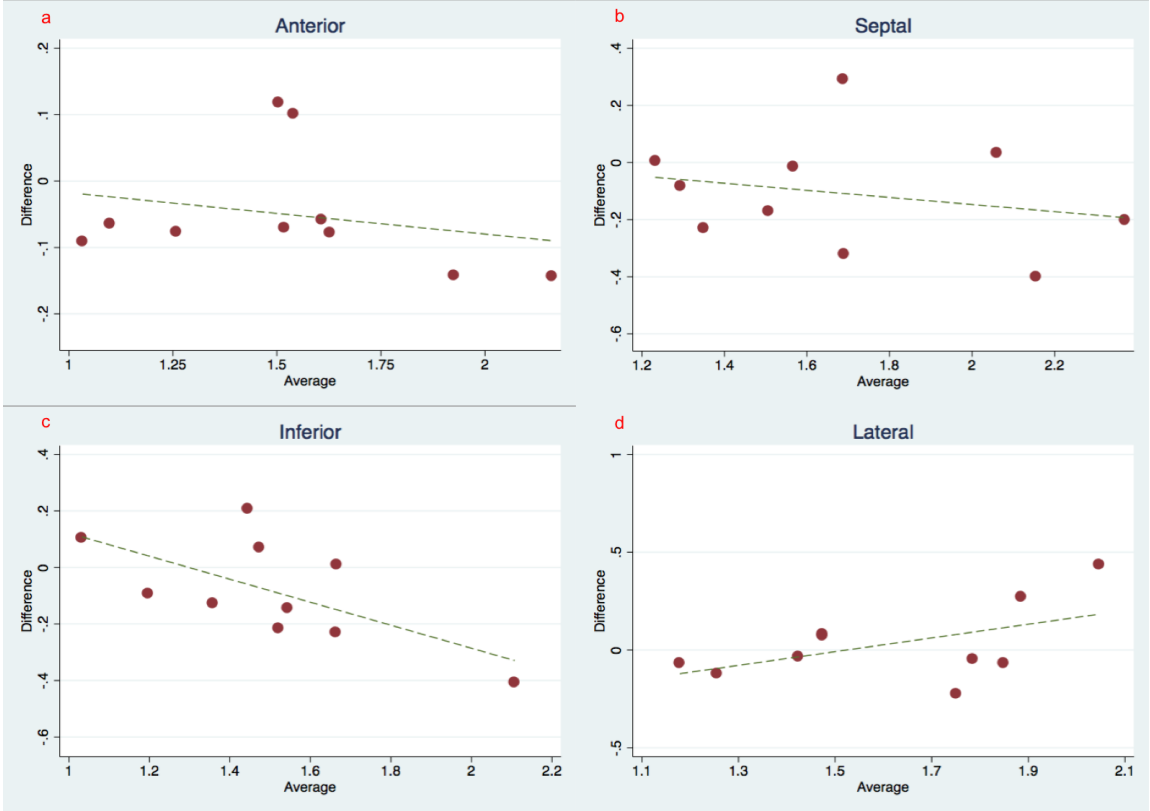

Figure 7-3. Scatter plots with line of agreement and Bland–Altman plots for comparisons between each measurement in each segment (a, b, c, d).

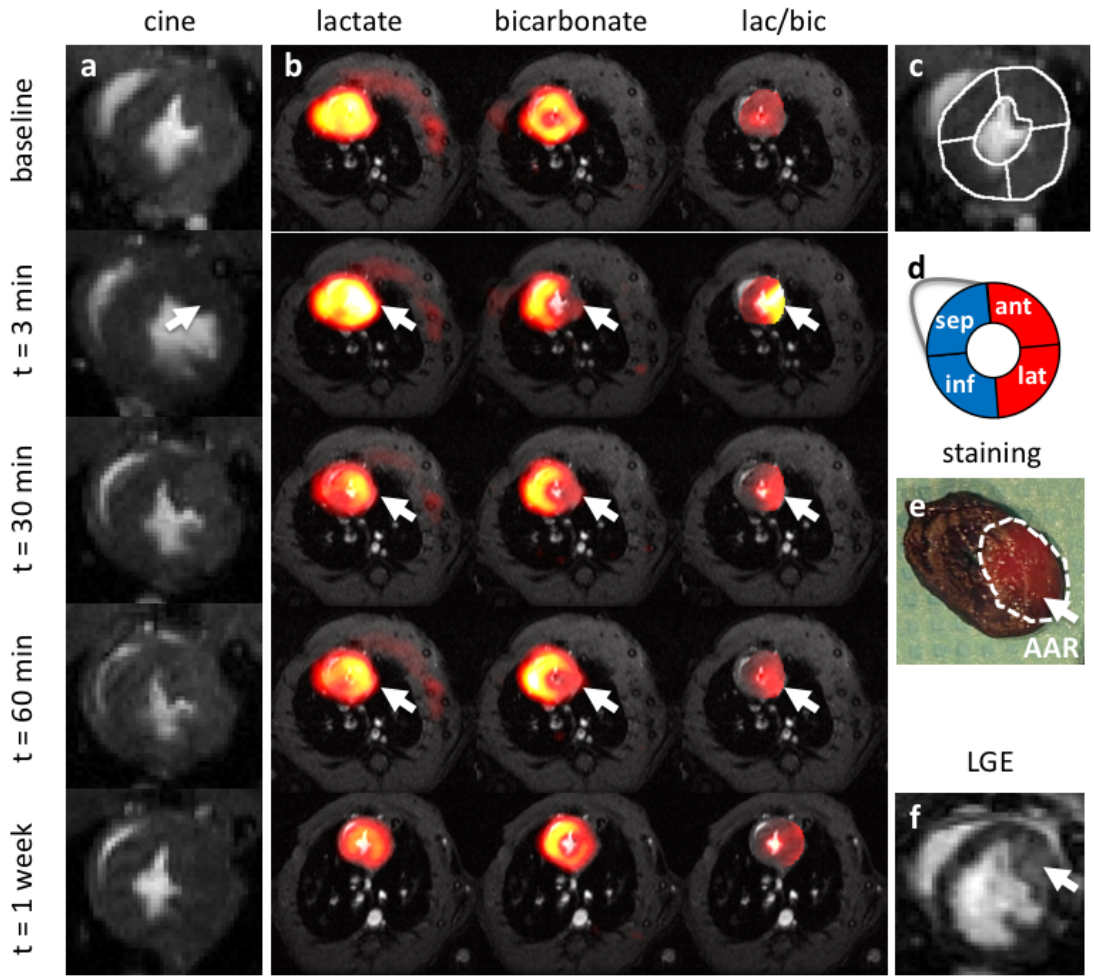

Figure 7-4. Example images at the five-time points in one animal. Left (a): Cine images show reduced systolic wall thickening in the AAR (anterior and lateral walls - arrow) on reperfusion. Middle (b): Metabolic maps of lactate, bicarbonate and lactate/bicarbonate (lac/bic) ratio (masked by myocardial segments used for analysis). In the AAR, the lactate/bicarbonate ratio is increased. Right (c,d): Cine image and schematic depiction of the four myocardial segments (AAR-red, remote myocardium – blue). (e) Evan's Blue staining dividing the myocardium into AAR – red (involving anterior and lateral segments), and remote myocardium – blue (septal and inferior). (f) Late gadolinium enhancement imaging demonstrates an area of hyperenhancement and thickening.

Metabolic images of hyperpolarised [1-^{13}C]pyruvate and its metabolites demonstrated sufficient signal-to-noise ratio (SNR) and spatial distribution at baseline in all animals. Peak pyruvate SNR in the left ventricular blood pool across all subjects was 53.7 ± 36 while lactate and bicarbonate and alanine SNR averaged over the myocardium were 13.7 ± 6, 8.4 ± 3 and 4.9 ± 1 respectively. At baseline, the lactate/bicarbonate AUC ratio was 1.79 ± 0.5. Examples of metabolic maps and derived parameter maps in one animal are given in Figure 7-4, Figure 7-5 and Figure 7-6.

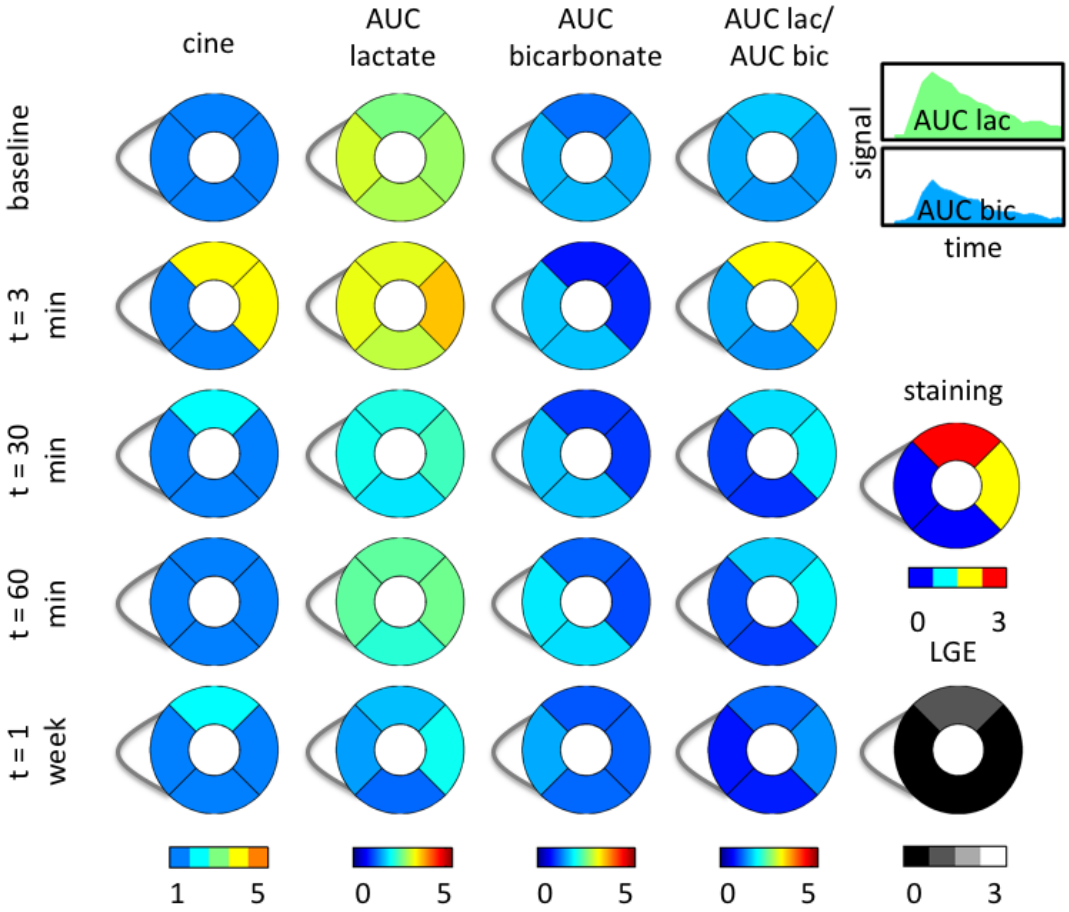

Figure 7-5. Assessment of segmental changes in metabolism and myocardial function (same animal as in Figure 2). For each time point, systolic function on cine MR; lactate, bicarbonate, and lactate/bicarbonate ratios are quantified as derived from the area-under-the-curve (AUC) of the signal intensity time curves as indicated. Myocardial staining demonstrates the area-at-risk.

The average time between reopening and injection of [1-13C] pyruvate was 3.0 ± 1 min. At this time point, the lactate/bicarbonate AUC ratio in the AAR increased relative to baseline (from 1.93 ± 0.5 to 3.01 ± 0.7, $p<0.001$) and was significantly increased relative to the ratio of the remote area (1.95 ± 0.4, $p<0.001$) (Figure 7-7).

The lactate/bicarbonate ratio in the AAR gradually recovered in the measurements at 30 (2.27 ± 0.5) and 60 minutes (2.17 ± 0.5) but was still elevated compared to the remote area (1.61 ± 0.5, $p<0.01$) (Figure 7-7).

In the animal without successful reperfusion, the lactate/bicarbonate ratio continued to increase at 30 and 60 minutes (2.92 on reperfusion to 5.72 at 60 min), suggesting continued anaerobic glycolysis and a lack of resumption of oxidative phosphorylation. The animal with infection had a

globally elevated lactate/bicarbonate ratio on the first measurements, which persisted in the examination at 1 week.

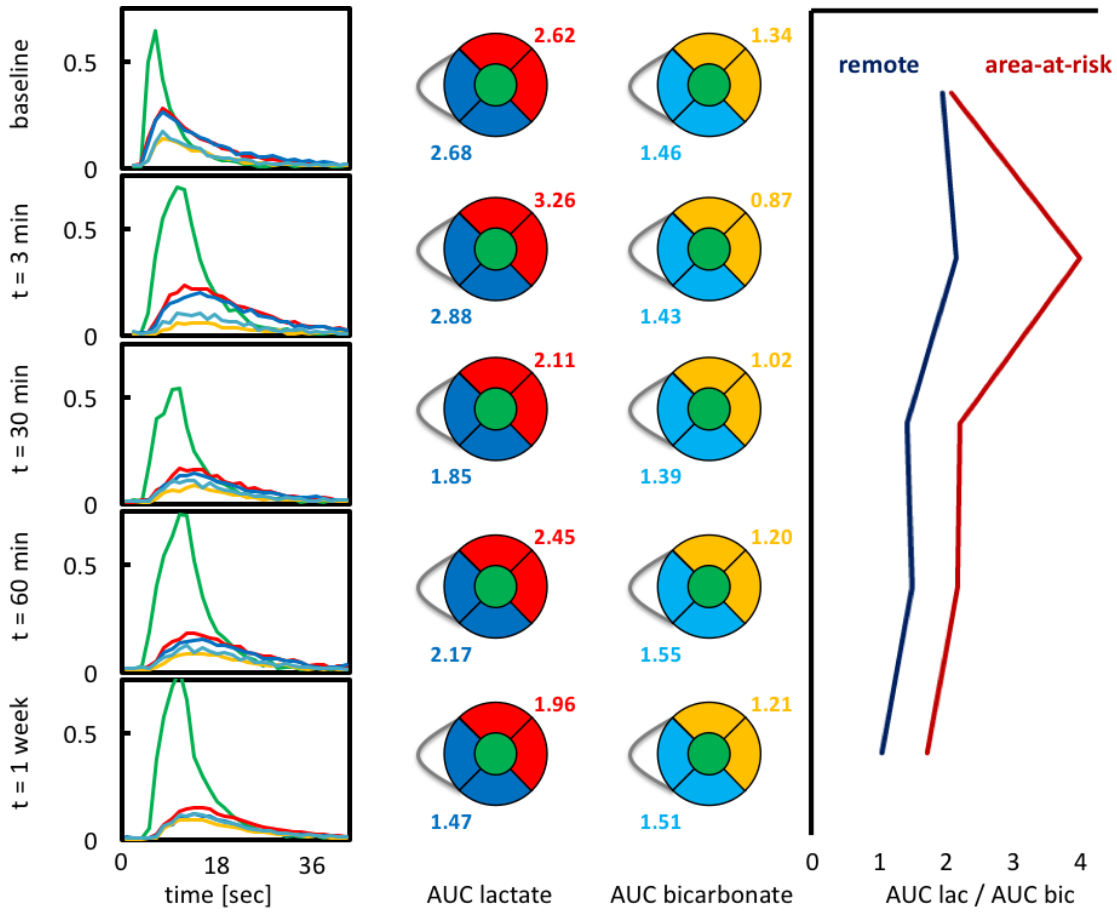

Figure 7-6. Left: Example signal intensity-time curves of pyruvate in the blood pool (green), lactate and bicarbonate in the AAR (red, orange) and remote myocardium (blue, cyan). Middle: AUC values for lactate and bicarbonate in the AAR (red, orange) and remote myocardium (blue, cyan). Right: Lactate/bicarbonate ratio as a function of time (vertical). On reperfusion, lactate/bicarbonate ratio is increased in the area-at-risk (dark red) vs. remote myocardium (dark blue) but reduces at 30 and 60 min indicating normalization of metabolism after the transient ischemic event.

Two of the eight planned animals died in the week following ischemia-reperfusion. The six remaining were scanned as intended. One week after the ischemic episode, the lactate/bicarbonate ratio in the AAR was not significantly different from the remote area (Figure 7-7). LGE imaging revealed small areas of hyperenhancement in 3 of the 6 animals (grade 0.7 ± 0.8 of the three anterior regions involved). This enhancement occurred solely in the area at risk and was not present in the remote myocardium (Figure 7-7).

The myocardial AAR of the entire heart, as determined by Evan's blue staining, was 30.3 ± 8% and involved the anterior and lateral segments exclusively (grade 2.25 ± 0.7). Very small infarcts

were detected in 8 out of 10 animals during histology with an average volume of 2.5 ± 2% of the whole myocardium.

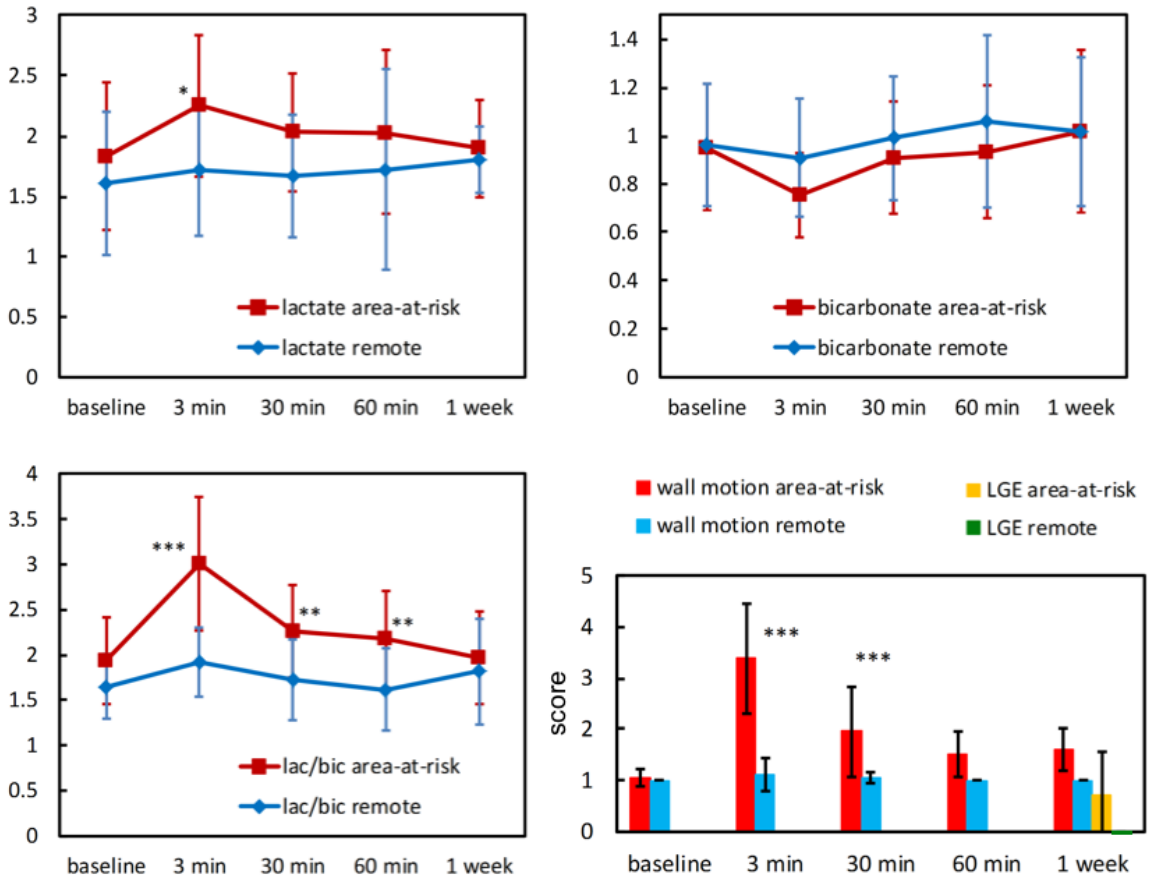

Figure 7-7. Summary of study findings. Top: Pooled AUC lactate (left) and bicarbonate (right) data of all animals. Bottom left: The AAR lactate/bicarbonate ratio increased following 15 min of ischemia, remained abnormal during the following 60 min and returned to base level at one week. Bottom right: The figure shows localized hypokinesia in the AAR following ischemia and its recovery with time. The AAR had small areas of hyperenhancement in 3 of 6 animals 1 week after ischemia/reperfusion. Mean values (± SD) are displayed and statistical differences between AAR and remote myocardium are indicated (*=p<0.05; **=p<0.01; ***=p<0.001).

7.6 Discussion

In this work, the acute changes in the metabolism of pyruvate and its recovery were studied in an in-vivo model of myocardial ischemia-reperfusion. On reperfusion, the lactate/ bicarbonate signal ratio was significantly increased in the AAR, indicating a reduction in oxidative metabolism and increased anaerobic metabolism. In the hour after reperfusion, pyruvate metabolism in the AAR demonstrated the dynamic changes with a decrease in the ratio of anaerobic to oxidative metabolism towards the baseline. At 1 week, no sequelae in pyruvate metabolism could be detected within the spatial resolution of our images, indicating metabolic recovery.

There have been a number of spectroscopic studies using hyperpolarised pyruvate to assess myocardial metabolism in ischemia e.g. (22). The present study used hyperpolarised MR imaging to investigate the regional differences at multiple time points after myocardial ischemia-reperfusion. This allows the in-vivo visualization of the spatial distribution of metabolic changes across the myocardium. Similar to ex-vivo studies, an increase in the lactate to bicarbonate ratio was detected in the AAR on reperfusion. In keeping with a previous large animal study (15), the metabolic change persisted for the first hour, even when the systolic function had returned to normal.

In the animal without successful reperfusion, the lactate/bicarbonate ratio continued to increase, suggesting impaired oxidative phosphorylation with continuing anaerobic glycolysis. The return towards a baseline lactate/bicarbonate ratio in the other animals suggests that perfusion was adequate to meet the metabolic needs of the myocardium. Of course, there could have been small areas of impaired perfusion that were below the resolution of our LGE imaging technique. This raises the issue of how perfusion can interact with myocardial metabolism. It is known that a coronary stenosis leading to inadequate myocardial perfusion will result in diastolic dysfunction and then systolic dysfunction before becoming clinically apparent via ECG changes and finally angina, known as the ischemic cascade. The development of hyperpolarised imaging now presents a means of studying the role of metabolism in this process (1). Although a recent hyperpolarised study did not detect changes in acetate metabolism during dobutamine stress testing (23), this area of research remains to be fully explored.

Studies on isolated perfused rat hearts have provided data before and during permanent coronary occlusion. However, in these studies the occluded artery resulted in a confounding perfusion defect in the AAR. Correcting for the change in perfusion in these studies allowed increased lactate signal intensity and increased lactate/bicarbonate ratio in the AAR to be demonstrated. It is nevertheless noted that the hyperpolarised tracer may not have reached the central core of the ischemic zone, as myocardial collaterals are limited. Accordingly, metabolic changes may have reflected inadequate perfusion in the ischemic border zone.

A previous study using an ex-vivo model of 10 minutes of global ischemia demonstrated virtually no production of bicarbonate in the first 90 seconds of reperfusion (16), with a rapid increase in production following 10 minutes of reperfusion. In contrast to our work and other studies (22, 24), this study demonstrated a bicarbonate signal was many times greater than the lactate. The discrepancy between this ex-vivo model and our data is attributed to the fact that the perfused heart was supplied with 2 mmol pyruvate as a sole energy source while, in this in-vivo study, alternative substrates were available to the myocardium.

In the present study the metabolism, as measured by the lactate/bicarbonate ratio, had recovered to normal at 1 week. Of the eight animals planned for the one-week follow-up experiments, two died prematurely. Metabolic recovery may be associated with increased myocardial survival. However, as these animals had small infarctions on tetrazolium chloride (TTC) staining and near-normal systolic function, it seems likely that these animals died of cardiac arrhythmia rather than progressive heart failure.

Early reperfusion is the goal of therapy in patients with ST-elevation myocardial infarction. Reopening an acutely occluded coronary artery reduces the size of myocardial infarction, but is also associated with transient contractile dysfunction, arrhythmias and increased myocardial enzyme release (25) due to rapid metabolic processes summarized as reperfusion injury. So far, there is no method available allowing for assessing the magnitude of reperfusion injury in-vivo in patients. Hyperpolarised metabolic MR imaging provides the possibility to study the rapid changes in metabolism during myocardial reperfusion, enabling the in-vivo analysis of myocardial injury with different reperfusion strategies.

Other clinical possibilities include the detection of stress-induced myocardial ischemia, using the injection of hyperpolarised tracers at peak stress, avoiding the need for gadolinium contrast agents. As viable myocardium is metabolically active, hyperpolarised MR imaging could offer an alternative to LGE imaging or PET imaging in the detection of viable myocardium. Although the increased signal offered by hyperpolarisation could provide superior spatial resolution to PET, it would remain challenging to improve on the spatial resolution currently available in clinical LGE imaging.

7.6.1 Study Limitations

Rather than merely demonstrating decreased metabolism in infarcted tissue, the aim of this study was to investigate the changes in viable myocardium. Even with 15 minutes of ischemia, very small volumes of myocardial infarction (2.5 ± 2%) could be detected in some animals during histology. However, these small infarct volumes were not detectable with the spatial resolution of the metabolic imaging sequence.

As the experiments took place during the day, the animals were fasting. During fasting, pyruvate supplies only a small amount of carbon for the Krebs cycle. To increase the flux via pyruvate dehydrogenase, the rats were provided with an i.v. glucose infusion. In healthy myocardium, hyperinsulinemia and hyperglycemia increase both glycolysis and the relative contribution of pyruvate to energy production when compared to fasting rats (26). However, previous studies have shown that in myocardium recovering from low flow ischemia, hyperglycemia and hyperinsulinemia did not increase total carbohydrate or pyruvate oxidation (27).

The present study focused on pyruvate metabolism. Beyond pyruvate, the development of hyperpolarised fatty acids, such as acetate (23) may also allow the study of changes in short chain fatty acid metabolism in myocardial ischemia.

Despite the significant signal gains due to hyperpolarised MR imaging, the limited SNR of the detected metabolic products leads to limited spatial resolution. For example, in rats, we could not detect small, sub-millimeter areas of infarction However, the spatial resolution achievable is comparable to that currently available in clinical SPECT or PET studies, suggesting that it could

be rapidly transferred to use in humans. However, improvements in polarisation levels and transition to 3D imaging approaches (28) are warranted to further optimize image quality.

An issue with hyperpolarized imaging is the volume of agent required. It has been found that a 1 ml injection of a pyruvate concentration of 40 mM maximised $H^{13}CO_3$ production while resulting in minimal alteration to in vivo substrate composition (29). We injected a slightly larger volume of a similar concentration to allow us overcome the dead volume in the longer lines used while the animal was in the scanner. Animals received 1.4 ml of pyruvate followed by 0.3 ml saline flush in 3-4 separate injections, and a final injection of 0.1 ml gadolinium contrast agent and 0.3 ml saline flush at the end of the 4-hour duration of the scan, resulting in a volume of 7.6 ml over the 4-5 hours of the experiment. In the second experiment, animals received a maximum of 4.2 ml over the 3-hour experiment. Each individual injection was approximately the recommended maximum bolus of 5 ml/kg, however multiple boluses were given over the duration of the experiment. As a result, the total volume given over the duration of the first experiment was above the maximum recommended volume for the species of 20ml/kg (30). Unfortunately, giving a smaller volume of higher concentration of pyruvate was not possible, as this may inhibit lactate dehydrogenase, leading to changes in the lactate/bicarbonate ratio (29). Finally, all animals were monitored for distress using a comprehensive scoring system after each stage of the experiments. It should be noted that, despite the volumes given, euthanasia was not required in any animal.

In summary, the present hyperpolarised MR imaging animal study has demonstrated detection of local metabolic changes in myocardial ischemia/reperfusion and has identified an acute increase in the lactate-to-bicarbonate ratio in the area-at-risk after reperfusion with recovery back to baseline by 1 week. Given the translation of the imaging technology to humans (31), the approach promises a diagnostic window to assess metabolic changes caused by transient ischemia and reperfusion therapies.

7.7 References:

(1) Nesto, R.W., and Kowalchuk, G.J. (1987). The ischemic cascade: temporal sequence of hemodynamic, electrocardiographic and symptomatic expressions of ischemia. *Am. J. Cardiol.* **59**(7), 23C-30C.

(2) Gianrossi, R., Detrano, R., Mulvihill, D., Lehmann, K., Dubach, P., Colombo, A., McArthur, D., and Froelicher, V. (1989). Exercise-induced ST depression in the diagnosis of coronary artery disease. A meta-analysis. *Circulation* **80**(1), 87-98.

(3) Greenwood, J.P., Maredia, N., Younger, J.F., Brown, J.M., Nixon, J., Everett, C.C., Bijsterveld, P., Ridgway, J.P., Radjenovic, A., Dickinson, C.J.*, et al.* (2012). Cardiovascular magnetic resonance and single-photon emission computed tomography for diagnosis of coronary heart disease (CE-MARC): a prospective trial. *Lancet* **379**(9814), 453-60.

(4) Manka, R., Wissmann, L., Gebker, R., Jogiya, R., Motwani, M., Frick, M., Reinartz, S., Schnackenburg, B., Niemann, M., Gotschy, A.*, et al.* (2015). Multicenter evaluation of dynamic three-dimensional magnetic resonance myocardial perfusion imaging for the detection of coronary artery disease defined by fractional flow reserve. *Circ. Cardiovasc. Imaging* **8**(5).

(5) Mahajan, N., Polavaram, L., Vankayala, H., Ference, B., Wang, Y., Ager, J., Kovach, J., and Afonso, L. (2010). Diagnostic accuracy of myocardial perfusion imaging and stress echocardiography for the diagnosis of left main and triple vessel coronary artery disease: a comparative meta-analysis. *Heart* **96**(12), 956-66.

(6) Braunwald, E., and Kloner, R.A. (1982). The stunned myocardium: prolonged, postischemic ventricular dysfunction. *Circulation* **66**(6), 1146-9.

(7) Ardenkjaer-Larsen, J.H., Fridlund, B., Gram, A., Hansson, G., Hansson, L., Lerche, M.H., Servin, R., Thaning, M., and Golman, K. (2003). Increase in signal-to-noise ratio of > 10,000 times in liquid-state NMR. *Proc. Natl. Acad. Sci. U. S. A.* **100**(18), 10158-63.

(8) Atherton, H.J., Schroeder, M.A., Dodd, M.S., Heather, L.C., Carter, E.E., Cochlin, L.E., Nagel, S., Sibson, N.R., Radda, G.K., Clarke, K.*, et al.* (2011). Validation of the in vivo assessment of pyruvate dehydrogenase activity using hyperpolarised 13C MRS. *NMR Biomed.* **24**(2), 201-8.

(9) Ugander, M., Bagi, P.S., Oki, A.J., Chen, B., Hsu, L.Y., Aletras, A.H., Shah, S., Greiser, A., Kellman, P., and Arai, A.E. (2012). Myocardial Edema as Detected by Pre-Contrast T1 and T2 CMR Delineates Area at Risk Associated With Acute Myocardial Infarction. *JACC Cardiovasc. Imaging* **5**(6), 596-603.

(10) Dodd, M.S., Ball, D.R., Schroeder, M.A., Le Page, L.M., Atherton, H.J., Heather, L.C., Seymour, A.M., Ashrafian, H., Watkins, H., Clarke, K.*, et al.* (2012). In vivo alterations in cardiac metabolism and function in the spontaneously hypertensive rat heart. *Cardiovasc. Res.* **95**(1), 69-76.

(11) Menichetti, L., Frijia, F., Flori, A., Wiesinger, F., Lionetti, V., Giovannetti, G., Aquaro, G.D., Recchia, F.A., Ardenkjaer-Larsen, J.H., Santarelli, M.F.*, et al.* (2012). Assessment of real-time myocardial uptake and enzymatic conversion of hyperpolarized [1-(1)(3)C]pyruvate in pigs using slice selective magnetic resonance spectroscopy. *Contrast Media Mol. Imaging* **7**(1), 85-94.

(12) Merritt, M.E., Harrison, C., Storey, C., Jeffrey, F.M., Sherry, A.D., and Malloy, C.R. (2007). Hyperpolarized 13C allows a direct measure of flux through a single enzyme-catalyzed step by NMR. *Proc. Natl. Acad. Sci. U. S. A.* **104**(50), 19773-7.

(13) Moreno, K.X., Sabelhaus, S.M., Merritt, M.E., Sherry, A.D., and Malloy, C.R. (2010). Competition of pyruvate with physiological substrates for oxidation by the heart: implications for studies with hyperpolarized [1-13C]pyruvate. *Am. J. Physiol. Heart Circ. Physiol.* **298**(5), H1556-64.

(14) Schroeder, M.A., Atherton, H.J., Ball, D.R., Cole, M.A., Heather, L.C., Griffin, J.L., Clarke, K., Radda, G.K., and Tyler, D.J. (2009). Real-time assessment of Krebs cycle metabolism using hyperpolarized 13C magnetic resonance spectroscopy. *FASEB J.* **23**(8), 2529-38.

(15) Golman, K., Petersson, J.S., Magnusson, P., Johansson, E., Akeson, P., Chai, C.M., Hansson, G., and Mansson, S. (2008). Cardiac metabolism measured noninvasively by hyperpolarized 13C MRI. *Magn. Reson. Med.* **59**(5), 1005-13.

(16) Merritt, M.E., Harrison, C., Storey, C., Sherry, A.D., and Malloy, C.R. (2008). Inhibition of carbohydrate oxidation during the first minute of reperfusion after brief ischemia: NMR detection of hyperpolarized 13CO2 and H13CO3. *Magn. Reson. Med.* **60**(5), 1029-36.

(17) O h-Ici, D., Jeuthe, S., Dietrich, T., Berger, F., Kuehne, T., Kozerke, S., and Messroghli, D.R. (2014). Closed-chest small animal model to study myocardial infarction in an MRI environment in real time. *Int. J. Cardiovasc. Imaging*. **31**(1), 115-21.

(18) Lauritzen, M.H., Laustsen, C., Butt, S.A., Magnusson, P., Sogaard, L.V., Ardenkjaer-Larsen, J.H., and Akeson, P. (2013). Enhancing the [13C]bicarbonate signal in cardiac hyperpolarized [1-13C]pyruvate MRS studies by infusion of glucose, insulin and potassium. *NMR Biomed.* **26**(11), 1496-500.

(19) Krajewski M, Batel M, Weiss K, Sigfridsson A, Batsios G, Ernst M, and S., K. (2013). A flexible multi-sample DNP system for rapid sequential dissolutions. Paper presented at: *Proceedings 21st Scientific Meeting, International Society for Magnetic Resonance in Medicine* (Salt Lake City).

(20) Sigfridsson, A., Weiss, K., Wissmann, L., Busch, J., Krajewski, M., Batel, M., Batsios, G., Ernst, M., and Kozerke, S. (2014). Hybrid multiband excitation multiecho acquisition for hyperpolarized C spectroscopic imaging. *Magn. Reson. Med.* **73**(5), 1713-7.

(21) Reeder, S.B., Wen, Z., Yu, H., Pineda, A.R., Gold, G.E., Markl, M., and Pelc, N.J. (2004). Multicoil Dixon chemical species separation with an iterative least-squares estimation method. *Magn. Reson. Med.* **51**(1), 35-45.

(22) Dodd, M.S., Atherton, H.J., Carr, C.A., Stuckey, D.J., West, J.A., Griffin, J.L., Radda, G.K., Clarke, K., Heather, L.C., and Tyler, D.J. (2014). Impaired in vivo mitochondrial krebs cycle activity after myocardial infarction assessed using hyperpolarized magnetic resonance spectroscopy. *Circ. Cardiovasc. Imaging* **7**(6), 895-904.

(23) Koellisch, U., Gringeri, C.V., Rancan, G., Farell, E.V., Menzel, M.I., Haase, A., Schwaiger, M., and Schulte, R.F. (2014). Metabolic imaging of hyperpolarized [1-C]acetate and [1- C]acetylcarnitine - investigation of the influence of dobutamine induced stress. *Magn. Reson. Med.*

(24) Ball, D.R., Cruickshank, R., Carr, C.A., Stuckey, D.J., Lee, P., Clarke, K., and Tyler, D.J. (2013). Metabolic imaging of acute and chronic infarction in the perfused rat heart using hyperpolarised [1-13C]pyruvate. *NMR Biomed.* **26**(11), 1441-50.

(25) Piper, H.M., Garcia-Dorado, D., and Ovize, M. (1998). A fresh look at reperfusion injury. *Cardiovasc. Res.* **38**(2), 291-300.

(26) McNulty, P.H., Cline, G.W., Whiting, J.M., and Shulman, G.I. (2000). Regulation of myocardial [(13)C]glucose metabolism in conscious rats. *Am. J. Physiol. Heart Circ. Physiol.* **279**(1), H375-81.

(27) Wang, P., Lloyd, S.G., and Chatham, J.C. (2005). Impact of high glucose/high insulin and dichloroacetate treatment on carbohydrate oxidation and functional recovery after low-flow ischemia and reperfusion in the isolated perfused rat heart. *Circulation* **111**(16), 2066-72.

(28) Miller, J.J., Lau, A.Z., Teh, I., Schneider, J.E., Kinchesh, P., Smart, S., Ball, V., Sibson, N.R., and Tyler, D.J. (2015). Robust and high resolution hyperpolarized metabolic imaging of the rat heart at 7 t with 3d spectral-spatial EPI. *Magn. Reson. Med.*, n/a-n/a.

(29) Schroeder, M.A., Atherton, H.J., Cochlin, L.E., Clarke, K., Radda, G.K., and Tyler, D.J. (2009). The effect of hyperpolarized tracer concentration on myocardial uptake and metabolism. *Magn. Reson. Med.* **61**(5), 1007-14.

(30) S., W., and Lloyd, M. (2000). *Handbook of laboratory animal management and welfare.* (Oxford: Blackwell Publishing).

(31) Nelson, S.J., Kurhanewicz, J., Vigneron, D.B., Larson, P.E., Harzstark, A.L., Ferrone, M., van Criekinge, M., Chang, J.W., Bok, R., Park, I.*, et al.* (2013). Metabolic imaging of patients with prostate cancer using hyperpolarized [1-(1)(3)C]pyruvate. *Sci. Transl. Med.* **5**(198), 198ra108.

Chapter 8 - Conclusion

This thesis focused on the structural and metabolic changes occurring in acute myocardial ischemia and reperfusion, using the MRI techniques of T_1 mapping and hyperpolarised spectroscopic imaging. The work ranged from the development of the animal model, to the validation of the imaging tools, to the investigation of the changes in native and post-contrast myocardial T_1 and pyruvate metabolism following occlusion of the coronary artery and reperfusion.

Initially, the small animal model of coronary occlusion was developed. This enabled us to occlude the left coronary artery while the animal remained in the bore of the scanner. This method avoids some of the confounders of the open chest myocardial ischemia models. It also allows the pattern of myocardial ischemia to be varied, with different durations of myocardial ischemia and reperfusion and thereby allowing the study of pre- and postconditioning. This model could also be used for other imaging methods, such as nuclear imaging, where the confounders of an open thorax were to be avoided, or where access to the animal is limited.

Our group had already developed and validated a novel technique of myocardial T_1 mapping in small animals. The SALLI pulse sequence overcomes some of the challenges of high heart rate and uses the T_1 recovery time to generate inversion-recovery and cine-MR images. This time efficient method of imaging was then validated against the gold standard of assessment of left ventricular function, conventional cine MR imaging while the LGE inversion recovery images were validated against myocardial staining for infarction.

Using the model developed in Chapter 3, we proceeded to investigate the acute changes in myocardial T_1 with varying durations of myocardial ischemia. We found that changes in myocardial T_1 began within the first 15 minutes of ischemia. The myocardial T_1 values continued to increase slightly with increasing duration of ischemia, but interestingly, did not increase significantly following myocardial reperfusion. Myocardial T_1 values then remained elevated for the next 90 minutes following reperfusion but did not change significantly.

We then proceeded to investigate the effects of preconditioning on myocardial T_1 values. Similar to studies using ex-vivo methods of measurement of myocardial oedema, we found that

preconditioning led to reduced myocardial oedema. The T_1 values rose more slowly and did not reach the level of remote myocardium at comparable time points.

We found that the native T_1 values in the AAR changed little from day 0 to day 3 and day 7 and remained higher than those of the remote myocardium. It was also true that the post-contrast T_1 values in the area at risk were significantly lower that the remote myocardium at each stage.

Finally, we studied the acute changes in pyruvate metabolism following a brief period of myocardial ischemia. An in-vivo technique of metabolic imaging was first optimised and assessed for reproducibility. We found that, following 15 minutes of myocardial ischemia, the lactate/bicarbonate ratio was significantly increased in the AAR. This indicated that, although myocardial perfusion had resumed, with resumption of systolic function, that the myocardial metabolism continued to produce increased levels of lactate from the anaerobic metabolism of pyruvate, with reduced aerobic metabolism of pyruvate into the Krebs cycle. This difference persisted for the first 60 minutes of myocardial reperfusion. When the metabolism was reassessed one week following the ischemic episode, the lactate/bicarbonate ratio in the AAR was indistinguishable from the remote myocardium, indicating that the myocardium had returned to normal levels of aerobic metabolism. It would be of interest to study the effects of various treatments, including conditioning, on myocardial metabolism in ischemia.

T_1 mapping has already progressed from a research tool into wider clinical use. Technical challenges, such as long sequence duration or variability at higher heart rates, are being addressed with modified shortened sequences. Alternatives to IR methods also exist, including saturation recovery methods. These have the advantage the recovery of T_1 is measured, rather than T_1^* as with IR methods such as MOLLI. Accuracy is improved, as correction for T_1^* is not required. It remains to be seen whether the potential gains in accuracy provided by saturation recovery methods will result in a practical clinical benefit.

Spatial resolution plays a significant role in T_1 mapping. As the T_1 values of blood and myocardium are very different, a partial volume effect will have a significant impact on the T_1 value in a voxel at the endocardium for example. It also makes T_1 mapping of thinner structures such as thin walled infarcts, atria and the right ventricle more demanding. For the purposes of small animal imaging, it makes the detection of varying degrees of injury from endocardium to

epicardium very challenging. Improvements in parallel imaging may allow increased image resolution, but as of yet, T_1 mapping does not reach the sensitivity of LGE for the detection of small focal injury or fibrosis.

Although we demonstrated significant changes in myocardial metabolism in a small animal model, it may be that a small animal is the most challenging in-vivo model to use for this technique. In spite of the enormous increases in SNR obtained with hyperpolarisation, obtaining high-resolution imaging remains challenging. Strategies to optimise SNR will in the future include improving polarisation, minimising polarisation loss before tracer injection and optimised imaging sequences. For example, we had a calculated polarisation of [1-^{13}C]pyruvate of 19% at 30 seconds following dissolution. Although improvements in pulse sequence and coil technology, such as compressed sensing and cryogenic coils, will give improvements in SNR, efforts to maximise the polarisation or to minimise polarisation loss before injection of the tracer offer larger potential gains. Further improvement in the efficiency and speed of polarisation can be expected with the use of new radicals as sources of unpaired electrons, or by first polarising ^{1}H before transferring this polarisation to ^{13}C. Outside the bore of the polariser, polarisation can be rapidly lost as the T_1 of the tracer can become quite short at low fields. An optimal system could see the polariser located in the same room, or same device, as the MR scanner, allowing control of the magnetic field, and rapid, semi-automatic injection of the tracer. Indeed, as pharmaceutical grade tracer is required for injection of human subjects, automatisation of as many aspects of the hyperpolarisation process including a quality control system, would lead to improved reproducible imaging.

Hyperpolarised imaging has opened up new areas of physiology to study. Hyperpolarised probes such as fumarate are already being used as a non-invasive marker of viability. Further insight into cellular biology will be driven by hyperpolarised imaging, and these findings will, in turn, lead to improved tracers and metabolic targets for study. As the heart is metabolically an omnivore, and can change its source of energy depending on availability, optimised protocols will involve the stimulation of various metabolic pathways, and studying the result. For example, our study involved the priming of carbohydrate metabolism with the use of a glucose infusion. This then allowed the imaging of hyperpolarised [1-^{13}C]pyruvate as the myocardium had switched from fatty acids to carbohydrates as its primary source of energy.

We have demonstrated that changes in myocardial structure and metabolism are detectable after very brief, 15-minute, periods of myocardial ischemia. We found that levels of myocardial oedema persisted for at least one week following an ischemic episode. The recovery of metabolism followed a different pattern, remaining abnormal but showing a return towards baseline in the 60 minutes following ischemia, whereas it had returned to normal one week later. This work demonstrated the utility of T_1 mapping in assessing the myocardial area at risk. We found that T_1 values remained elevated in the week following ischemia. This indicates that T_1 mapping could be used to detect acute myocardial injury, and could perhaps be used to delineate the myocardial AAR. The AAR could also be detected by the metabolic changes following ischemia-reperfusion. In the future, the lactate/bicarbonate ratio could be used to estimate the degree of myocardial injury, estimate myocardial viability and measure the AAR. Until now, there has been no means of studying the metabolism of the myocardium as it recovers from ischemia and no method of studying reperfusion injury in-vivo. The combination of both T_1 mapping and hyperpolarised imaging can provide unique insights into the process of myocardial ischemia and reperfusion.

Appendix A: Publications & Conference Proceedings

Conference Posters

- **Studying the course of myocardial ischemia and reperfusion in rats in vivo**

  O h-Ici D, Dietrich T, Kühne T, Messroghli D

  European Society of Cardiology (ESC) Scientific sessions, Sept 2012 (Munich, Germany)

- **Assessment of Acute Myocardial Ischemia with Unenhanced T1 mapping MR Imaging**

  O h-Ici D, Jeuthe S, Dietrich T, Pietsch H, Schuetz G, Berger F, Kuehne T, Kozerke S, Messroghli D

  Society of Cardiovascular Magnetic Resonance (SCMR) 15th Annual Scientific Sessions, Jan 2012 (Orlando, FL)

- **Validation of Small-Animal Look-Locker Inversion Recovery (SALLI) Cine versus Cine MR in assessment of Left Ventricular Function**

  O h-Ici D, Jeuthe S, Dietrich T, Pietsch H, Schuetz G, Berger F, Kuehne T, Kozerke S, Messroghli D

  SCMR 15th Annual Scientific Sessions, Jan 2012 (Orlando, FL)

- **Multi-echo Single-shot EPI for Hyperpolarised 13C Cardiac Metabolic Imaging of Small Animals**

  Sigfridsson A, Weiss K, Wissmann L, Busch J, Krajewski M, **O h-Ici D**, Batel M, Batsios G, Kozerke S

  SCMR 15th Annual Scientific Sessions, Jan 2012 (Orlando, FL)

- **Metabolic profiling using ex-vivo proton magic angle spinning magnetic resonance spectroscopy (1H-MAS-MRS) detects myocardial injury in experimental autoimmune myocarditis (EAM)**

  Münch F, Retel J, Jeuthe S, van Rossum B, **O h-Ici D**, Kühne T, Berger F, Oschkinat H, Messroghli D

  EuroCMR 2014

Peer Reviewed Publications

- **Assessment of Diffuse Myocardial Fibrosis in Rats Using Small Animal Look-Locker Inversion Recovery (SALLI) T1 Mapping**

  Messroghli D, Nordmeyer S, Dietrich T, Dirsch O, Kaschina E, Savvatis K, **O h-Ici D**, Klein C, Berger F, Kuehne T

  Circ Cardiovasc Imaging 2011;4(6)636-40

- **Magnetic resonance imaging of myocardial edema using the short inversion time inversion recovery (STIR) black-blood technique**

  O h-Ici D, Ridgway JP, Kuehne T, Berger F, Plein S, Sivananthan M, Messroghli DR

  J of Cardiovasc Magn Reson 2012, 14:22

- **Assessment of cardiac function and myocardial morphology using Small Animal Look-Locker Inversion recovery (SALLI) MRI in rats**

  Jeuthe S, **O h-Ici D**, Messroghli DR

  J Vis Exp 2013 19;(77)

- **T1 Mapping in Ischemic Heart Disease**

  O h-Ici, D, Jeuthe S, Al-Wakeel N, Berger F, Kuehne T, Kozerke, S, Messroghli DM

  EHJ Cardiovascular Imaging 2014;15(6), 597-602;

- **Mortality and Morbidity in Different Immunization Protocols for Experimental Autoimmune Myocarditis in Rats**

  Schmerler P, Jeuthe S, **O h-Ici D**, Wassilew K, Lauer D, Kaschina E, Kintscher U, Mueller S, Kühne T, Berger F, Steckelings U, Paulis L, Messroghli DR

  Acta Physiologica 2014;21, 889-898

- **The Influence of the Region of Interest Width on Two-Dimensional Speckle Tracking Based Measurements of Strain and Strain Rate**

  Spriestersbach H, **O h-Icí D**, Schmitt B, Berger F, Schmitz L

  Echocardiography 2015;32(1), 89-9.

- **Closed-chest small animal model to study myocardial infarction in an MRI environment in real time**

  O h-Ici D, Jeuthe S, Kühne T, Kozerke S, Messroghli D

  Inter J Cardiovasc Imaging 2015;31(1), 115-21

- **Cardiac magnetic resonance imaging in patients with complex congenital heart disease following primary or secondary implantation of MRI-conditional pacemaker system**

  Al-Wakeel N, **O h-Ici D**, Schmitt KR, Messroghli DR, Riesenkampff E, Berger F, Kuehne T, Peters B

  Cardiol Young 2015;23, 1-9.

- **Cardiovascular magnetic resonance predictors of clinical outcome in patients with suspected acute myocarditis**

  Sanguineti F, Garot P, Mana M, **O h-Ici D**, Hovasse T, Unterseeh T, Louvard Y, Troussier X, Morice MC, Garot J

  J Cardiovasc Magn Reson 2015;**17**(1) 78

- **Hyperpolarized Metabolic MR Imaging of Acute Myocardial Changes and Recovery Upon Ischemia-Reperfusion in a Small Animal Model**

  O h-Ici D, Wespi P, Busch J, Wissmann L, Krajewski M, Weiss K, Sigfridsson A, Messroghli D, Kozerke S

  Radiology 2016 Mar;278(3):742-51

- **A Universal Delivery System for Percutaneous Heart Valve Implantation**

  Bartosch M, Peters H, Spriestersbach H, **O h-Ici D**, Berger F, Schmitt B.

  Ann Biomed Eng 2016 Feb 10. [Epub ahead of print]

- **Myocardial T1 maps reflect histological findings in acute and chronic stages of myocarditis in a rat model**

  Jeuthe S, Wassilew K, **O h-Ici D**, Ferreira da Silva T, Muench F, Berger F, Kuehne T, Pieske B, Messroghli D

  J Cardiovasc Magn Reson 2016;18(1):19.